MICROCOPY RESOLUTION TEST CHART

NATIONAL BUREAU OF STANDARDS-1963-A

LEVEL

AUTOMATIC TARGET CUER
FIRST QUARTER REPORT

Prepared by

B. Deal   T. Noda
C. M. *Lo*   J. Powers
R. Taylor   G. Guzman
V. Norwood   H. Greenberger
H. Henning   G. Towner
T. Daggett   G. Parker

NORTHROP CORPORATION
Electro-Mechanical Division
500 East Orangethorpe Avenue
Anaheim, California 92801

23 October 1979

QUARTER REPORT
FOR PERIOD
18 May 1979 — 31 August 1979

NIGHT VISION AND ELECTRO-OPTICS LABORATORY
FORT BELVOIR, VIRGINIA 22060

DDC
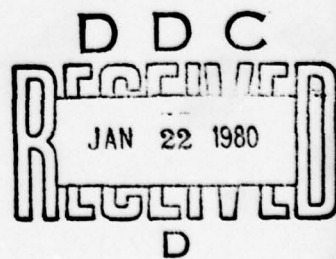
RECEIVED
JAN 22 1980

D

80   1 21 132

REPORT DOCUMENTATION PAGE		READ INSTRUCTIONS BEFORE COMPLETING FORM
1. REPORT NUMBER	2. GOVT ACCESSION NO.	3. RECIPIENT'S CATALOG NUMBER
4. TITLE (and Subtitle) AUTOMATIC TARGET CUER. FIRST QUARTER REPORT		5. TYPE OF REPORT & PERIOD COVERED QUARTERLY PROGRESS REPORT 18 MAY — 31 AUGUST 1979
		6. PERFORMING ORG. REPORT NUMBER NORT - 79Y100
7. AUTHOR(s) B. Deal, C.M. Lo, R. Taylor, V. Norwood H. Henning, T. Daggett, T. Moda, J. Powers, G. Guzman, H. Greenberger, G. Towner, G. Parker		8. CONTRACT OR GRANT NUMBER(s) DAAK70-79-C-0066
9. PERFORMING ORGANIZATION NAME AND ADDRESS Northrop Electro-Mechanical Division 500 E. Orangethorpe Avenue Anaheim, Calif. 92801		10. PROGRAM ELEMENT, PROJECT, TASK AREA & WORK UNIT NUMBERS
11. CONTROLLING OFFICE NAME AND ADDRESS Night Vision and Electro-Optics Laboratory Fort Belvoir, VA 22060		12. REPORT DATE 23 Oct 1979
		13. NUMBER OF PAGES 94
14. MONITORING AGENCY NAME & ADDRESS(if different from Controlling Office)		15. SECURITY CLASS. (of this report) UNCLASSIFIED
		15a. DECLASSIFICATION/DOWNGRADING SCHEDULE

16. DISTRIBUTION STATEMENT (of this Report)

Approved for public release distribution unlimited.

17. DISTRIBUTION STATEMENT (of the abstract entered in Block 20, if different from Report)

18. SUPPLEMENTARY NOTES

19. KEY WORDS (Continue on reverse side if necessary and identify by block number)

Infrared	Target Recognition
FLIR	Image Enhancement
Target Cuer	Image Segmentation

20. ABSTRACT (Continue on reverse side if necessary and identify by block number)

This is the first quarterly progress report for the ATC program. It covers system organization and specific algorithm development, leading to the construction of a real-time target cueing system.

DD FORM 1473 1 JAN 73   EDITION OF 1 NOV 65 IS OBSOLETE
S/N 0102-014-6601
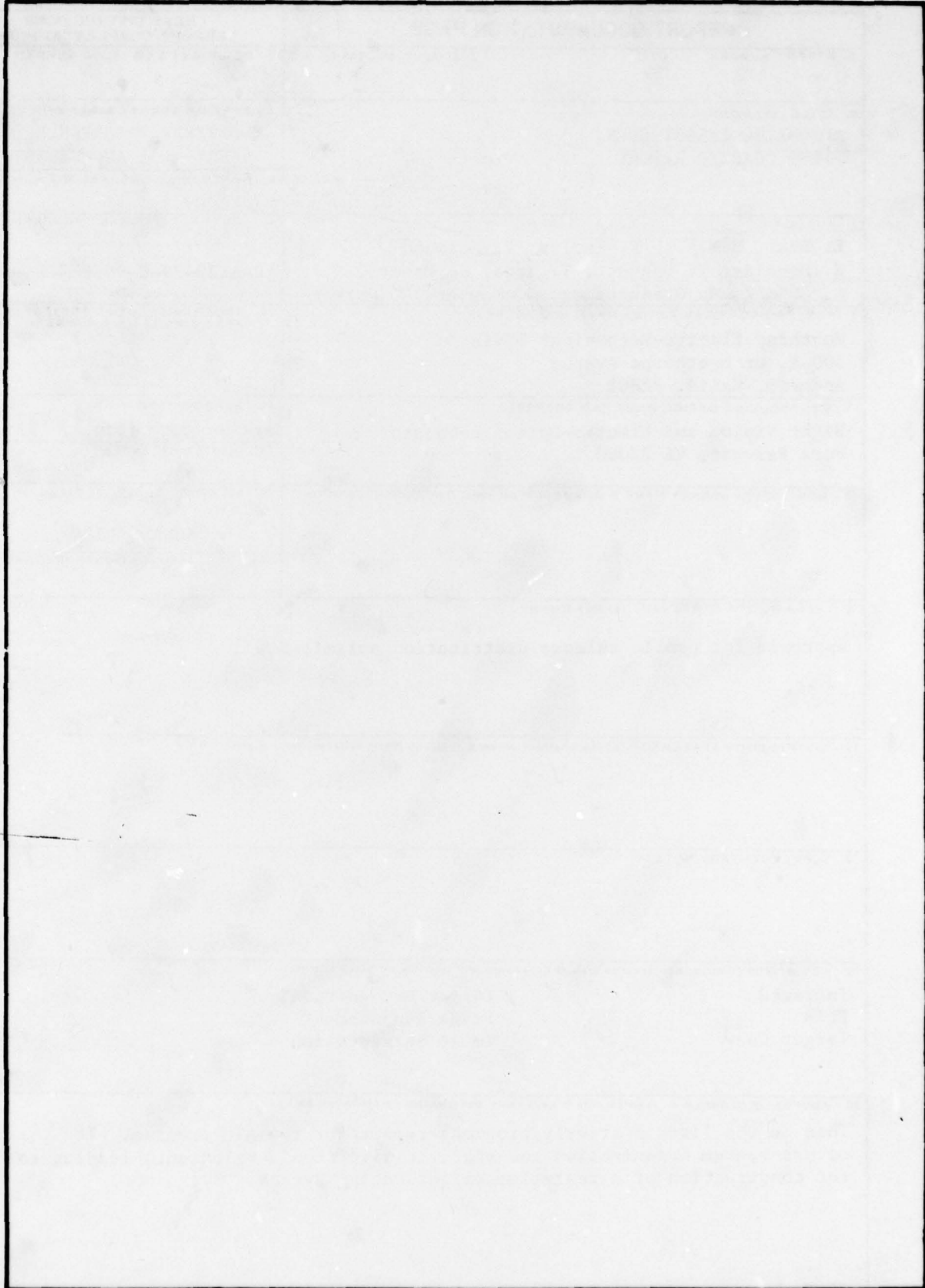
"The views, opinions, and/or findings contained in this
report are those of the authors and should not be
construed as an official department of the Army position,
policy, or decision, unless so designated by other
documentations."

CONTENTS

CONTENTS (Continued)

Illustrations

Illustrations (Continued)

Tables

SECTION 1

INTRODUCTION

This is the first quarterly progress report for the Automatic Target Cuer (ATC) Program, Contract No. DAAK70-79-C-0066. The ATC Program is a 32-month effort culminating in the delivery of two developmental ATC systems to the Night Vision and Electro-Optical Laboratory (NV&EOL). The first system will be in an engineering, breadboard-type configuration while, the second system will be a flight-worthy unit and integrated into the Light Observation Helicopter Target Acquisition/Designation System (LOHTADS) helicopter. Flight tests will be conducted with the second unit.

The ATC program can be divided into three phases. Phase I (6 months) is the system analysis and design effort that includes primarily algorithm development and tradeoff studies. Also included in Phase I is the design and construction of the ATC interfaces and memories. Phase II (12 months) is a modeling and construction phase. The hardware and software specified and designed during Phase I will be constructed during this effort. The specific hardware functions of the ATC will also be modeled, in software, to facilitate system analysis and test. Phase II culminates with the completion of the Model 1 ATC system. During the third phase (14 months), which is primarily a construction and test phase, the Model 2 ATC system will be built. Construction of the Model 2 ATC will be basically a repackaging of the Model 1 system in a flight-worthy configuration. Ground and flight tests will be conducted on both the Model 1 and Model 2 ATC systems during Phase III.

This report will describe the progress in the design of the processing algorithms and hardware which is currently undergoing development as part of Phase I. Plans for the technical effort of the second quarter are also presented.

SECTION 2
SYSTEM OVERVIEW

The Automatic Target Cuer (ATC) system is made from several major subsystems. This section will show the relationship of the major system functional elements to the total ATC. The specific implementations of each subsystem function are covered in other parts of the report. The ATC system performance goals are also presented here.

2.1 ATC SYSTEM

The block diagram for the ATC system and its Forward-Looking Infrared (FLIR) interface is shown in Figure 2-1. Infrared imagery is first sensed by a common module FLIR. The particular FLIR in this case is the one associated with the Light Observation Helicopter Target Acquisition/Designation System (LOHTADS). The outputs of the FLIR postamplifiers are input to the MUX/digitizer. The MUX/digitizer takes the 120 analog detector channels from the FLIR and reformats them into four 8-bit sampled data paths. The image sample locations are determined by information obtained by the scan-mirror-position sensor. The resultant multiplexed digital video is then input to the ATC, where it is divided into two system function paths: a full-frame rate path and a sampled frame path.
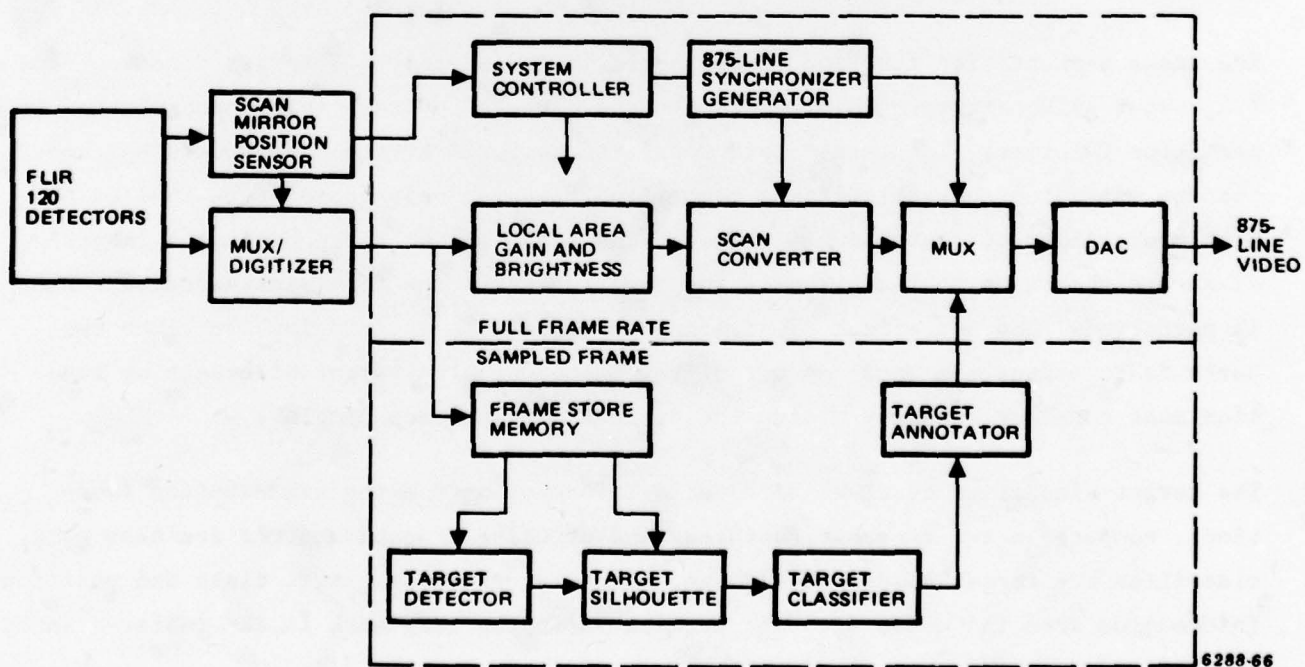
Figure 2-1. ATC System Block Diagram

The full-frame rate path performs the functions required to construct a 875-line television compatible display from the multiplexed digital video. The four 8-bit data paths are first input to the Local Area Gain Brightness Control (LAGBC). Synthetic dc restoration is currently not a function of the ATC. LAGBC reduces the apparent dynamic range of the digital video so that only 6 bits of amplitude resolution are required. A 2-to-1 reduction in spatial resolution is also performed to arrive at an image-sample rate that is compatible with the output display format.

The four 6-bit data paths that result from LAGBC become the input to the scan converter memory. This memory uses a full frame of digital memory to perform a scan conversion from a multiplexed digital video to a raster-scanned digital video. The system controller and 875-line sync generator synchronize this process. The output format of the scan converter is such that the entire scan converter frame memory is read out on every field of the display video. Before the video is sent to the digital-to-analog converter, it is first mixed with target annotation from the sampled frame path.

The sampled frame path also accepts multiplexed digital video, but an image "snap-shot" is created by loading a single FLIR frame into the frame store memory. This frame snapshot is required to allow the image segmentation and target classification functions to randomly access the FLIR scene.

The image segmentation function is performed in two steps: (1) target detection and (2) target silhouetting. This is done to speed up the overall throughput of the segmentation function. The target detector first performs a target prescreening function by examining the entire frame memory and flagging only those areas that have a high probability of containing a target. The locations of these candidate target areas are then sent to the silhouetting function where the final image segmentation is performed. The net effect of dividing segmentation, in this fashion, into two parts is to reduce the total amount of raw image data the target silhouetting function must consider, thereby making the silhouetting process simpler.

The target classifier receives silhouette information from the segmentation functions, computes a set of shape features, and by using a nonparametric decision rule, classifies the target shape. The target annotator receives target class and position information from the classifier and creates an appropriate mark in the raster-scanned digital video stream.

2.2 DESIGN GOALS

The design goals of the ATC system are presented below:

    a. <u>Minimum Resolvable Temperature (MRT)</u> -- The MRT of the LOHTADS FLIR, when measured using the LAGBC function of the ATC, should be less than 10 percent greater than the MRT measured under manual operation.

    b. <u>Target Classes</u> - The ATC should be capable of handling six target types: (1) tank, (2) APC, (3) truck, (4) antiaircraft cannon vehicle, (5) antiaircraft missile launcher, and (6) jeep.

    c. <u>Number of Targets</u> - The ATC should be capable of cueing at least 10 targets per sampled frame.

    d. <u>Target Update Rate</u> - The ATC should update target cues at least every third, displayed-image frame.

    e. <u>Probability of Detection and Classification</u> - The probabilities of detection and classification should be compatible with the Johnson criteria[1].

    f. <u>Probability of False Alarm</u> - The false alarm rate should be less than one per sampled FLIR frame.

    g. <u>Volume</u> - The physical volume of the Model 2 ATC should be less than 1.0 cubic feet.

[1] J. Johnson 'Analysis of Image Forming Systems,' Proc. of Image Intensifier Symposium, 1958 pp 249, 273.

SECTION 3

ALGORITHM DEVELOPMENT

3.1 IMAGE ENHANCEMENT

A FLIR image enhancement process is one in which the image is manipulated for the
purpose of increasing the information extractable by the human visual system or
suitable for machine analysis. Enhancement techniques are inherently quite dif-
ferent from image restoration methods. The image restoration is the estimation of
the original image (object) signal by both blur removal and noise suppression. Thus,
image restoration needs knowledge of the degrading phenomeon. Image enhancement
may not specifically need this a priori knowledge. Essentially, any technique is fair
game for enhancement if the enhanced image provides additional information about
the object which was not readily apparent in the original image. There is no
general unifying theory of image enhancement because there is no generally accepted
standard of image quality that can be used as a design criterion for an image
enhancement processor.

Image enhancement techniques are based on one primary goal: maximum use of the
available gray levels in the imaging display. Secondary goals include: (1) the
need for real-time operation, (2) the avoidance of complex algorithms which may
impact the robustness and versatility of the system, and (3) the need for simple,
compact hardware.

This section presents the implementations of seven candidates for image enhancement
and shows experimental results. Finally, based on subjective criteria to judge en-
hanced image quality, the three best image enhancement techniques for use in the FLIR
image processor are proposed. These three techniques will then be traded for sim-
plest implementation.

3.1.1 FLIR Image Enhancement Techniques

3.1.1.1 Variable Threshold Zonal Filtering - For referenced documents, see Section 3.4, Number 1. The variable threshold zonal filtering is an active, nonlinear, image-enhancement process which employs a simple subtractive box filter to remove the low-frequency components which usually obscure the more interesting local image details and targets. Zonal differentiation of the image is accomplished during computation of the local average surrounding each pixel. Only those nearby pixels in the window, whose gray level values lie within a prespecified brightness range of the gray value of the current central pixel, are used to compute the local average (nonstationary mean). The brightness range is determined by two relative threshold levels, T_L and T_U, as illustrated in Figure 3-1.

A thresholded local mean $\bar{f}_{ij}$ is computed by averaging the brightness values of all points from within the local rectangular region. This must satisfy the criterion $(f_{ij} - T_L) \leq f_{mn} \leq (f_{ij} + T_U)$, i.e, a thresholded local mean $\bar{f}_{ij}$ is calculated from those pixels whose gray levels lie within the cross-hatched region of the local area histogram shown in Figure 3-1. Specifically, the thresholded local mean defined by:

$$\bar{f}_{ij} = \frac{\sum_R \delta_{mn} f_{mn}}{\sum_R \delta_{mn}} , \qquad (3\text{-}1)$$

where

$$\delta_{mn} = \begin{cases} 1 & (f_{ij} - T_L) \leq f_{mn} \leq (f_{ij} + T_U) \\ 0 & \text{otherwise,} \end{cases}$$

and where R is the (2M +1) by (2N +1) local window region centered at pixel (i,j) and defined by $(i - M) \leq m \leq (i + M)$ and $(j - N) \leq n \leq (j + N)$.

The zonal filter enhanced image is formed by the fraction of the resulting variations from the thresholded local mean, the fraction of the original image, and a dc bias, i.e.,

$$g_{ij} = S(1 - \alpha) (f_{ij} - \bar{f}_{ij}) + S\alpha f_{ij} + C, \qquad (3\text{-}2)$$
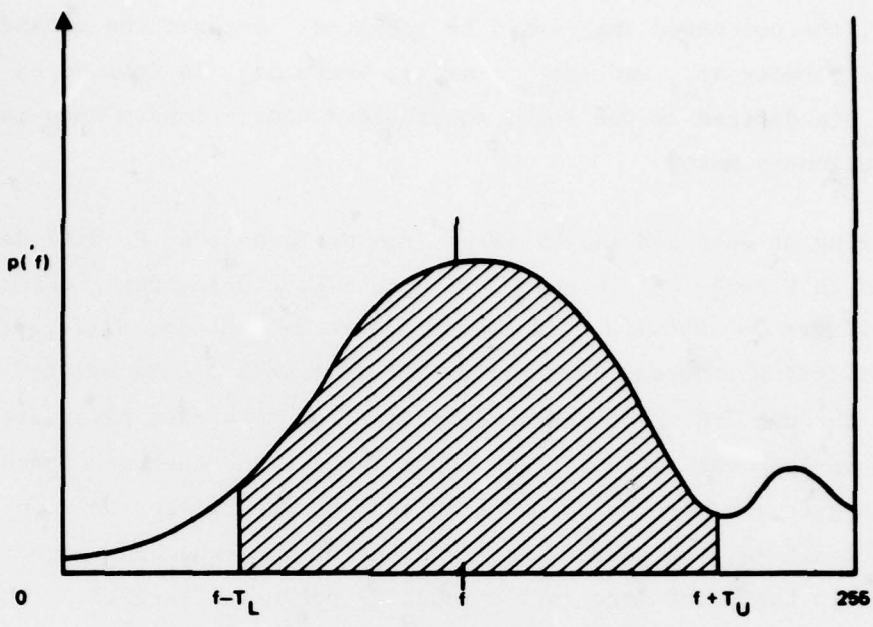
Figure 3-1. Histogram of Typical FLIR Image

where

g_{ij} is a filtered enhanced image gray level at pixel (i,j),

f_{ij} is an original image gray level at pixel (i,j),

$\bar{f}_{ij}$ is a thresholded local mean value at pixel (i,j),

α is an adaptive fraction factor,

S is a scale factor (to deal with integer run-off), and

C is a dc bias value.

The thresholded local mean $\bar{f}_{ij}$ is computed by the two-dimensional, rolling-window method. The rolling-window average method is an overlap sectioning average processor (for reference, see Section 3.4, Number 2). The window sizes are chosen: 3 by 3, 5 by 5, and 7 by 7. In general, the smaller the window, there is less computing time and the more sensitivity to noise degradation; however, the larger the window, the better the statistical property. The zonal filtering algorithm was implemented with three window sizes in order to investigate the tradeoff between performance and computation time in the presence of noise degradation. Threshold levels T_L, T_U can be

3-3

chosen arbitrarily, regardless of the FLIR image histogram. As long as T_L is not equal to T_U, the processed image will be enhanced. Because the enhanced image value g_{ij} will lie between αf_{ij} and $(\Delta f_{ij} + \alpha f_{ij})$, where Δf_{ij} is defined as $(1 - \alpha)(f_{ij} - \bar{f}_{ij})$ and $\bar{f}_{ij}$ is defined as the local thresholded nonstationary mean instead of the local nonstationary mean.

Zonal filtering of enhanced images taken from Northrop's A. P. Hill data set are demonstrated in Figures 3-2 through 3-5, with Figure 3-3 showing different adaptive constants, Figure 3-4 showing bias C, and Figure 3-5 showing different window size. The zonal filtering enhanced images from the Fort Polk 1 data set are shown in Figures 3-6 through 3-8. The enhanced images from both data bases display detailed information on both the potential candidate targets and the background, so that the candidate targets are more conspicuous in the enhanced images than in the pre-enhanced images. In addition, the temperature gradient of the enhanced images is pulled out clearly to help the pilot more easily identify potential targets.

The experimental results also show that the zonal filtering is not very sensitive to the rolling window size, bias, and threshold levels of the zonal filter.

3.1.1.2 Edge Crispening – Statistical Differencing Operator – For referenced documents, see Section 3.4, Number 3 and 4. Edge crispening enhances the edge by using the results of psychophysical experiments. These experiments indicate that a photograph or visual signal with accentuated edge is often subjectively more acceptable than an exact photometric reproduction. The statistical differencing operator is one of the edge crispening techniques which forces the enhanced image to have second-order moment. The operator is defined by:

$$g_{jk} = (f_{jk} - \bar{f}_{jk}) \frac{A_{\sigma d}}{A\sigma_{jk} + \sigma_d} + (\alpha_{Md} + (1 - \alpha)\bar{f}_{jk}), \qquad (3-3)$$

where Md and Ad are desired mean and standard deviation respectively. A is a gain factor: σ_{jk} is a local standard deviation at (j,k) pixel (the center pixel of a 7 by 7 window that is generated by a two dimensional, 7 by 7, rolling window averaging processor), and α is a proportionality factor controlling the ratio of the edge to background composition of the enhanced image. The contrast gain is a function of the local standard deviation and is bounded as shown in Figure 3-9.

6288-14

Figure 3-2. Original FLIR Image of A.P. Hill Data Set
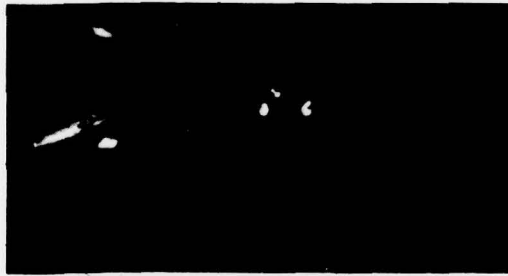
(A) ADAPTIVE CONSTANT $\alpha = 0.8$

(B) ADAPTIVE CONSTANT $\alpha = 0.2$ 6288-18

Figure 3-3. Enhanced A. P. Hill Images Using Zonal Filtering Enhancement with
a Different Adaptive Constant

3-5

(A) BIAS C = 30

(B) BIAS C = 60   6288-16

Figure 3-4. Enhanced A. P. Hill Images Using Zonal Filtering Enhancement with a Different Bias

(A) ROLLING WINDOW SIZE 3X3
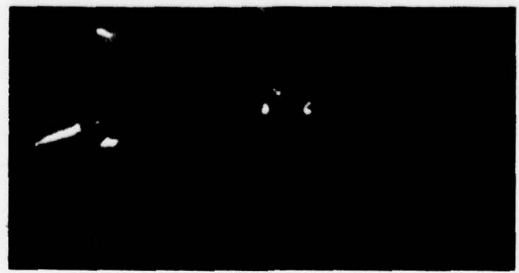
(B) ROLLING WINDOW SIZE 5X5   6288-17

Figure 3-5. Enhanced A. P. Hill Images Using Zonal Filtering Enhancement with a
Different Rolling Window Size

6288-18

Figure 3-6. Original FLIR Image from Fort Polk 1 Data Set

(A) ADAPTIVE CONSTANT $\alpha = 0.8$

(B) ADAPTIVE CONSTANT $\alpha = 0.2$ 6288-19

Figure 3-7. Enhanced Fort Polk 1 Images Using Zonal Filtering Enhancement with a
Different Adaptive Constant
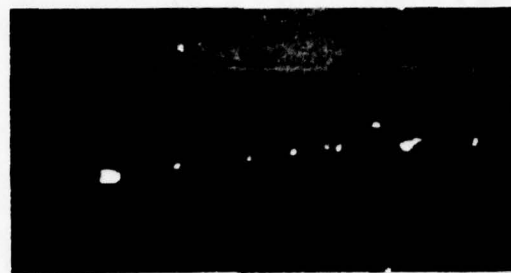
(A) ROLLING WINDOW SIZE 3X3

(B) ROLLING WINDOW SIZE 5X5   *6288-20*

Figure 3-8. Enhanced Fort Polk 1 Images Using Zonal Filtering Enhancement with a Different Rolling Window
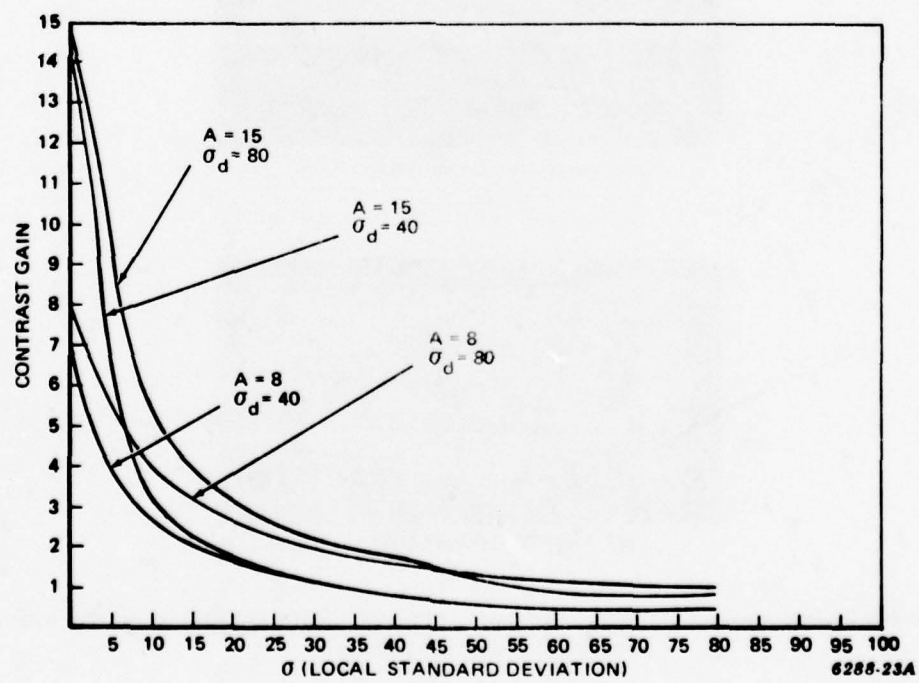
Figure 3-9. The Constrast Gain of SD Operator

In order to implement equation (3-3), we need to compute the local nonstationary mean $\bar{f}_{jk}$ and the local standard deviation σ_{jk}. The nonstationary mean and local standard deviation are computed using a two-dimensional, rolling-window technique. Images from the A. P. Hill data set enhanced by the statistical differencing operator are shown in Figures 3-10, 3-11, and 3-12. These have different desired mean and variance, rolling-window size, and adaptive constant, respectively. The enhanced images of Fort Polk 1 data are shown in Figures 3-13 and 3-14.

From these experimental results, it is found that this method extracts the detailed information of the candidate targets and background area, but the enhanced images have more noise in the background than unenhanced images. This occurs because the contrast gain is a function of the local standard deviation which is very sensitive to noise degradation. This operator is not sensitive to the rolling-window size. This method actually acts as a high pass filter to enhance the edge. This contrast gain is bounded to avoid saturation.

(A) DESIRED GLOBAL MEAN AND VARIANCE ARE Md_1 AND σd_1
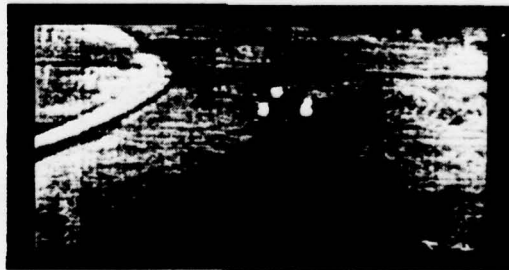
(B) DESIRED GLOBAL MEAN AND VARIANCE ARE Md_2 AND σd_2 6288-25

Figure 3-10. Enhanced A. P. Hill Images Using a Statistical Differencing Operator Enhancement with a Different Desired Mean and Variance

(A) ROLLING WINDOW SIZE 3X3

(B) ROLLING WINDOW SIZE 5X5   6288-26

Figure 3-11. Enhanced A. P. Hill Images of Using Statistical Differencing Operator Enhancement
with a Different Rolling Window Size

(A) ADAPTIVE CONSTANT $\alpha = 0.8$
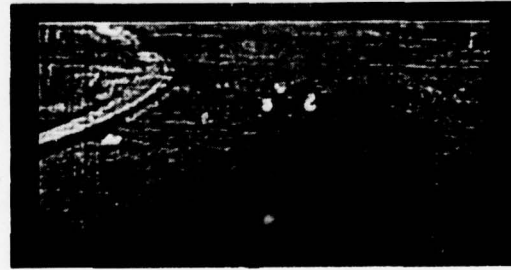
(B) ADAPTIVE CONSTANT $\alpha = 0.2$ 6288-24

Figure 3-12. Enhanced A. P. Hill Images Using Statistical Differencing Operator Enhancement

3-10
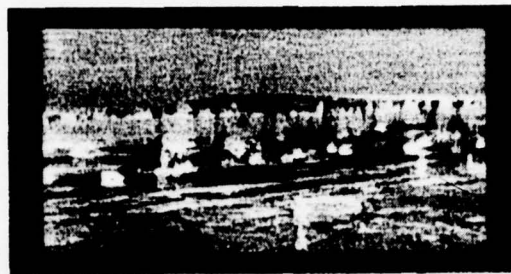
(A) ADAPTIVE CONSTANT $\alpha = 0.8$
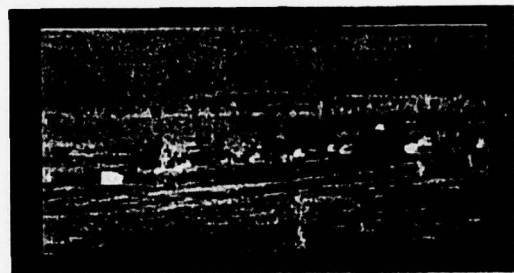
(B) ADAPTIVE CONSTANT $\alpha = 0.2$ 6288-27

Figure 3-13. Enhanced Fort Polk 1 Images Using Statistical Differencing Operator Enhancement with a Different Adaptive Constant
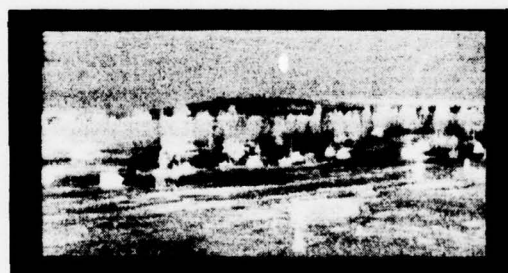
(A) ROLLING WINDOW SIZE 3X3
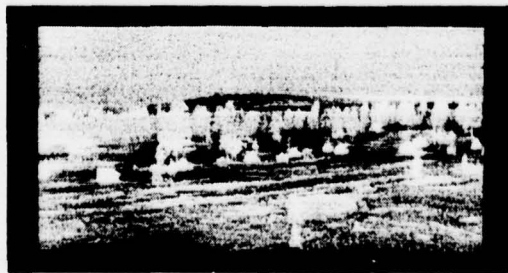
(B) ROLLING WINDOW SIZE 5X5   6288-28

Figure 3-14. Enhanced Fort Polk 1 Images Using Statistical Differencing Operator Enhancement with a Different Rolling Window Size

3.1.1.3 <u>Edge Crispening - Unsharp Masking Method</u> - For referenced documents, see Section 3.4, Number 3 and 4. The unsharp, masking method of edge crispening is a technique which employs an "unsharp masking" operator to enhance the image edge. This operator is defined as :

$$g_{jk} = Cf_{jk} - (1 - C) \bar{f}_{jk}, \tag{3-4}$$

or equivalently,

$$g_{jk} = h_u \otimes f_{jk}, \tag{3-5}$$

where:

f_{jk} is original image intensity,

$\bar{f}_{jk}$ is the low-pass filtered image,

C   is a proportionality constant,

$\otimes$ is two-dimensional convolution operator, and

h_u is the 7 by 7 unsharp mask

The low-pass filtered image $\bar{f}_{jk}$ is computed by the two-dimensional, 7 by 7 rolling-window average processor.

Enhanced images from both the A. P. Hill and Fort Polk data set are shown in Figures 3-15 and 3-16.

From experimental results, we have found that more detail information of the objects and the background is extracted because of accentuating the edge. This method also acts as a high pass filter to enhance image and it only needs compute first-moment for implementation.

This algorithm is a special case of the zonal filtering method.

3.1.1.4 <u>Prototype·Automatic Target Screener (PATS) Enhancement Technique</u> - For referenced documents, see Section 3.4, Numbers 5, 6, and 7. The PATS method is a technique which employs the local adaptive gain to different local regions in order

6288-29

Figure 3-15. Enhanced A. P. Hill FLIR Image of the Unsharping Mask Method with C = 5/3

6288-30

Figure 3-16. Enhanced Fort Polk 1 FLIR Image of the Unsharp Masking Method with C = 5/3

to enhance the contrast, in such a manner that the enhanced image can satisfy the psychovisual consideration (Weber's Law). The local adaptive gain A_{ij} is a function of global mean and local standard deviation. The enhanced image is defined:

$$g_{ij} = A_{ij} (f_{ij} - \bar{f}_{ij}) + \bar{f}_{ij}, \tag{3-6}$$

where the local gain

$$A_{ij} \triangleq \alpha \frac{M}{\sigma_{ij}}, \quad 0 < \alpha < 1,$$

and where M is the global mean,

f_{ij} is input image intensity of the (i,j) pixel,

$\bar{f}_{ij}$ is a nonstationary mean of the (i,j) pixel, and

A_{ij} is a local standard deviation of the (i,j) pixel.

3-13

The local nonstationary mean f_{ij} and local standard deviation A_{ij} can be computed by the two-dimensional, 7 by 7 rolling-window averaging technique.

The experimental results of the PATS technique are shown in Figures 3-17 and 3-18.

From experimental results, we have found that the enhanced images extract more information of both target objects and background but it trades more background noise for the better contrast. This occurs because the contrast gain is a function of the local standard deviation which is very sensitive to noise. This technique needs to compute both the first moment and second moment for implementation.

6288-31

Figure 3-17. Enhanced A. P. Hill Image Using PATS Enhancement Technique with Adaptive Constant $\alpha = 0.8$

6288-32

Figure 3-18. Enhanced Fort Polk 1 Image Using PATS Enhancement Technique with Adaptive Constant $\alpha = 0.2$

3.1.1.5 <u>Constant Variance Enhancement (CVE)</u> - For reference documents, see Section 3.4, Number 8. The CVE enhancement is a technique which employs a high pass filtering to reduce the local average to zero for all regions of the picture and applies a contrast gain factor equal to the reciprocal of the local standard deviation to produce an enhanced image in which all local regions have equal variance.

The enhanced image is defined

$$g = \frac{f - f \otimes W}{\left[(f - f \otimes W)^2 \otimes W\right]^{1/2}} , \qquad (3-7)$$

or equivalently,

$$g_{ij} = \sqrt{\frac{\sigma_d}{\sigma_{ij}}} \ (f_{ij} - \bar{f}_{ij}), \qquad (3-8)$$

where

$\quad$ f is the input image intensity,

$\quad \otimes$ is the two-dimensional convolution operator.

$\quad$ W is the spatial weight function,

$\quad f \otimes W$ is the local nonstationary mean,

$\quad (f-f*W)^2 \otimes W$ is the local variance,

$\quad \sigma_d$ is the desired standard deviation, and

$\quad \bar{f}_{ij}$ is the local nonstationary mean at (i,j) pixel.

The nonstationary mean $\bar{f}_{ij}$ and the local variance A_{ij} are computed by the above mentioned two-dimensional, rolling window averaging technique. The spatial weighting function W is a cube function. The experimental results are shown in Figures 3-19 and 3-20.

From experimental results, we have found that enhanced images so overly exhibit detail information of the candidate targets and background that the object clarity is obliterated. This occurs because this algorithm is entirely dependent upon the local standard deviation which is very sensitive to noise, thereby degrading the image.

This method also needs to compute the first moment and second moment for implementation.

3.1.1.6 <u>Histogram Equalization</u> - For referenced documents, see Section 3.4, Number 3 and 9. Histogram equalization is a technique by which all brightness levels are redistributed within the available dynamic range as equally as possible in order

6288-33

Figure 3-19. Enhanced A. P. Hill FLIR Image Using Constant Variance Enhancement

6288-34
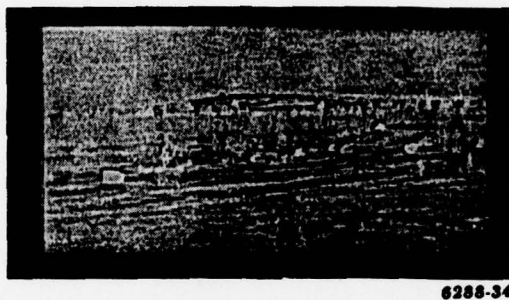
Figure 3-20. Enhanced Fort Polk 1 FLIR Image Using Constant Variance Enhancement

to avoid information losses. The resultant uniform distribution density of the enhanced image is the maximum entropy case. Thus, the histogram equalization technique maximizes the zero-order brightness entropy. Specifically, this technique yields images of increased intelligibility.

The block diagram of the histogram equalization system is shown as Figure 3-21.

This process can be considered to be a monotonic point processor for which the input intensity variable $f_o \leq f_j \leq f_J$ is mapped into an output variable $g_o \leq g_k \leq g_K$ in such a manner that the output probability distribution density $P_g(g)$ is of uniform distribution density. Thus, the histogram equalization transfer function is:

$$g = \left[g_{max} - g_{min} \right] P_f(f) + g_{min}, \tag{3-9}$$

where

$$P_f(f) \triangleq \int_0^f p_f(f) \, df \ .$$

3-16

$$f_j \qquad T\{f_j\} \qquad g_k$$
$$p_{f(f)} \qquad\qquad\qquad P_{g(g)}$$

6288-64
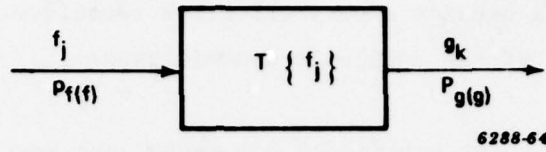
Figure 3-21. Block Diagram of Histogram Equalization Enhancement System

In order to implement equation 3-9, we need to compute the one-dimensional histogram of input intensity and find the values of g_{min} and g_{max}.

The experimental results are shown in Figures 3-22 and 3-23.

From experimental results, we have found that the enhanced images are so overly enhanced the local region contrast that obscure some local clarity of the image. Clearly, the image with more entropy is not necessary the better image.

6288-35
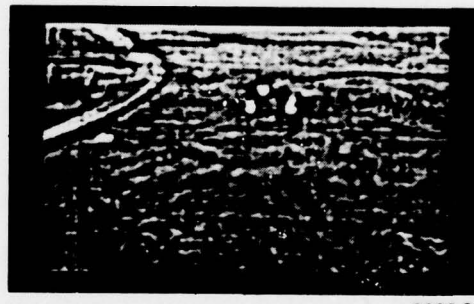
Figure 3-22. Enhanced A. P. Hill Image Using Histogram Equalization Method

6288-65
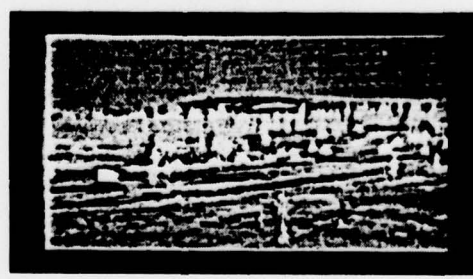
Figure 3-23. Enhanced Fort Polk 1 Image Using Histogram Equalization Method

Histogram equalization is usually a very effective technique, however, when the image occupies a small portion of the available dynamic range.

3.1.1.7 <u>1/64 Law Method</u> - For referenced documents, see Section 3.4, Number 12. An enhancement technique under development at Northrop uses an optimal statistical argument to arrive at the output relation:

$$g_{ij} = K_1 \frac{f_{ij} - \bar{f}_{ij}}{\sigma_{ij}} + K_2 \tag{3-10}$$

where

g_{ij} is the enhanced image

f_{ij} is the input image

$\bar{f}_{ij}$ is the nonstationary mean

σ_{ij} is the local variance

K_1 is a gain factor

K_2 is a bias factor

K_1 and K_2 are derived by determining the optimum gain and bias required in the input image to properly place (on the average) a Rayleigh probability distribution across the 64 gray levels available in the output display. Since the optimization process is performed on an average for all time basis, the factors K_1 and K_2 may be fixed well before any test image is encountered. The results of applying this technique to two FLIR scenes is shown in Figures 3-24 and 3-25.

3.1.2 Evaluation of FLIR Image Enhancement Effectiveness

For referenced documents, see Section 3.4, Numbers 3 and 10. All the above candidate enhancement techniques were implemented on USC's DEC KL-10 computer and

6288-36

Figure 3-24. Enhanced A.P. Hill Image Using 1/64 Law

6288-37

Figure 3-25. Enhanced Fort Polk Image Using 1/64 Law

the enhanced images are displayed on USC's Comtal display system. In addition, all the enhanced image photo prints in this section were generated by USC's Dicomed photo system in order to preserve good quality of enhanced image.

Enhancement is performed on a picture to present additional information or insight to the viewer. Determination of the quality of enhanced images by psychophysical experiments is a means of evaluating the effectiveness of the enhancement techniques. There are two general types of subjective evaluations. In one, absolute evaluation, observers are shown an enhanced image and asked to rate it according to a predefined scale. The other, relative evaluation, simply requires the observer to rank from best to worst, a set of enhanced images. The relative evaluation has been adopted because it is a fairly quick and easy test to perform, and it requires no training or familiarization tasks.

Northrop has conducted relative psychophysical evaluations using 21 observers and totaled the resulting ranks. Each observer was instructed to perform a relative eval-

3-19

uation of the same set of pictures based on total scene information content, visibility of scene detail, object clarity (included target and nontarget object), artifacting, sharpness and contrast of target and background area, and natural rendition of the scene.

This experiment was conducted using two different images: a Northrop-digitized A. P. Hill frame, and a member of the standard Fort Polk data set. The resulting ranks are consistent. The rank for each technique is shown in Table 3-1. the top ranked techniques are the variable threshold zonal filtering, PATS's enhancement technique, and unsharp masking enhancement, in this order.

3.1.3 Conclusion

We have investigated and implemented seven candidate techniques of image enhancement. The most effective techniques for image enhancement are utilization of high pass filtering for edge crispening and locally varying scaling for contrast stretching. All the enhancement techniques are dependent on the local nonstationary mean, or local variance, or both to achieve edge enhancement or contrast stretching in local regions. The local nonstationary mean and the local variance in each case may be a two-dimensional, rolling window average processor.

The zonal filering method, PAT'S method, and unsharp masking methods are combinations of high pass filtering and linear contrast, stretching in a local region. These three methods have been shown to be more effective than the others.

In addition, the adaptive weighting factors used in zonal filtering enhancement, PAT's enhancement, and the unsharp masking operator enhancement. can be optimized to achieve the best enhanced image quality in the sense of subjective criterion. Each of the three top ranked approaches: variable threshold zonal filtering, PAT's enhancement and unsharp masking, will be investigated during the next quarter to determine ease of implementation. The best combination of performance and complexity will then be selected for the Automatic Target Cuer (ATC).

Table 3-1. Subjective Evaluation Results of All Seven Enhancement Techniques

Enhanced Method	Original	Zonal Filter 1	Zonal Filter 2	Statistical Differencing	Histogram Equalization	Constant Variance	PAT's	Unsharp Masking	1/64 Law
a. Fort Polk Image									
Evaluated Scores	78	65	46	142	132	180	46	98	158
Rank*	3	2	1	6	5	8	1	4	7
b. A. P. Hill Image									
Evaluated Scores	97	105	40	142	146	162	72	67	111
Rank*	4	5	1	7	8	9	3	2	6

*Based on sum of rank rated by 21 observers.

3.2 TARGET SILHOUETTING

The silhouetting function receives location data from the detector, fetches the candidate subframe from the frame store memory, and passes resultant target silhouettes to the classifier. The fundamental requirement imposed on the silhouette is that it sends to the classifier a separable region from the image which represents the "target" within the candidate region. Obviously, multiple or distorted silhouettes will have a detrimental effect on classifier performance. In addition, the elimination of system noise is a fundamental requirement of the silhouetter. The types of noise the silhouetter will receive are: (1) image noise which makes the true silhouette hard to find, and (2) subframes comprised entirely of noise. Proper identification of this second type of noise will allow the reduction of total system false alarms.

The silhouetting system being evaluated for the ATC is based on the University of Maryland 'Superslice' system. See referenced documents, Section 3.4, Number 11. This section describes the algorithms that comprise Northrop's implementation of the Superslice system. This implementation differs from the University of Maryland's in that connected component analysis and containment trees are not utilized. These functions are currently omitted from the silhouetter but are planned for inclusion in the next quarter. Also, since the University of Maryland's Superslice system was developed using a single NV&EOL data set, a set of experiments is performed using a sampling from other NV&EOL data sets to evaluate the performance of the smoothing and edge detection functions of the system.

3.2.1 Superslice

The general algorithm construction of the superslice system is displayed in Figure 3-26. An image subframe is first extracted from the full frame image by the target detector and presented to the silhouetting system. The subframe is operated by a smoothing algorithm to produce a smooth image, and to decrease spurious noise contributions.

The output of the smoother is routed to three separate paths to yield the required inputs for the blob selection function. The first data path consists of an edge

3-22
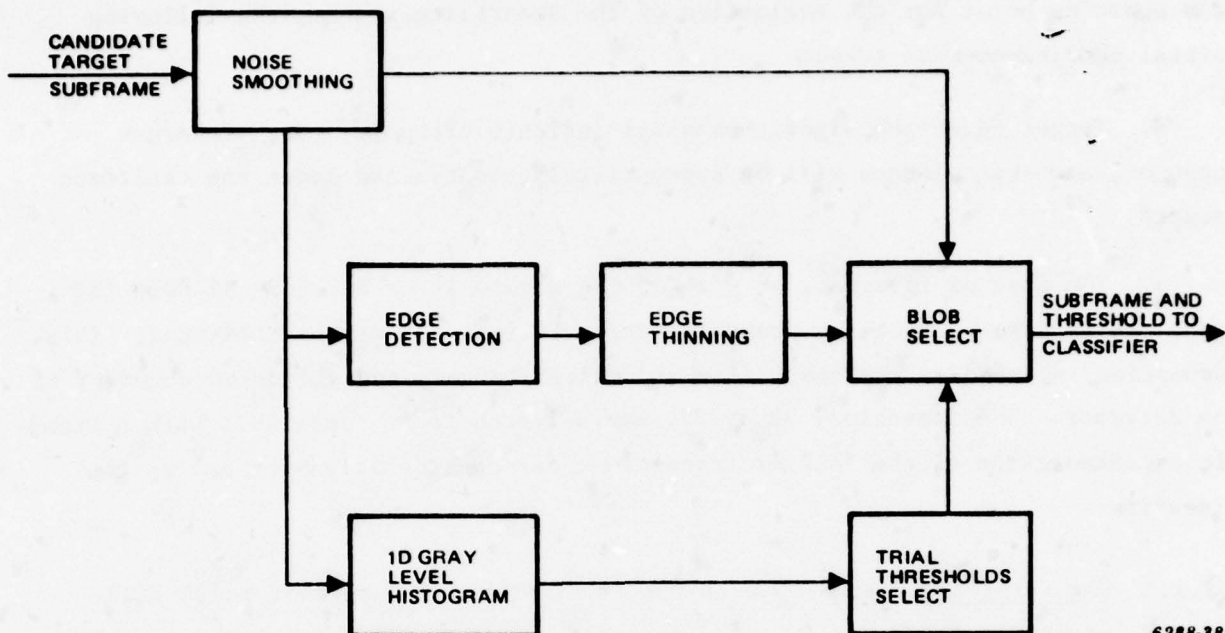
Figure 3-26. Northrop — University of Maryland Superslice Program

detection function, followed by a thinning operation. The edge detection algorithm calculates the edge map of the image subframe and the thinning function thins the resultant edge map using both edge amplitude and direction information. The result of this functional path is then a thinned edge map which is ready for input into the blob selection algorithm. The second functional path computes the one-dimensional, gray-level histogram. The third path passes the smooth image directly to the blob selection process.

The blob selection routine is the final function of the thresholding system. This function receives the thinned edge map and a set of trial thresholds and determines the number of coincidence points between the edge map and the boundary points of the thresholded image. This operation is performed for each threshold in the trial set. A merit figure based on the number of coincident points is also determined. At the end of the blob selection procedure, the trial threshold with the greatest figure of merit, is output to the classifier, along with the smoothed input subimage. Furthermore, it is possible to send all thresholds and their respective figures of merit to the classifier for containment tree analysis.

As a starting point for the evaluation of the superslice system, the following initial conditions were taken:

a. Target detection algorithms shall indicate probable areas of target location, and that windows will be appropriately constructed about the candidate targets.

b. The area of interest, or size of the window is to be 32 by 32 pels in size. It is assumed that the probable target is enclosed within this area. This assumption is based on the small size of desired targets and projected accuracy of the detector. The dimension, 32 by 32, was selected to be compatible with a standard implementation of the Fourier transform under consideration for use in the classifier.

3.2.1.1 <u>Smoothing Algorithm</u> - Due to the inherent noisy nature of input FLIR imagery, smoothing is required in the superslice system. Spatial image smoothing is used for three reasons. First, the smoothing operation increases the probability of identical treatment of points that belong to the same region. Secondly, insignificant local contrast changes are eliminated. Thirdly, the statistical properties of a smoothed image are closer to the true situation than the received noisy image, thereby, rendering more accurate threshold decisions based on statistical properties (i.e., histograms).

Four candidate images from four NV&EOL data sets were selected to evaluate the basic silhouetting approach. These frames contained a large target, small target, an embedded target and a noise frame. As a starting set, these represent the variance of the basic types of targets expected.

Two methods were considered: mean and median filtering. Mean filtering replaces a pel value by the mean of its neighborhood, while median filtering replaces the pel by the median of the neighborhood. Averaging or blurring may cause some small objects to become less well defined, while median filtering does preserve edges, yet rounds off sharp corners.

The results of both smoothing procedures (5 by 5 neighborhood) for each input image case are presented in Figure 3-27. The format for the output images shown in Figure 3-27 is (1) upper left hand image is original, (2) lower left hand image

MEAN FILTERED   MEDIAN FILTERED
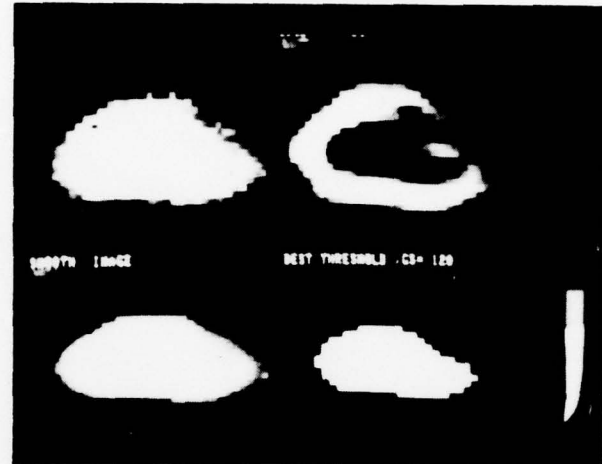
LARGE TARGET
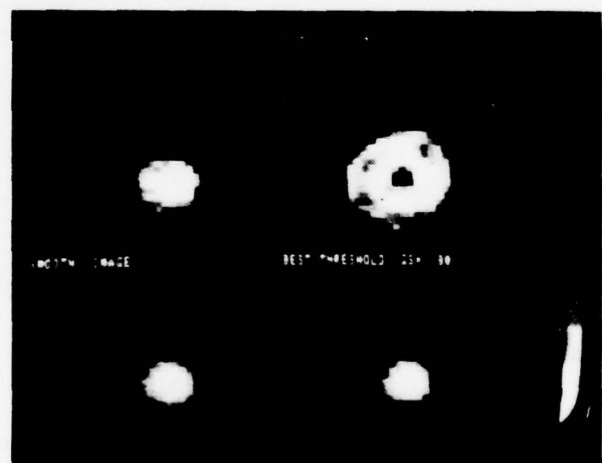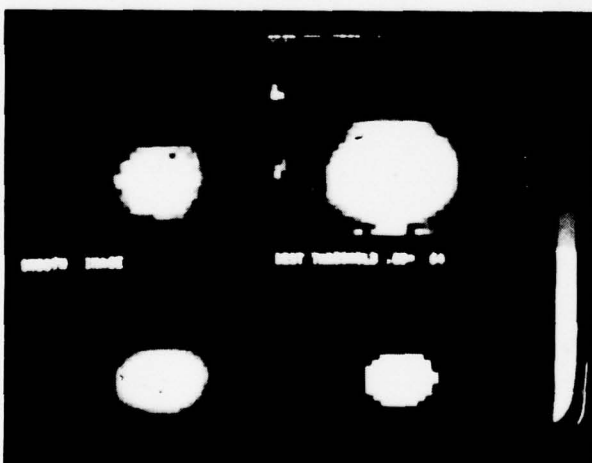
SMALL TARGET   6288-39(A)

Figure 3-27. Effects of Smoothing (Sheet 1 of 2)

3-25

MEDIAN FILTERED

MEAN FILTERED

NOISE FRAME

EMBEDDED TARGET

6288-39C

Figure 3-27. Effects of Smoothing (Sheet 2 of 2)

3-26
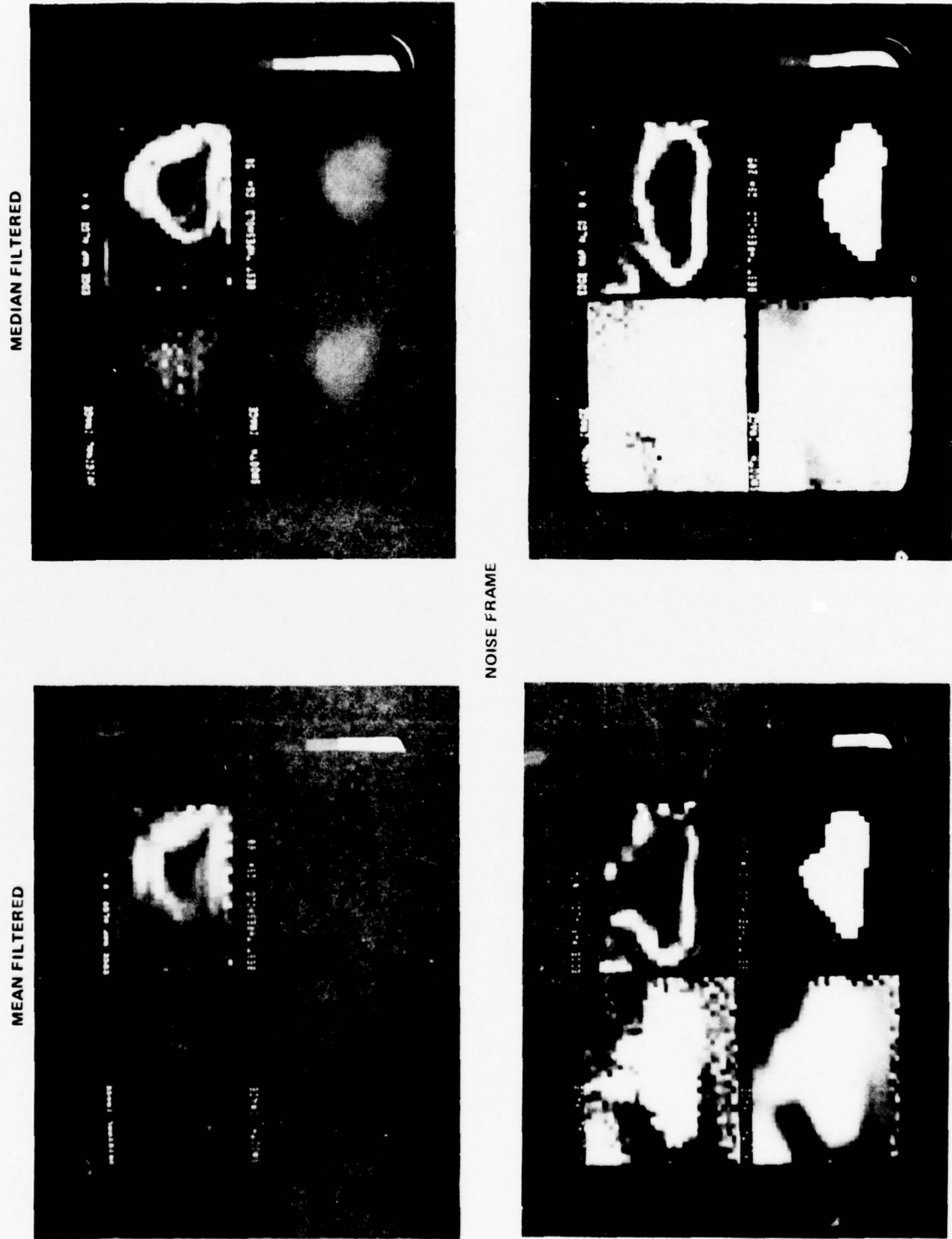
is smoothed, (3) upper right hand image is edge map (not thinned), and (4) lower right hand corner image is the resultant silhouette. The edge detector used to generate these images was a 2 by 2 neighborhood operator. The edge thinning procedure was the non-maximum supression algorithm.

As shown in the photographs, the median filtered image produced silhouettes that were generally more structured or object-like than those produced with mean filtering. Also, note that for mean filtering the selected blob in the noise frame is not representative of the input image while median filtering pulls out the weak false blob rather well. Based on these results median filtering is selected for the baseline superslice system.

3.2.1.2 <u>Edge-Detection Algorithm</u> – Four edge-dectection procedures were also evaluated. They were (1) the 2 by 2 neighborhood operator used by the University of Maryland, (2) the Roberts operator, (3) the Laplacian, and (4) the Sobel operator. The mask of each edge operator is shown in Figure 3-28.

1. <u>LAPLACIAN</u>:

a b c
d $\circledcirc$ f
g h i

$D'_L = |e - (a + b + c + d + f + g + h + i)/8|$

2. <u>ROBERTS</u>

a b
c $\circledcirc$

$D'_R = MAX\{|a - d|, |b - c|\}$

3. <u>2 X 2 DIFFERENCE</u>

VERTICAL   HORIZONTAL

b c
$\circledcirc$ f
h i
v w

d $\circledcirc$ f t
g h i u

$P'_{1X2} = 1/4\ MAX\ \{|VERT| . |HORIZ|\}$
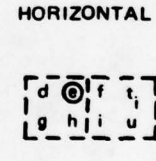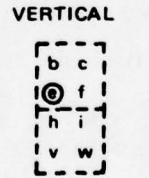
4. <u>MAGNITUDE OF SOBEL</u>

SOBEL MASKS

1 0 −1   1 2 1
2 0 −2   0 0 0
1 0 −1   −1 −2 −1
  <u>V</u>   <u>H</u>

$D'_{MS} = |V| + |H|$

6288-40A

Figure 3-28. Edge Detection Procedures

The silhouettes obtained by using each of the edge operators in the four test images are shown in Figure 3-29. In addition, Median smoothing and nonmaximum thinning were used to generate the silhouettes.

Examination of the edge maps produced shows that both the 2 by 2 Neighborhood and Sobel operators generate, in general, a smooth broad line. This is desirable when the edge map is used as input to a thinning algorithm that looks for edge points with immediate neighbors. Although the Roberts and Laplacian operators produce edge maps that are not as full, both have a large spatial extent and would, therefore, still require thinning. An algorithm that thins the output of the Roberts and Laplacian would require a larger spatial mask than one that thins the output of the Sobel and 2 by 2 neighborhood.

The Sobel operator and 2 by 2 neighborhood operator produce comparable silhouettes from the input test set. The 2 by 2 neighborhood operator, however, is easier to implement in hardware than the Sobel. For this reason, the 2 by 2 neighborhood operator has been selected for the superslice system.

3.2.1.3 - Edge Thinning - Edge thinning is performed using the University of Maryland's non-maximum supression technique. For every edge point on the edge map, the associated edge direction is first examined and a mask having its major axis normal to the edge direction is selected. The masks used are illustrated in Figure 3-30. The edge points designated by an 'x', in the selected mask, are then examined. If any point in the mask has an edge value greater than that of the center point, the center point edge value is set to zero.

3.2.1.4 Trial Threshold Selection - Trial threshold selection is performed using information derived from the 1-D histogram. Four thesholds are selected from the first four local minima or "valleys" of the histogram in descending order, whose gray value is less than maximum and greater than that of the mode or peak value. If four valleys are not found, the remaining trial thresholds are spread evenly across the gray level range from the first valley to the maximum gray value. If no valleys are found, the trial thresholds are spread evenly across the range from the mode of the histogram to the maximum gray value. Implicit in this method is the assumption that the peaks of the histogram represent regions of uniform brightness and that the valleys that separate the peaks make good candidate threshold values.
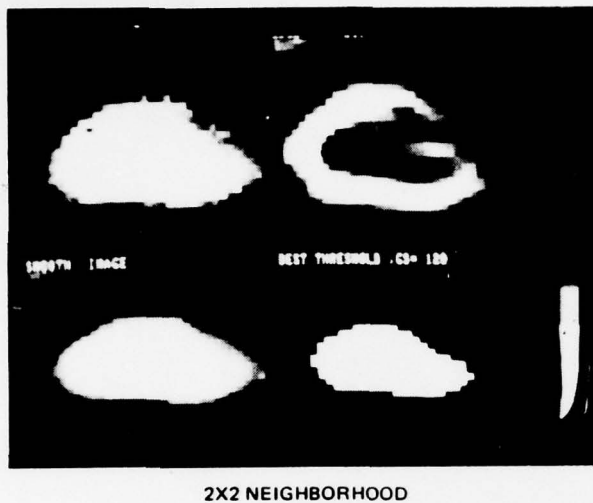
2X2 NEIGHBORHOOD
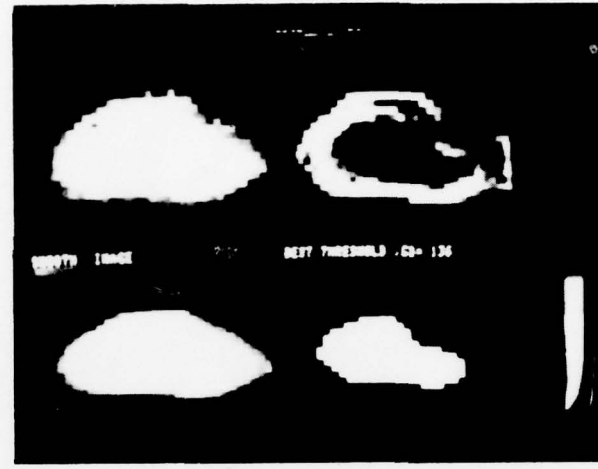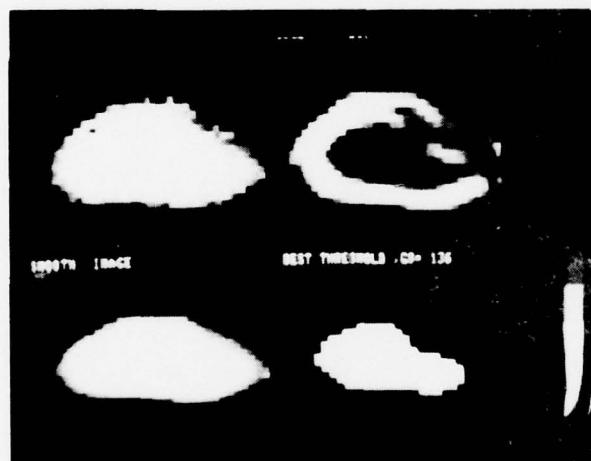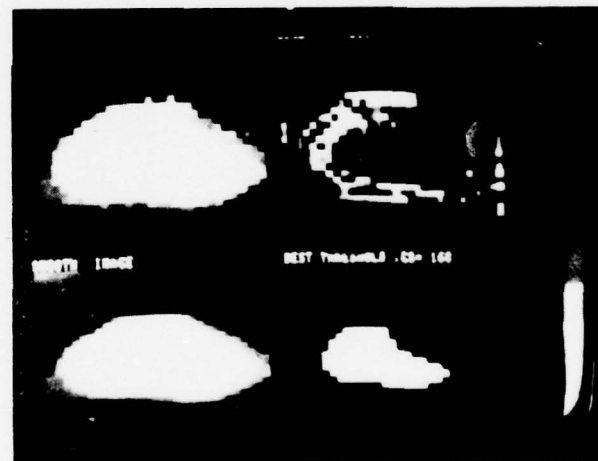
ROBERTS

SOBEL

LAPLACIAN

(A) LARGE TARGET

6288-41

Figure 3-29. Effects of Edge Operator (Sheet 1 of 4)
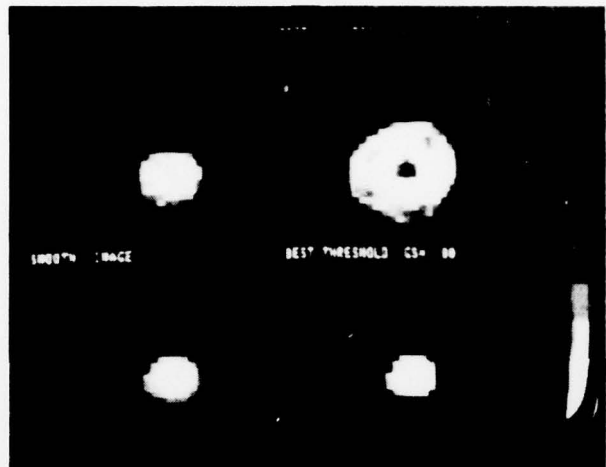
2X2 NEIGHBORHOOD
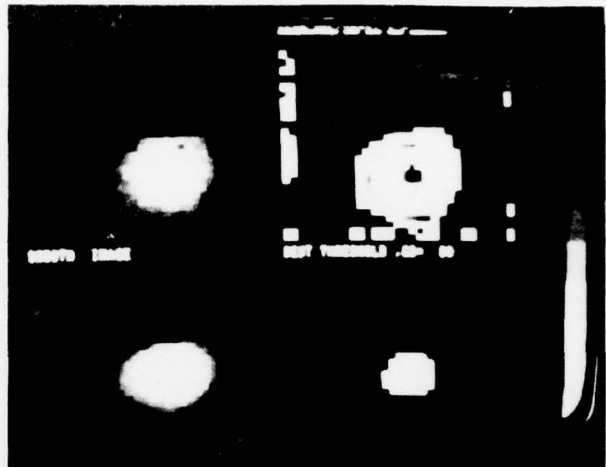
ROBERTS
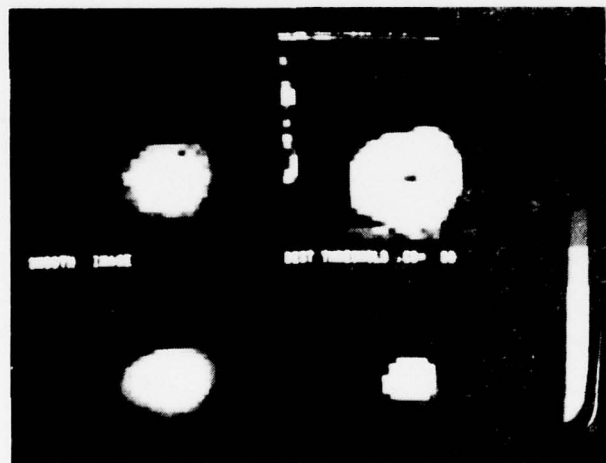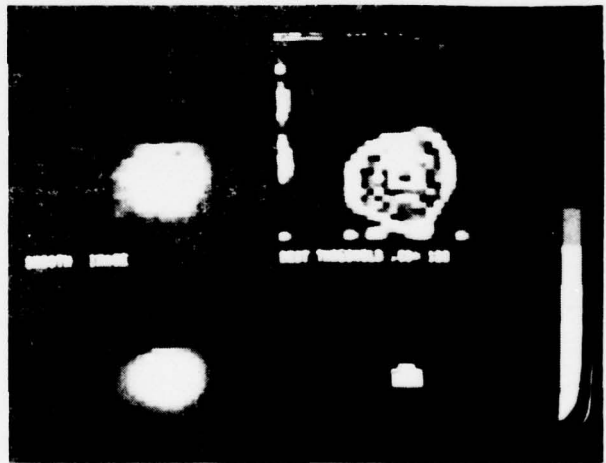
SOBEL

LAPLACIAN

(B) SMALL TARGET

6288-42

Figure 3-29. Effects of Edge Operator (Sheet 2 of 4)

ROBERTS

LAPLACIAN

6288-43A

(C) NOISE FRAME
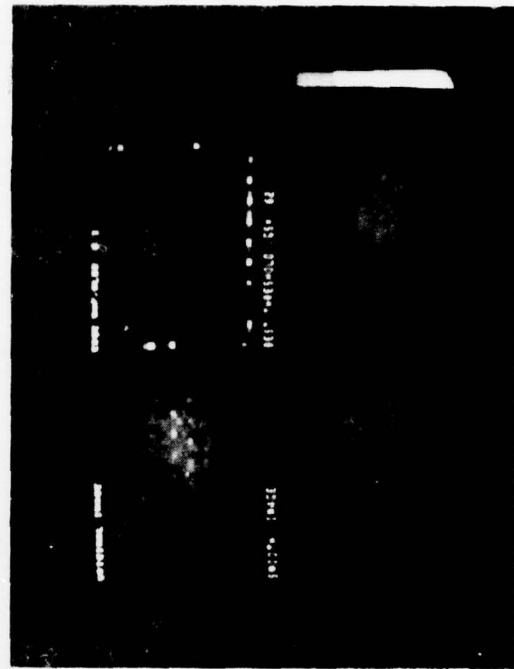
2 X 2 NEIGHBORHOOD

SOBEL

Figure 3-29. Effects of Edge Operator (Sheet 3 of 4)

ROBERTS

LAPLACIAN

6285-41A

2 X 2 NEIGHBORHOOD

SOBEL

(D) EMBEDDED TARGET
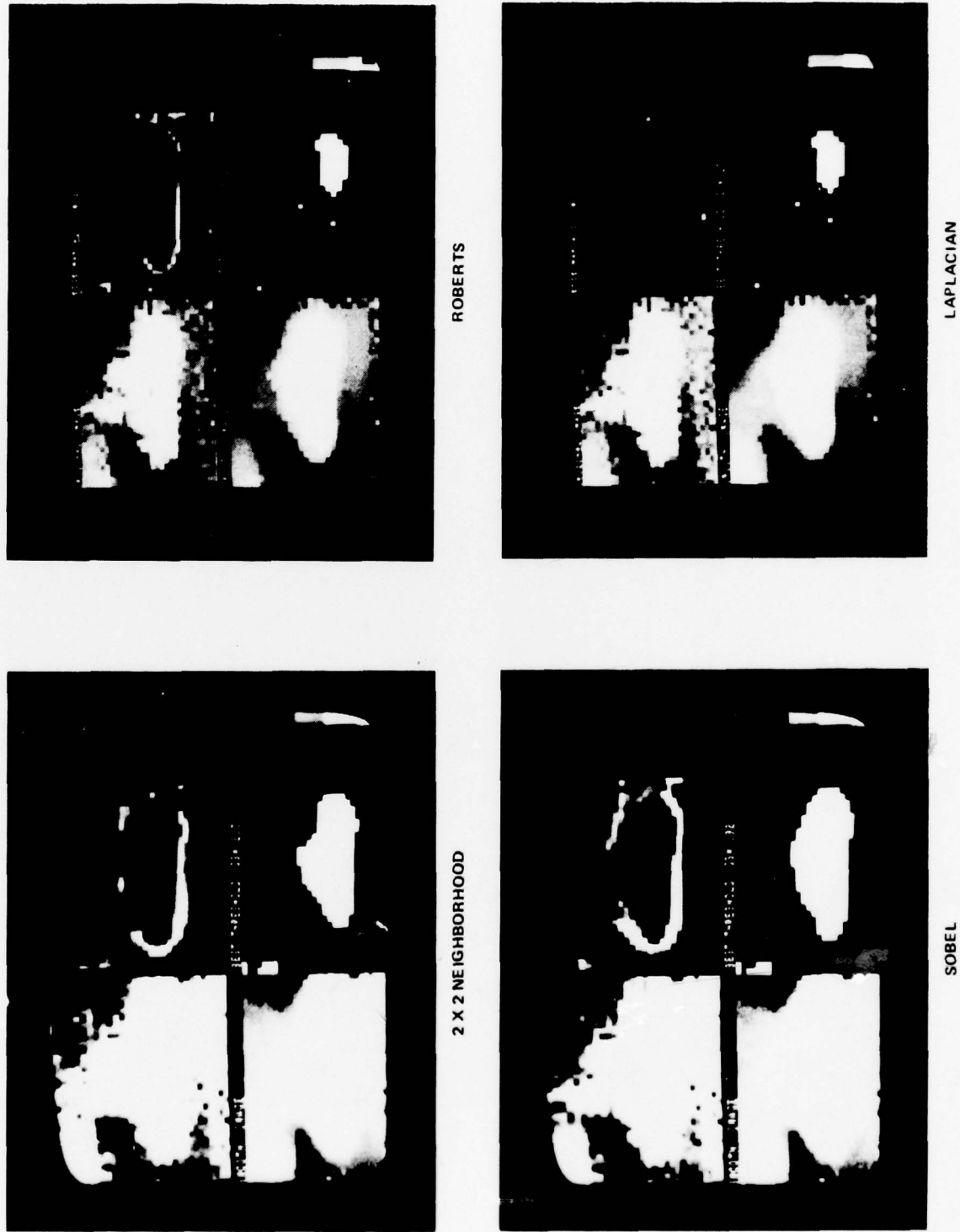
Figure 3-29. Effects of Edge Operator (Sheet 4 of 4)

RULE: POINTS IN CENTER, 'O' LOCATION, ASSIGNED TO O IF ANY
POINT WITHIN MASK HAS GREATER RESPONSE

6288-45

Figure 3-30. The Non-Maximum Suppression Masks

Figure 3-31 illustrates the selection of thresholds for two histograms. The mode is located at f_o on the ordinate scale and t_i, i = 1 through 4 represents the thresholds selected.

In Figure 3-31A four valleys to the right of the mode are found and the corresponding gray values become the trial thresholds. In Figure 3-31B, however, there are no valleys, so the four trial thresholds are spread evenly across the range from the mode to the maximum value.
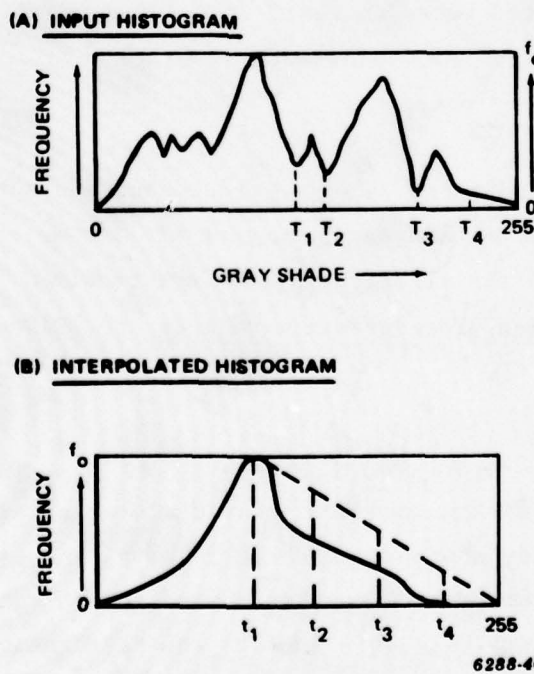
Figure 3-31. Threshold Selection

3.2.1.5 <u>Blob Selection</u>. The selection of a proper target silhouette is performed by optimizing thinned-edge, border-point coincidence over the image subframe. As a preliminary to optimize the edge-border coincidence, the border points of a trial silhouette must be found. This is accomplished by examining each point in the trial silhouette to see if any one of its four nearest neighbors are outside the silhouette. If so, then that point is defined as a border point. An illustration of the edge-border coincidence process is given in Figure 3-32. Part A illustrates the thinned edge map. Part B shows a single border map given by the border points resulting from a trial threshold applied to the smooth image. The coincidence points between the two maps are flagged by asterisks. The resultant figure of merit is defined as the coincidence ratio and is defined by the number of coincident points divided by the number of thinned edge points. The coincidence ratio for parts A and B of Figure 3-32, for example, is 8 to 11. Figure 3-32C illustrates a sequence of border-thinned edge comparisons for one image and a set of trial thresholds.

3.2.2 Summary

A silhouetting system based on University of Maryland's Superslice system has been simulated and some options within the algorithm, namely smoothing and edge detection, have been selected based on tests from a diverse data sample. A 5 by 5 median filter is the preferred smoothing method, while edge detection is performed using the 2 by 2 neighborhood operator.

During the next quarter, component labeling procedures and shrink/expand type, object-thinning methods to be used on the output of blob selection will be investigated. These additions to the algorithm system are required in cases where the output of the blob selection procedure is more than one silhouette.

3.3 CLASSIFIER TRADES

The classifier in the ATC system receives individual target silhouettes from the target silhouetter, computes appropriate shape features, and assigns a target class to the silhouette. This information is then passed to the target annotator for creation of display symbology. In this section the performance of two candidate approaches for computing target shape features is examined. The structure of the classification tasks, based on these features, is presented in the appendix.

(A) THINNED EDGE MAP

```
0  0  0  0  0  0
0  1  1* 1* 0  0
0  1* 0  0  1* 0
0  1* 1  0  1* 0
0  0  1* 1* 0  0
0  0  1  0  0  0
0  0  0  0  0  0
```

(B) THRESHOLDED BORDER MAP

```
0  0  0  0  0  0
0  0  1* 1* 0  0
0  1* 1  0  1* 0
0  1* 0  0  1* 0
0  0  1* 1* 1  0
0  0  0  0  0  0
0  0  0  0  0  0
```

(C) SEQUENCE OF TRIALS FOR ONE IMAGE

EDGE THRESHOLD:

COINCIDENCE RATIO	COUNT	THRESHOLD
0.038086	39	64
0.119141	122	128
0.081289	73	192
0.000000	0	256

MAXIMUM COINCIDENCE = 0.119141
BEST THRESHOLD = NO.   2 GRAY SHADE – 128

6288-47A

Figure 3-32. Blob Selection

3.3.1 Design Goals

The features used to classify target silhouettes should exhibit the following characteristics:

a. They must lead to a process that is invariant to rigid target motion, within the scene, i.e., rotation of the target shape due to platform dynamics, scale change due to changes in range, and variations of the target's position within the raster.

b. They must be relatively easy to compute. Straightforward measures based on the target silhouette are desirable in a digital, computer-based system.

c. The target feature space must have a low dimensionality. The target features must have a high power discrimination even though the number of features is low.

The first of these design goals, invariance, is surveyed briefly in Table 3-2 for some readily available feature sets. In the table, features 2 and 3 are taken from the University of Maryland features (for referenced documents, see paragraph 3.4, Number 11) while features 4 and 5 are transform features under investigation at Northrop.

Table 3-2. Shape Feature Invariance

Feature	Scale	Rotation
1. Area	NO	YES
2. Height/Width	YES	NO
3. Height/Width/Area	YES	NO
4. Discrete Fourier Transform Energy	NO	YES
5. Mellin Transform Energy	YES	YES

3.3.2 Feature Experiment

Two candidate feature sets, Northrop's Fourier set and the University of Maryland's, were selected for further evaluation. This section will give a brief overview including the sample data base used to evaluate their relative performance, and the results of the experiment.

3.3.2.1 Candidate Target Features - The Northrop Fourier features used in this experiment are described in referenced documents, paragraph 3.4, Number 13. Briefly, they involve a summary of the distribution of energy within a two-dimensional, Fourier transform of a candidate target's silhouette. The University of Maryland's features are basically geometric, using for example, height to width ratios, area to perimeter ratios, and some brightness distribution statistics. Specific definitions of the University of Maryland's features are presented in Table 3-3.

3.3.2.2 Image Data Base - The target-image data base used in this experiment consisted of side views of Armored Personnel Carriers (APC's), jeeps, and tanks. A breakdown of each target type and the NV&EOL-supplied data sets is shown in Table 3-4.

Each target image was silhouetted by eye, by manually adjusting a gray-scale threshhold until a subjectively appropriate silhouette was obtained. The resultant silhouettes are shown in Figure 3-33. Table 3-5 shows the raw feature measurements obtained from the 32 target images for each of the five Fourier descriptors. The images are numbered arbitrarily from 1 to 32. Another number is shown which references the particular image in the global FLIR target data base. Target class is
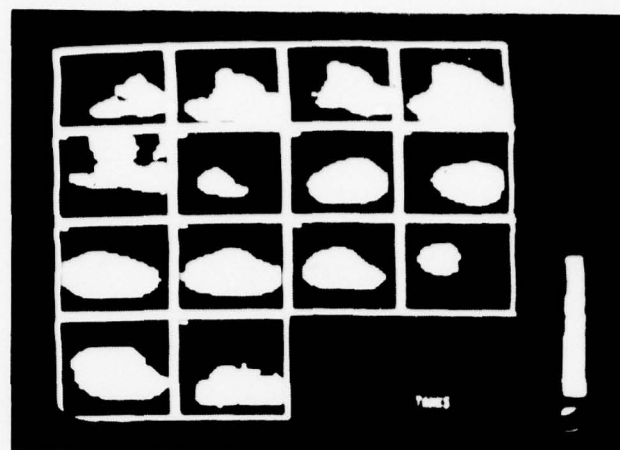
TANKS
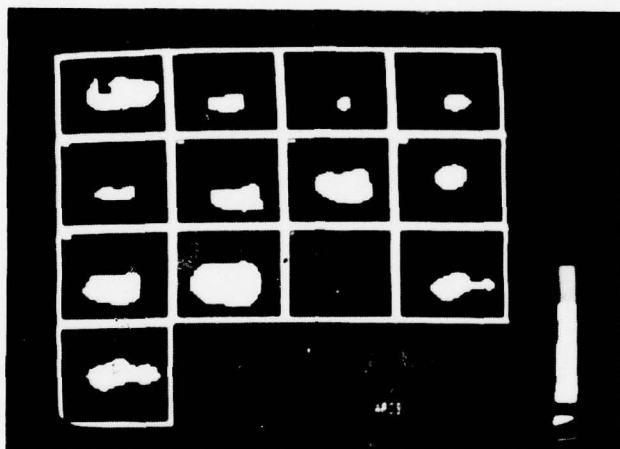
APC'S
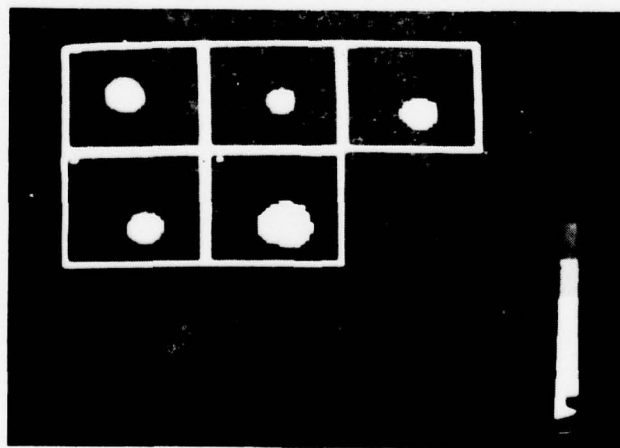
JEEPS

6288-48

Figure 3-33. Target Silhouettes

3-37

Table 3-3. Maryland Shape Features

1. h/w Y_{AVE}/X_{AVE}

2. $(H/w)'N$ $\left(|X_{AVE}-.8*Y_{AVE}|/\sqrt{X_{AVE}*Y_{AVE}}\right)N$

3. $(h*w)*N$ $\left(X_{AVE}*Y_{AVE}/N\right)*N$

4. $((h+w)/P)*N$ $\left[(X_{AVE}+Y_{AVE}-4)/P\right]*N$ } shape

5. Diff $(SX^2-SY^2)/R^2$

6. Skewness $|SXY/R^2|$

7. Asymmetry $((SXY)^2-SX^2SY^2)/R^4$

8. SDEV $\sqrt{V}$

9. Gray level difference $SIG/(N-P) - SPG/P$ } brightness

10. E_p SPE/P

where:

Symbol	Meaning
1. N	Area
2-3. SX, SY	$\Sigma X, \Sigma Y$ - first moments
4-6. SX^2, SY^2, SXY	$\Sigma X^2, \Sigma Y^2, \Sigma XY$ - second moments
7. P	Perimeter point count
8. E	High edge point count
9. SPE	Total edge value on the perimeter
10. SIG	Total interior gray value
11. SPG	Total perimeter gray value
12-13. SG, SG^2	Total gray level, total squared gray level

and

1. X_{AVE} $4*\sqrt{SX^2}$

2. Y_{AVE} $4*\sqrt{SY^2}$

3. R^2 $SX^2 + SY^2$

4. V $SG^2/N - (SG)^2/N^2$

Table 3-4. Target Source Data Sets

Data Set	Jeeps	APC's	Tanks
Alabama	5	9	8
Fort Polk 1	0	1	6
Fort Polk 2	0	2	0
Hunter Liggett 1 & 2	0	1	0

shown by a column, headed by a single letter where J = Jeeps, A = APC's, T = Tanks, N = Noise, and P = Probable Target, Type Unknown. In addition to presenting the Fourier features, the table also shows area of each target's binary silhouette, along with the gray-scale threshold used to create the silhouette.

Table 3-6 presents the raw feature measurements obtained for the same sample images from each of the 10 University of Maryland features listed in Table 3-3. Since the same silhouettes were used (both Fourier and University of Maryland Feature sets) the area and threshold values are the same.

3.3.3 Measuring Cost and Performance

For any combination of feature candidates, (1) the cost necessary to achieve any desired level of classification performance (including 100 percent), and (2) expected classifier performance in terms of Probability of Recognition (PR) and False-Alarm Rate (FAR) is measured.

3.3.3.1 Classifier Cost - The concept of classifier cost is defined inductively at first, and later defined precisely.

Consider Figure 3-34. These are scatterplots of known target images in three feature dimensions. In Figure 3-34A, three target classes are each represented by one point and each class is separated in feature space. It is obvious that there exists a large number of possible ways to summarize these classes, and a large number of different classification rules. However, each classifier must have the same nil cost, since it is necessary to account for three different points in feature space and exactly three classes.

Table 3-5. Fourier Features

NUM	IMAGE	CLASS J	A	T	N	F	TD 1	TD 2	TD 3	TD 4	LD 5	AREA	THRESH
1	38	-	-	X	-	-	2244.0	181.0	97.0	203.0	3.2	239.0	203.0
2	42	-	-	X	-	-	1412.0	94.0	34.0	62.0	1.9	341.0	195.0
3	44	-	-	X	-	-	2439.0	186.0	114.0	310.0	3.2	280.0	199.0
4	55	-	X	-	-	-	2946.0	234.0	155.0	428.0	3.9	180.0	190.0
5	57	-	-	X	-	-	1612.0	96.0	42.0	100.0	1.9	417.0	177.0
6	58	-	X	-	-	-	1682.0	120.0	39.0	69.0	2.3	387.0	177.0
7	134	-	-	X	-	-	3319.0	267.0	281.0	865.0	4.4	110.0	190.0
8	135	-	X	-	-	-	2710.0	166.0	162.0	508.0	2.9	176.0	81.0
9	136	X	-	-	-	-	4436.0	380.0	588.0	2274.0	6.1	71.0	43.0
10	140	-	X	-	-	-	6130.0	790.0	1387.0	4553.0	12.1	28.0	127.0
11	141	-	X	-	-	-	2425.0	131.0	115.0	387.0	2.4	281.0	77.0
12	150	-	X	-	-	-	5124.0	568.0	830.0	2696.0	8.8	48.0	126.0
13	159	X	-	-	-	-	5214.0	537.0	967.0	3716.0	8.4	42.0	57.0
14	165	-	X	-	-	-	2890.0	188.0	189.0	686.0	3.3	206.0	177.0
15	172	-	-	X	-	-	1401.0	71.0	34.0	73.0	1.5	336.0	100.0
16	173	X	-	-	-	-	4472.0	463.0	547.0	1653.0	7.3	66.0	109.0
17	178	-	X	-	-	-	4439.0	402.0	624.0	2308.0	6.4	61.0	75.0
18	179	-	X	-	-	-	3256.0	219.0	235.0	780.0	3.7	144.0	151.0
19	180	-	X	-	-	-	2670.0	138.0	129.0	511.0	2.5	315.0	97.0
20	182	-	X	-	-	-	2296.0	139.0	102.0	293.0	2.5	250.0	100.0
21	183	-	X	-	-	-	2575.0	166.0	150.0	434.0	3.0	163.0	104.0
22	184	X	-	-	-	-	4113.0	340.0	478.0	1693.0	5.5	73.0	65.0
23	193	-	X	-	-	-	4411.0	475.0	634.0	2132.0	7.5	62.0	152.0
24	197	-	X	-	-	-	3483.0	301.0	350.0	1155.0	4.9	95.0	208.0
25	198	-	X	-	-	-	3373.0	224.0	253.0	918.0	3.8	155.0	149.0
26	200	-	X	-	-	-	2478.0	145.0	121.0	420.0	2.6	297.0	202.0
27	201	-	X	-	-	-	2284.0	133.0	103.0	304.0	2.5	253.0	168.0
28	202	X	-	-	-	-	3469.0	266.0	317.0	1141.0	4.4	124.0	125.0
29	226	-	X	-	-	-	7699.0	1297.0	2709.0	8476.0	19.5	15.0	112.0
30	295	-	X	-	-	-	2627.0	200.0	114.0	290.0	3.4	279.0	195.0
31	403	-	X	-	-	-	3698.0	307.0	289.0	817.0	5.0	113.0	201.0
32	410	-	X	-	-	-	3378.0	272.0	239.0	706.0	4.5	146.0	192.0

Table 3-6. Maryland Features

NUM	IMAGE	CLASS J	A	T	N	F	TD 1	TD 2	TD 3	TD 4	TD 5	TD 6	TD 7	TD 8	TD 9	TD 10
1	38	-	-	X	-	-	1.1	0.1	2.2	0.3	-0.1	0.0	-0.2	11.9	-4.8	255.1
2	42	-	-	X	-	-	1.3	0.0	1.8	0.3	-0.3	0.1	-0.2	15.5	-337.9	216.7
3	44	-	-	X	-	-	1.2	0.0	1.9	0.3	-0.2	0.1	-0.2	14.4	3.6	207.5
4	55	-	X	-	-	-	1.8	0.3	1.7	0.3	-0.5	0.0	-0.2	15.2	5.9	228.3
5	57	-	-	X	-	-	1.2	0.1	1.6	0.3	-0.2	0.1	-0.2	19.1	-242.0	216.1
6	58	-	-	X	-	-	1.1	0.1	2.2	0.2	-0.1	0.0	-0.2	12.8	247.2	124.5
7	134	-	-	X	-	-	1.5	0.2	1.6	0.6	-0.4	0.2	-0.2	20.8	26.2	305.9
8	135	-	X	-	-	-	1.5	0.2	1.3	0.6	-0.4	0.0	-0.2	39.1	59.1	525.3
9	136	X	-	-	-	-	0.9	0.3	1.3	0.6	0.1	0.1	-0.2	55.6	86.0	499.7
10	140	-	X	-	-	-	0.8	0.4	14.8	2.5	0.1	0.4	-0.2	13.6	-9.3	235.2
11	141	-	-	X	-	-	1.5	0.2	1.3	0.6	-0.4	-0.1	-0.2	50.6	-225.3	346.1
12	150	X	-	-	-	-	0.9	0.3	6.2	1.2	0.1	0.4	-0.1	33.7	27.8	422.6
13	159	X	-	-	-	-	1.0	0.2	1.3	0.6	0.0	0.0	-0.2	65.5	88.6	539.7
14	165	-	-	X	-	-	1.4	0.1	1.3	0.5	-0.3	0.0	-0.2	20.9	-419.5	516.5
15	172	-	-	X	-	-	1.9	0.4	1.3	0.5	-0.6	0.1	-0.2	56.8	-185.6	345.3
16	173	-	X	-	-	-	1.9	0.4	1.7	0.4	-0.6	0.0	-0.2	7.4	4.1	110.5
17	178	X	-	-	-	-	1.0	0.2	1.3	0.6	0.0	0.0	-0.2	42.0	62.5	441.7
18	179	-	X	-	-	-	1.7	0.3	1.4	0.5	-0.5	0.0	-0.2	14.5	9.3	303.3
19	180	-	-	X	-	-	1.9	0.4	1.4	0.6	-0.6	0.1	-0.2	47.2	-192.5	432.5
20	182	-	-	X	-	-	1.5	0.2	1.5	0.5	-0.4	0.1	-0.2	41.2	-315.9	366.5
21	183	-	-	X	-	-	1.6	0.2	1.3	0.6	-0.4	0.0	-0.2	23.2	18.7	419.9
22	184	X	-	-	-	-	0.9	0.3	1.3	0.6	0.1	0.0	-0.2	51.9	75.0	483.9
23	193	-	X	-	-	-	1.1	0.1	3.1	0.8	-0.1	0.2	-0.2	27.2	25.5	244.2
24	197	-	X	-	-	-	1.1	0.1	1.4	0.5	-0.1	0.0	-0.2	13.8	16.2	310.2
25	198	-	X	-	-	-	1.6	0.2	1.4	0.5	-0.4	0.0	-0.2	14.1	16.6	216.1
26	200	-	-	X	-	-	1.5	0.2	1.5	0.5	-0.4	0.0	-0.2	16.8	-270.4	280.4
27	201	X	-	-	-	-	1.2	0.0	1.4	0.6	-0.2	0.1	-0.2	29.7	-298.7	335.1
28	202	-	X	-	-	-	0.9	0.3	2.0	0.8	0.1	0.2	-0.2	41.6	59.6	417.7
29	226	-	X	-	-	-	0.7	0.6	40.3	4.2	0.4	0.4	0.0	14.7	-50.0	253.5
30	295	-	-	X	-	-	1.4	0.1	2.4	0.3	-0.3	0.1	-0.2	16.2	379.6	-171.3
31	403	-	X	-	-	-	2.3	0.6	1.8	0.4	-0.7	-0.1	-0.1	11.1	10.3	267.0
32	410	-	X	-	-	-	2.3	0.5	1.7	0.4	-0.7	0.0	-0.1	15.8	16.3	260.8

24-JUN-79 19:35:27

3-41
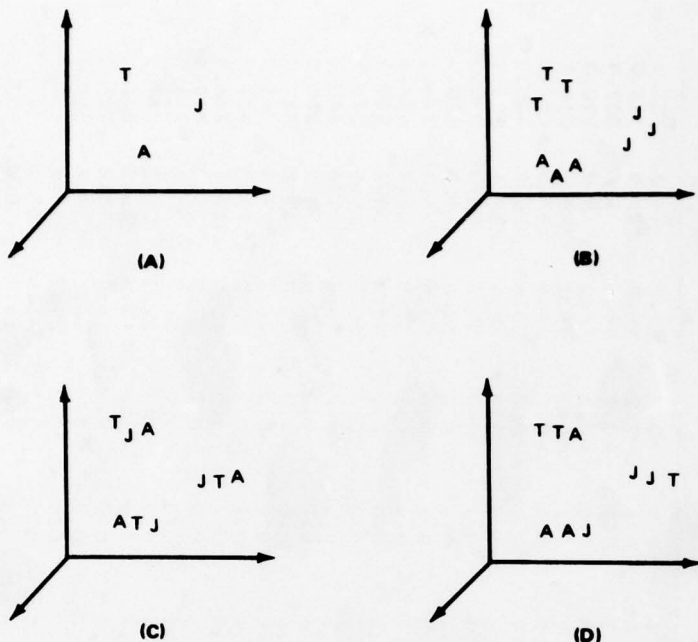
Figure 3-34. Scatterplots of Target Images in 3-D Feature Space
(T = Tank, A = APC, J = Jeep)

Like Figure 3-34A, Figure 3-34B illustrates three target classes, but
there are nine individual points distributed in feature space. To
measure classifier cost, it is necessary to be able to summarize the
distribution of feature vectors within each class. It is obvious
using any practical concept of distance, that when inspected, all
members of each class in this scatterplot occupy about the same re-
gion of feature space. Members of each class, therefore, 'cluster'
well. More precisely, the distance between any two points belonging
to the same class is less than the distance between any one of these
points and any other point of any other class (where distance is some
additive function of real measurements on features). As it turns out,
therefore, the cost of classifying targets based on Figure 3-34B is
also nil.

3-42

Likewise, Figure 3-34C shows three target classes with nine target points. It is obvious, by inspection, that there exists no practical distance metric on features which can yield a summary of the targets in feature space with a nil cost of classification. We might, for example, assign each target image to its own cluster. Since the actual and maximum possible number of clusters are both nine, the cost of classification is maximal, or 9/9 = 1.0. Figure 3-34C therefore summarizes a scatterplot of target feature vectors, in feature space, for which the most obvious classification rule is also the most expensive one possible.

In general, we shall define the cost of a classifier, given a distribution of training target feature vectors in feature space, as

$$COST = (ANC - CL) / (N - CL)$$

where ANC is some actual number of clusters ($1 \leq ANC \leq N$), CL is the number of different target classes ($1 \leq CL \leq N$), and N is the total number of target feature vectors.

3.3.3.2 <u>Classifier Performance</u> - We can then measure expected classifier performance of a given cost by empirical estimates of PR and FAR for any given class of target $\underline{t}$: .

$$PR = \sum_{i=1}^{ANC} (t_i \mid t_i)/t_f$$

$$FAR = \sum_{i=1}^{ANC} (t_i \mid \overline{t}_i)/t_f$$

where t_f is the true frequency of target class $\underline{t}$.

In Table 3-7, we show performance and cost measures obtained from each of the four scatterplots of Figure 3-34. For Figure 3-34D we have held the cost to a minimum, and map clusters by a simple majority vote.

3-43

Table 3-7. Cost and Performance Measures of the Features Shown in Figure 3-34.

Figure	Cost	Performance	
		PR	FAR
3-34A	0.0	1.0	0.0
3-34B	0.0	1.0	0.0
3-34C	1.0	1.0	0.0
3-34D	0.0	0.6	0.3

3.3.3.3 An Example - Figure 3-35 shows a scatterplot of feature points obtained for Maryland features TD1 (abscissa) and TD6 (ordinate). These features are described in more detail in paragraph 3.3.3.1 of this report.

Each letter represents a different target class, with T = tank, A = APC, and J - jeep.

Figure 3-36 shows the same scatterplot marked with significant clusters outlined by dashed or by solid lines, and labeled for ease of presentation. The automated classifications for which Figure 3-36 is a summary are shown in Figure 3-37.

For this example, we have measured classifier cost = 0.091 in return for an overall PR = 0.714. The PR for tanks = 1.00 in return for an overall FAR = 0.289.

Figures 3-38 and 3-39 illustrate exactly the same scatterplots using a cluster rule designed to improve overall performance. In this case, we have measured classifier cost = 0.568 in return for an overall PR = 0.821. Thus, the classifications obtained in the first instance were 48 absolute percent less expensive and sacrificed only 11 percent in global PR.

3.3.4 Summary of Findings

The target classifier described in the appendix of this report can achieve 100 percent correct a posteriori classifications of targets (PR = 1.00, FAR = 0.00) given only that a feature set produces a unique feature vector for each training image. The performance of

3-44
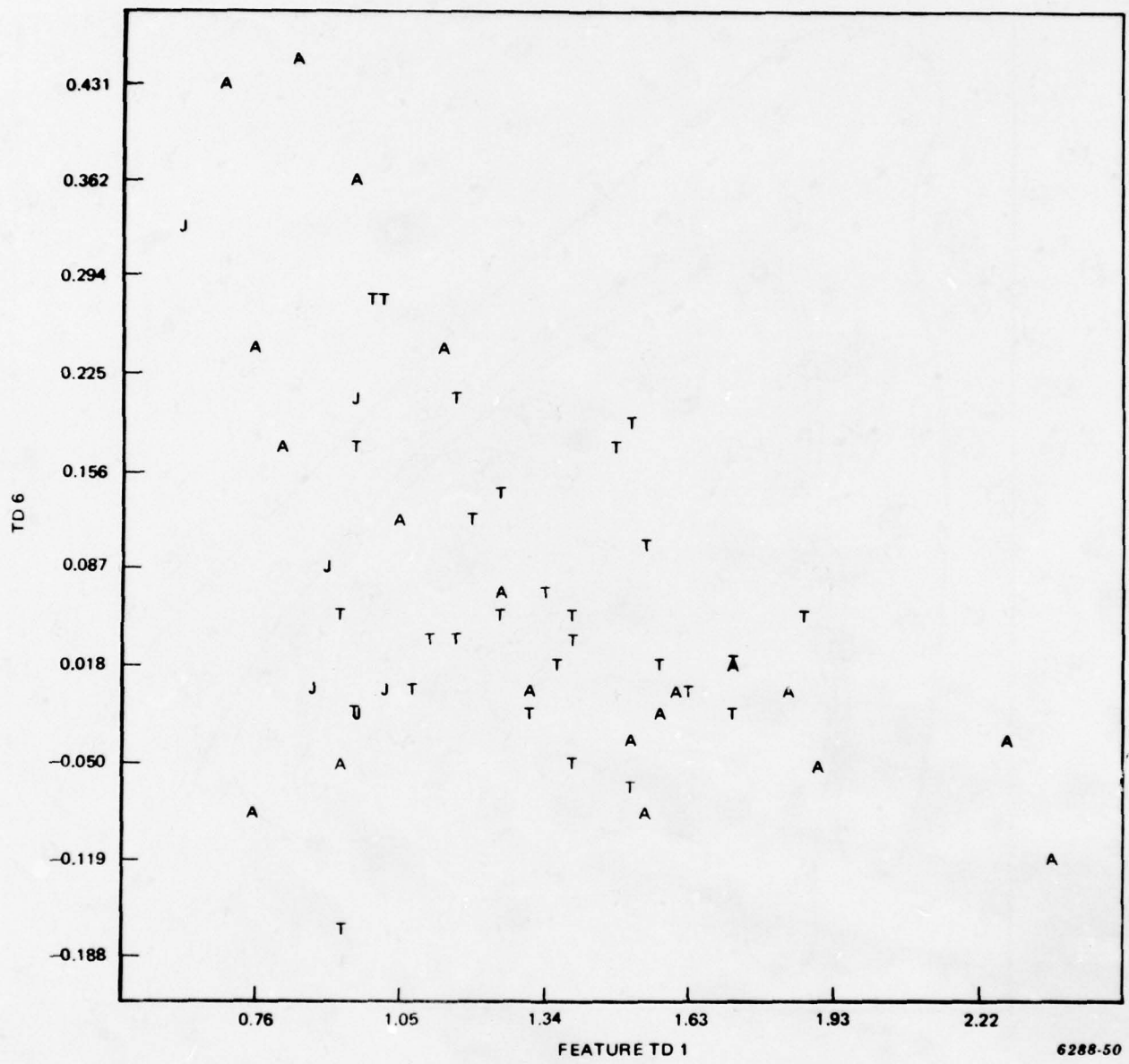
Figure 3-35. Scatterplot of 56 IR Target Images Based on the
University of Maryland's TD1 - TD6 Features

6288-50
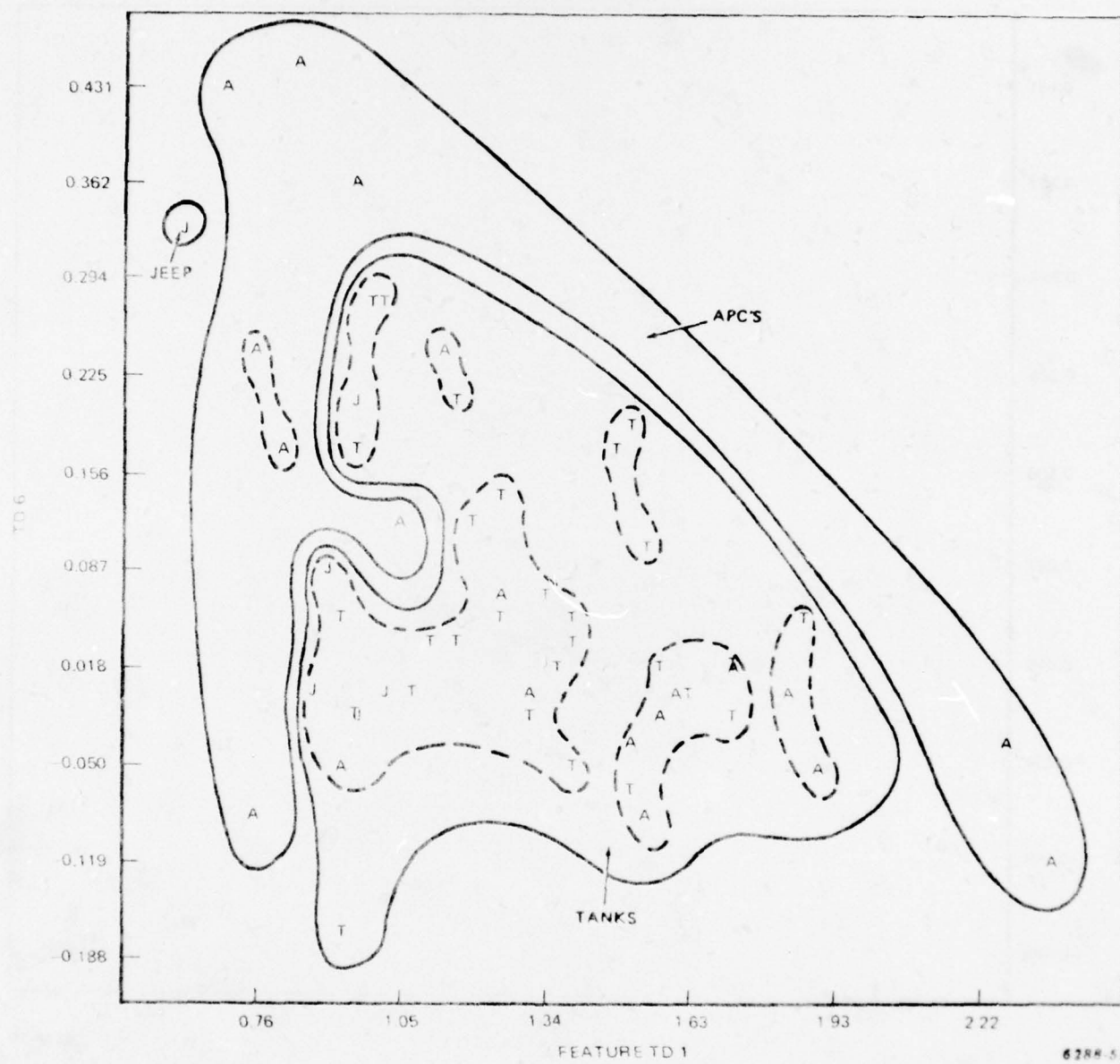
Figure 3-36. Significant Target Clusters by Class
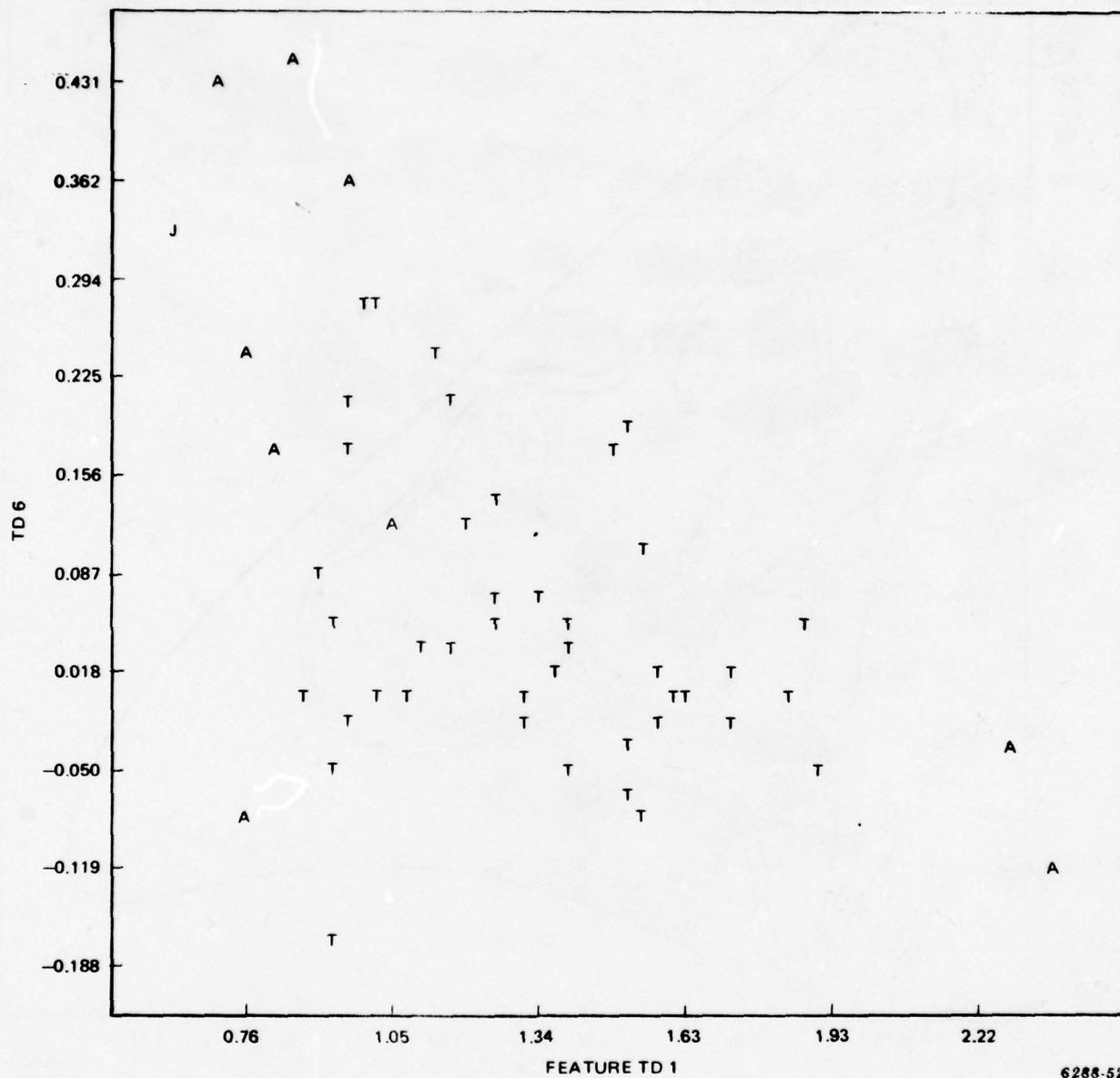
Figure 3-37. Feature TD1
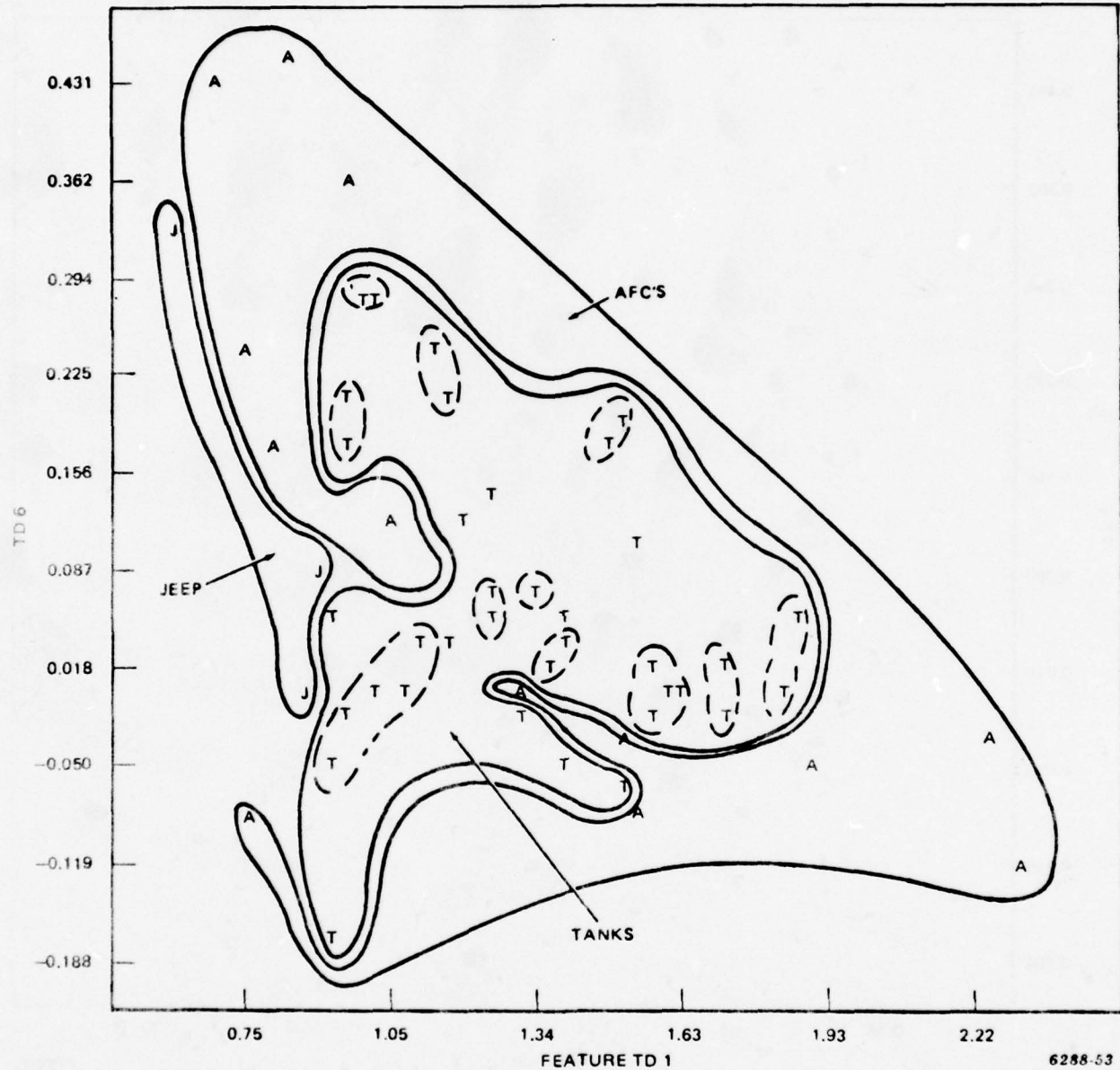
Figure 3-38. Significant Target Clusters by Class
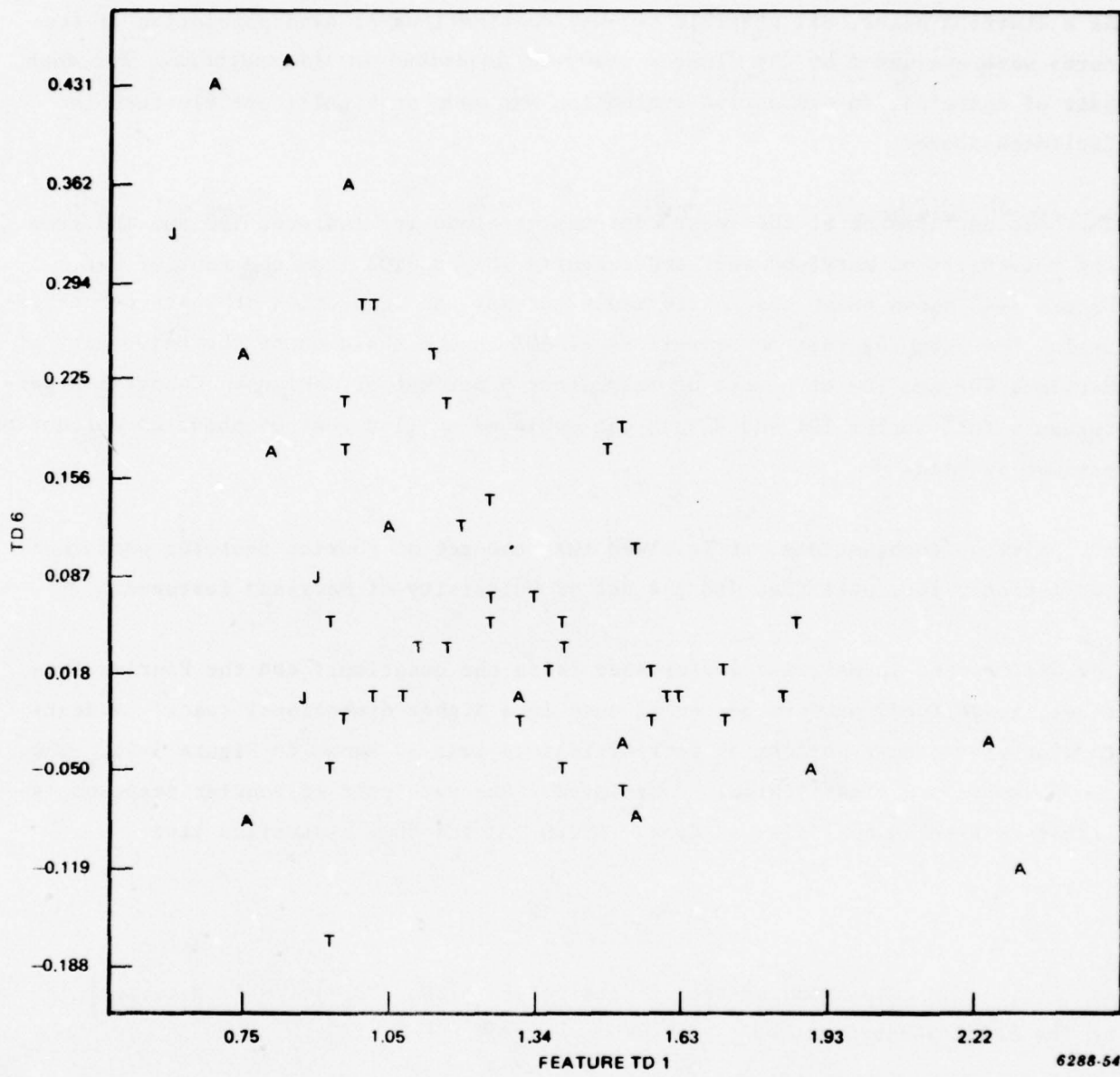
Figure 3-39. Automated Classification (Cost = 56.8%; PR = 82.1%)

6288-54

target feature sets may be compared in terms of their respective classifier costs for a given level of accuracy, or in terms of their accuracy for a given cost.

As a starting point, all possible two-way combinations of each population of features were evaluated by the cluster analyzer described in the appendix. For each pair of features, an exhaustive evaluation was made of significant clusters in Euclidian space.

The best performance at the least cost was obtained for features TD8 and TD9 from the University of Maryland set, and features TD1 and TD5 from the Fourier set. Figure 3-40 shows these cost/performance curves. An inspection of these curves reveals, for example, that an overall PR of 80% can be achieved by the University of Maryland TD8 and TD9 at a cost of only about 9 percent of maximum. Comparable performance for Fourier TD1 and TD5 is not achieved until a cost of about 25 percent of maximum is paid.

For pairwise combinations, it is clear that the set of Fourier features performed consistently less well than did the set of University of Maryland features.

The differences in pairwise performance raise the question: can the Fourier features, as defined, perform better if used in a higher dimensional space? A scatterplot of the best performing Fourier feature pair is shown in Figure 3-41. The two features are clearly highly correlated. For each pair of Fourier features, a linear regression analysis was done. Given TD_x and TD_y, a straight line

$$TD_y = a_o + a_1 TD_x$$

was fit to the corresponding set of data points $\left\{ (TD_{x_i}, TD_{y_i}), i = 1, 2, \ldots, n \right\}$ by the least squares method.

The coefficient of determination r^2 is the proportion of total variation about the mean $\overline{TD}_y$ explained by the regression, or the goodness of fit of the regression line.
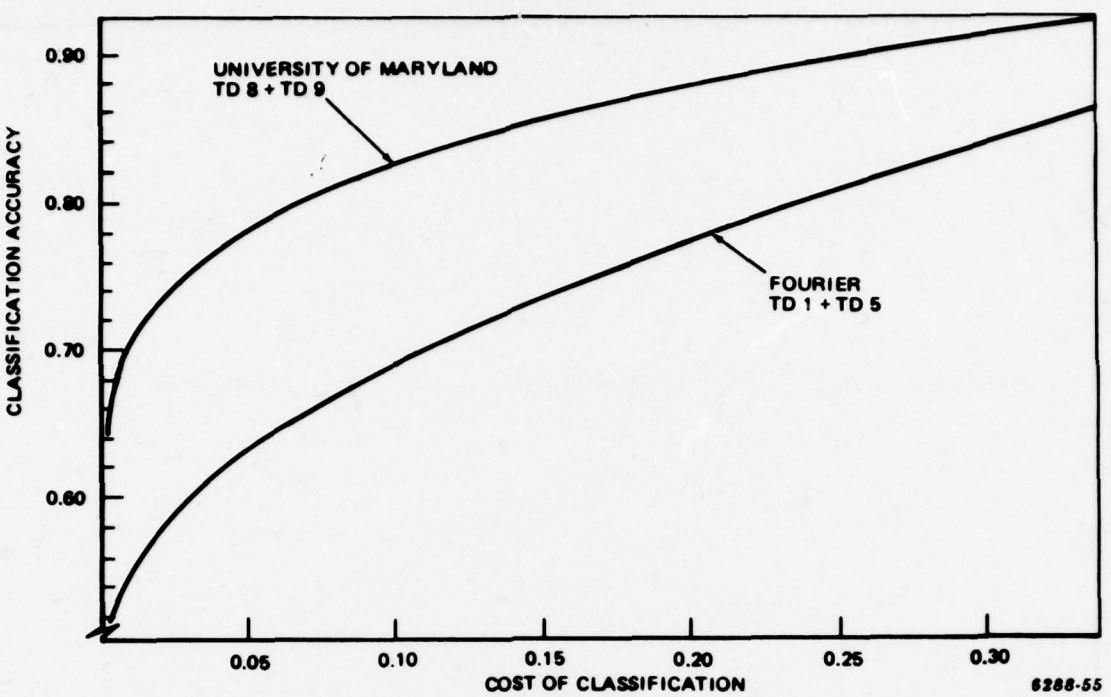
Figure 3-40. Performance Comparison Scale for the University of Maryland
TD8 and TD9 and Fourier TD1 and TD5

$$
r^2 = \frac{\left[\displaystyle\sum_{i=1}^{n} TD_{x_i} TD_{y_i} - \frac{\sum TD_{x_i} \sum TD_{y_i}}{n} \right]^2}{\left[\displaystyle\sum_{i=1}^{n} TD_{x_i}^2 - \frac{\left(\sum TD_{x_i}\right)^2}{n} \right]\left[\displaystyle\sum_{i=1}^{n} TD_{y_i}^2 - \frac{\left(\sum TD_{y_i}\right)^2}{n} \right]} \tag{3-2}
$$

r^2 was found to range from 0.8 to 1.0 for the Fourier feature pair set. Thus, any
higher order linear combination of features beyond two would not increase per-
formance. Indeed, for purposes of discriminating between different classes of target
the Fourier feature set is essentially a single dimension (Figures 3-41 and 3-42).
We, therefore, conclude that for the Fourier feature set the curve shown in Figure
3-40 is nearly asymptotic.

3-51
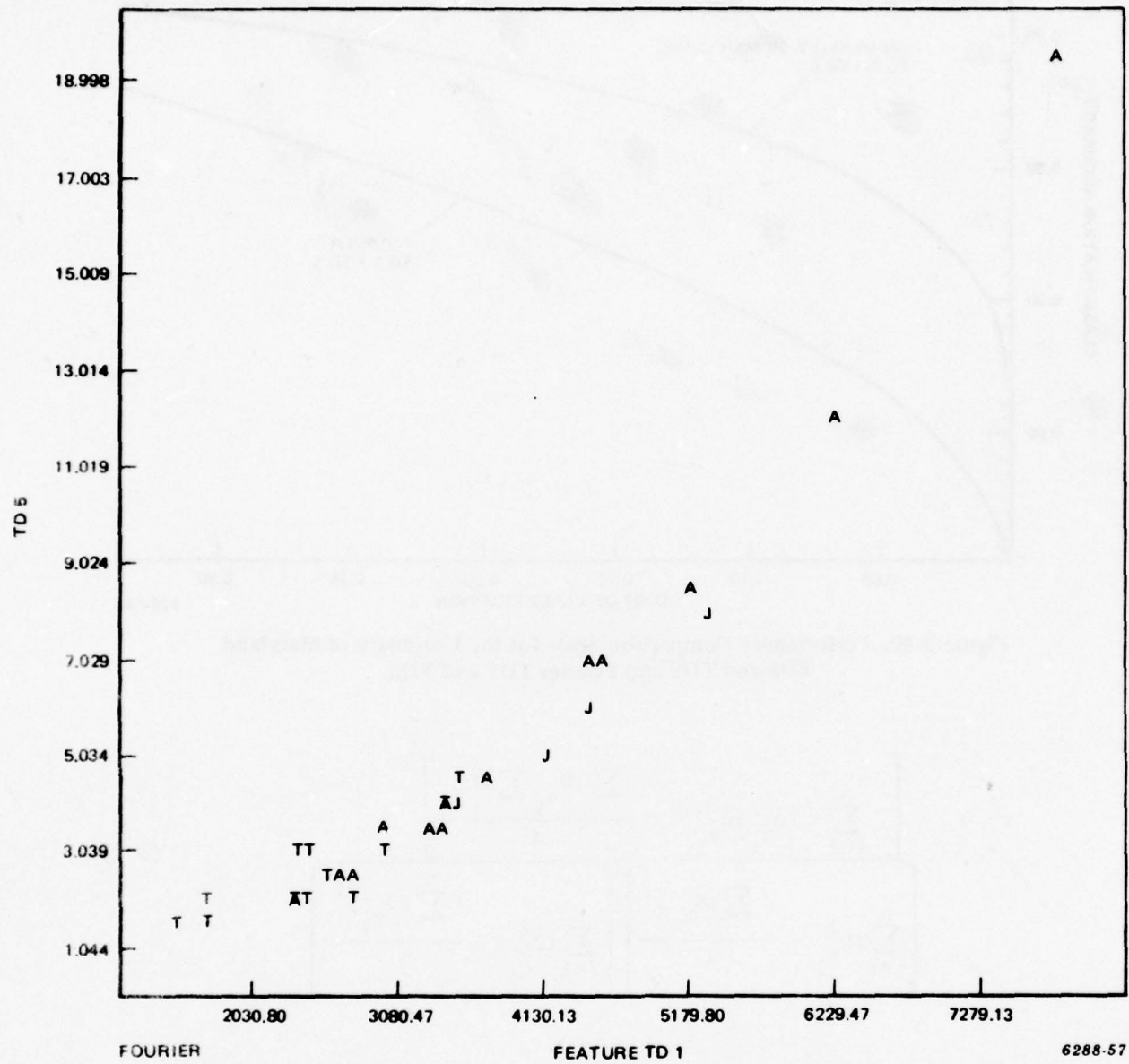
Figure 3-41. Scatterplot of Fourier Features

In further studies during the next quarter, an optimal combination of features from the Maryland set will be found. Efforts are also under way to define a set of features in the Fourier transform domain that do not display such a high degree of inter-correlation. The resultant new Fourier features will then be compared with the optimal University of Maryland feature combination.
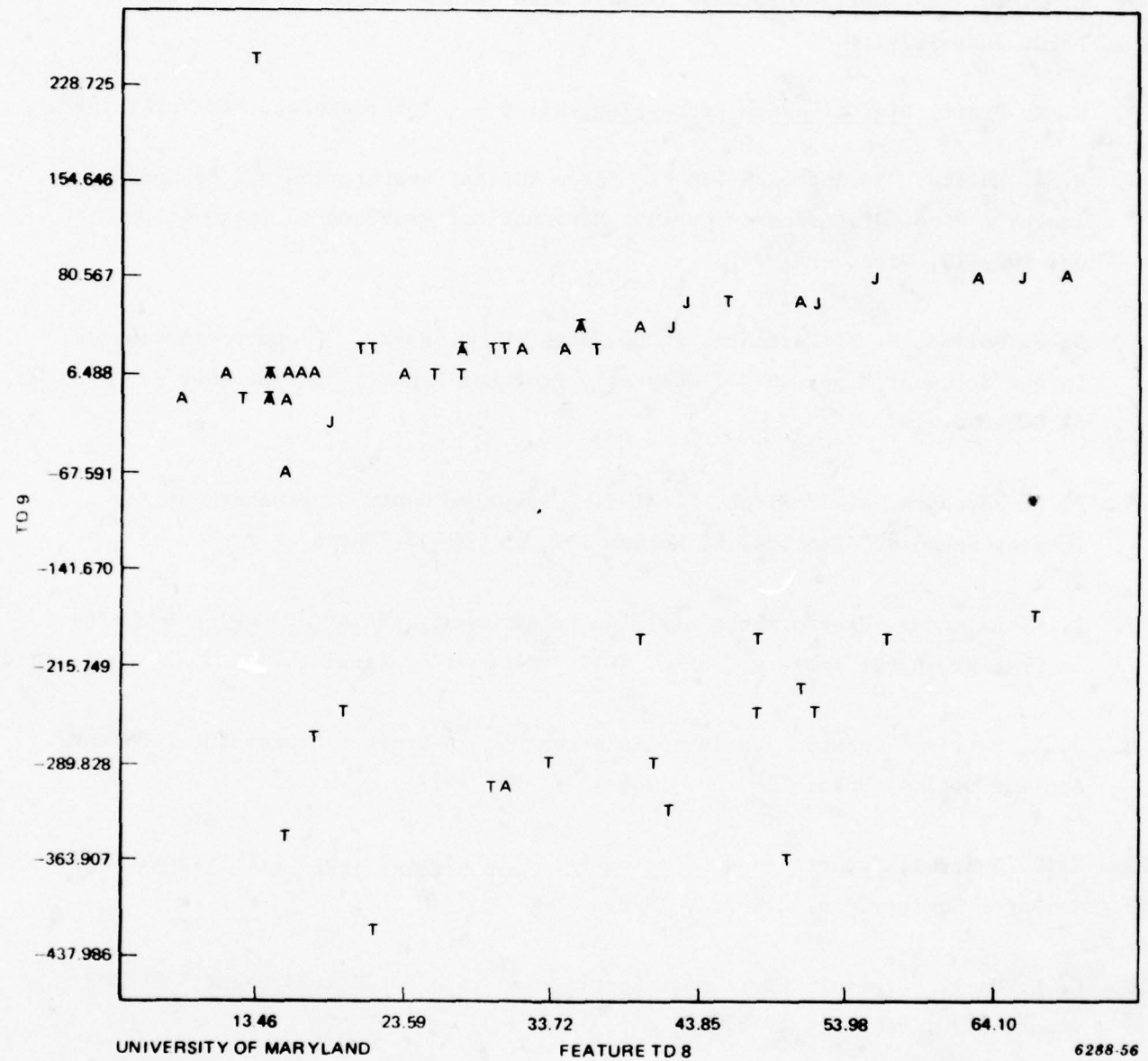
Figure 3-42. Scatterplot of University of Maryland Features

3.4 REFERENCED DOCUMENTS

1. A.A. Schwartz, J. M. Soha, "Variable Threshold Zonal Filtering," Applied Optics, Vol. 16, pp. 1779-1781, July 1977.

2. C. M. Lo, "Estimation of Image Signals with Poisson Noise," USC IPI Report #890, June 1979.

3. W. K. Pratt, Digital Image Processing, Wiley - - Interscience, New York, 1978.

4. R. H. Wallis, "An Approach for the Space Variant Restoration and Enhancement Images", Proc. Symposium on Current Mathematical Problems in Image Science, pp. 107-110, November 1976.

5. D. E. Soland, P. M. Narendra, R. C. Fitch, D. P. Panda, "Prototype Automatic Target Screener," pp. 26-47, Quarterly Progress Report, 21 September - 31 December 1977.

6. P. M. Narendra, R. C. Fitch, "Real-Time Adaptive Contrast Enhancement for Imaging Sensors," Proc. SPIE, Volume 137, pp. 31-35, March 1978.

7. P. K. Raimondi, "Performance of Image Enhancement and Target Cueing Techniques on Grafenwoehy II Imagery," Proc. SPIE, Volume 178, April 1979.

8. J. L. Harris, "Constant Variance Enhancement: A Digital Processing Technique," Applied Optics, Volume 16, pp. 1268-1271, May 1977.

9. H. C. Andrews, Tutorial and Selected Paper in Digital Image Processing, IEEE Computer Society, pp. 274-332, 1978.

10. C. F. Hall, "Digital Color Image Compression in a Perceptual Space," USCIPI Report #790, February 1978.

11. David L. Milgram and Azriel Rosenfeld, Algorithms and Hardware Technology for Image Recognition, Final Report to U.S. Army Night Vision Lab. March 31, 1978 (Contract DAAG53-76C-0138).

12. H. B. Henning and G. A. Guzman, Automatic Contrast Brightness Control, 11 October 1979, Northrop #Y4310-79/ASA-074.

SECTION 4
EQUIPMENT DESIGN

The equipment comprising the Automatic Target Cuer (ATC) and its interface with the Common Module Forward Looking Infrared (FLIR) consists of the FLIR Digitizer and scanner mirror Position Quantizer, and the Target Cuer Processing Elements. The following paragraphs describe the requirements dictating the design parameters for the equipment design, a description of the present design, and a brief summary of the current design status.

4.1 FLIR DIGITIZER

The FLIR Digitizer consists of that hardware necessary to convert analog video signals from the LOHTADS Common Module FLIR to a form suitable for use by the ATC. The following paragraphs describe the requirements for interfacing the FLIR Digitizer to the Common Module FLIR, the detail design of the FLIR Digitizer, and the current status of the design.

4.1.1 Common Module FLIR Interface

A review of the Common Module FLIR System sets forth the interface requirements for the FLIR Digitizer. The optical concept of the Common Module FLIR is depicted in Figure 4-1. A thermal image is optically projected to the image plane. This thermal image is swept across a line array of Infrared (IR) detectors by the oscillating scanner mirror. The electrical signals thus produced are amplified and used to drive a line array of light-emitting diodes, producing modulated light in the visible spectrum. This is projected onto the back side of the scanning mirror, and through the exit optics to produce a visible image. Interlace is achieved by slightly offsetting the scanning mirror about the scan-orthogonal axis during the retrace. The electronics block diagram of a Common Module FLIR System is depicted in Figure 4-2. In the LOHTADS system, however, the second stage of the post-amplifier/driver is replaced with the Sen-Te-Chow automatic low-frequency gain limiting (AFLGL) circuit, which reduces the video dynamic range from about 70 decibels (dB) to about 25 dB, greatly easing the video dynamic range problem. The output of the postamplifier/driver is used as the source of video signals for the FLIR Digitizer. The following characteristics of the Common Module FLIR are particularly pertinent to the design of the ATC and, specifically, the FLIR digitizer:
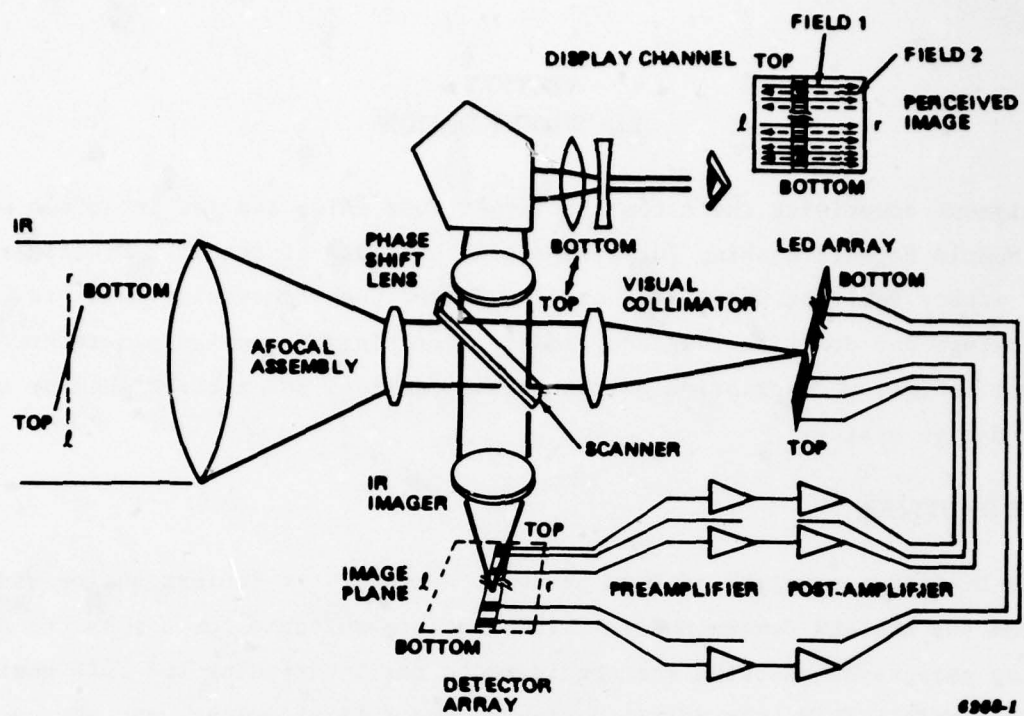
Figure 4-1. FLIR Optical Concepts

a. The video format is line-parallel with interlace in a direction opposite to the forward scan direction, whereas the video display which the ATC will ultimately drive, expects video formatted line-serial with interlace in the same direction as the forward scan.

b. Registration between the IR and visible images is almost perfect because both utilize nearly identical mirror scanning planes. When the video is taken prior to the output scan, however, the scan mirror position must be sensed with sufficient accuracy to allow later point-to-point and frame-to-frame registration in the displayed image.

Both of the above imply that the FLIR Digitizer cannot be a free-running design. Item b further implies that there must be an accurate determination of mirror position throughout the digitization cycle. The interface to the Common Module FLIR, then, requires one video signal line for each of the detector elements in the line array (i.e., the output of each of the postamplifier/drivers) and one signal accurately indicating the scanner mirror angular position.

4-2
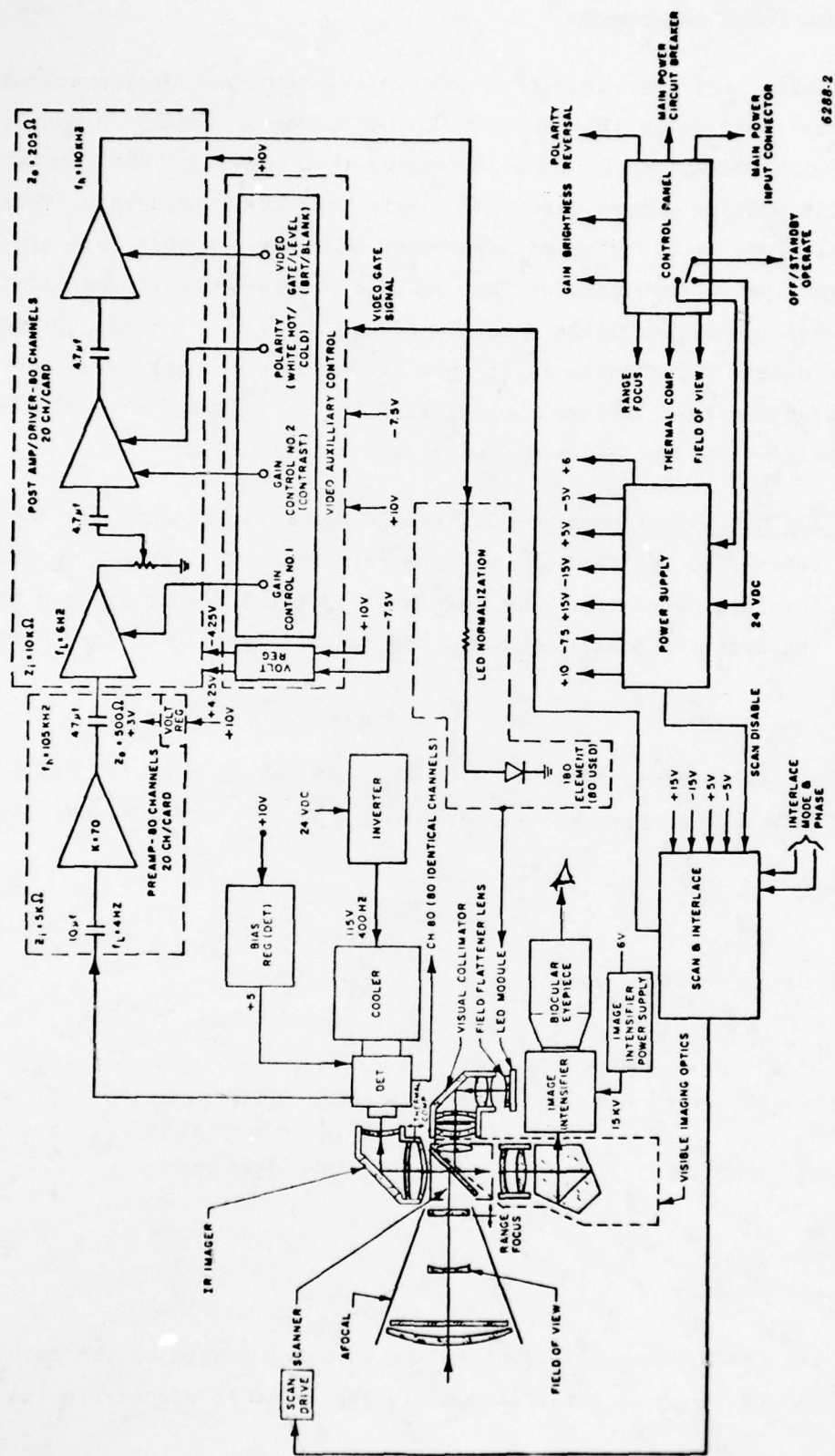
Figure 4-2. Typical Common Module System Functional Block Diagram

4.1.2 FLIR Digitizer Design Requirements

The numerical values for the parameters used in the digitizer design calculations and shown herein are those for a 160-detector Common Module system and a scan rate of 60 hertz. The actual LOHTADS application, however, utilizes only 120 detectors, and at the time of this writing a scan rate of 30 hertz is being considered. Thus, the design presented here involves speed parameters that are somewhat more severe than required for the LOHTADS application, but it also provides growth potential for other applications while still providing adequate design margins. For the LOHTADS application, the excess video channels are not included in the implementation. The excess spatial sampling rate is left alone, resulting in somewhat over sampling for the LOHTADS application, but eases aliasing considerations.

4.1.2.1 <u>Sampling Rate Requirements</u> - The sample rate requirements for the FLIR Digitizer are determined by finding a minimum rate which will have a negligible effect on the combined Modulation Transfer Function (MTF) resulting from the IR optical design, the detector size and shape, and the electronics temporal frequency response.

For a system that is detector limited, with an image aspect ratio of 4:3 and a 2:1 interlace the number of samples per video line may be determined by the following:

Let:

    W = actual detector size (detector is square)

    w = effective detector width w = .75 W

    H = image height at the detector plane

    L = image length, after masking, at the detector plane

If the image aspect ratio is to be 4:3 as in LOHTADS, then:

$$\frac{L}{H} = \frac{4}{3} \tag{1}$$

The vertical size of the image is equal to the physical length of the detector array, with a 2:1 interlace, each detector element in the array is spaced W units from its

neighbor (i.e., the elements are on 2 W centers). The physical vertical dimension of the image for a 160-detector array is:

$$H = 160(2W) \qquad (2)$$

Substituting (2) into (1) produces:

$$\frac{L}{160(2W)} = \frac{4}{3}$$

$$L = \frac{4(160)(2W)}{3} = 427\ W \qquad (3)$$

The effective detector width however is somewhat less than the physical width for this detector:

$$w = 0.75W \quad \text{or} \quad W = \frac{w}{0.75} \qquad (4)$$

Substituting (4) into (3) produces:

$$L = 427\ W = (427)\ \frac{w}{0.75} = 569\ w \qquad (5)$$

For a detector-limited system, the limit in horizontal resolution is reached when the image component at the detector array is equal to the detector effective width. Then the resolution limit is the total image length divided by the effective detector width from (5):

$$L = 569w \quad \text{or} \quad \frac{L}{w} = 569.$$

Nyquist criteria require at least two samples per minimum image component, therefore, the minimum number of samples per line is 1138.

Thus, the required number of samples is 1138 on each detector video signal for each field. Additionally, the Target Cuer algorithms are simplified if the number of samples per line is an integral multiple of the number of lines per frame. The lowest multiple higher than the required number is 4(320) or 1280 samples per line. By the same reasoning, for LOHTADS, with only 120 detectors, the number is 960 samples per line.

4-5

The scanner mirror completes a cycle (i.e., one forward scan and one retrace) in 1/60th of a second, or each direction in 1/120th of a second; however, because the mirror is oscillating, there are some mechanical turnaround transients, and only 65 percent of the scan time is usable. Scan time, then is 65 percent of 1/120th second, or 5.42 milliseconds. Sampling at 1280 samples per scan line results in a sample time of 5.42/1280 milliseconds, or 4.23 μseconds, which gives a sample rate of 236,308 samples per second.

4.1.2.2 <u>Scan Mirror Position Sensing Requirements</u> - In its normal mode of operation, the Common Module FLIR effectively removes scanner mirror motion anomalies by scanning the visible image with the back side of the same mirror that scans the thermal image. The FLIR Digitizer, however, will take the video signals from the postamplifier prior to forming the visible image. For this application, then, scan mirror position must be measured accurately.

Good picture quality is obtained if the spatial error for a given pixel is better than about 1/4 of a pixel. With 1280 samples per line, then, the allowable pixel position error is 1/4 (1/1280) or approximately 0.02 percent of the image width, for any pixel position relative to a reference grid. However, for visual viewing of a single frame, where a single frame is captured and continuously displayed, a considerable amount of elongation or nonlinearity can be tolerated without objection. (Typical nonlinearity factors for commercial TV are 10 percent.) The only requirement is that each pixel fall within 0.02 percent of image width relative to its companion pixel on adjacent lines. In other words, scale factor and linearity, in the absolute sense, can be considerably in error without objection provided that the anomalies are the same for both the forward and the retrace scan of the mirror. However, when integration of multiple frames occurs, such as eye integration of a visual display or integration to improve signal-to-noise ratio, repeatability over the integration period to within 0.02 percent must be maintained; otherwise, excessive blurring will occur.

In summary, repeatability to within 0.02 percent over 0.5 seconds is a firm requirement. Linearity and scale factor accuracy to within 0.02 percent will be a design goal for possible future applications, but not a firm requirement for this system.

4.1.2.3 Interface Buffer/Filter - The interface point for the video signals is at the output of the FLIR postamplifier/drivers. These drivers, however, are basically operated as current drivers in the FLIR normal mode of operation to drive the LED line array. When coupled to the FLIR Digitizer, the drivers must function in voltage mode. An interface buffer is required to perform bias and gain compensation on each detector channel. The buffer also provides the capability for an anti-aliasing filter.

Anti aliasing filters will be implemented in the Model 1 ATC, however, since noise in the amplifier circuits may be a problem. The requirements for filtering will be determined during Model 1 test.

4.1.3 FLIR Digitizer Design

Figure 4-3 is a block diagram of the ATC system showing the relationship of the FLIR Digitizer to the Common Module FLIR and the remainder of the Target Cuer System. Video from the postamplifier/drivers feeds the interface amplifiers and filters. The interface amplifiers provide gain and offset adjustment, high frequency roll-off, and interface buffering between the postamplifier/drivers and the multiplexer. The video signals are then fed through four groups of 32-channel, three-stage, analog multiplexers which output four Time-Division-Multiplexed (TDM) video signals. Each of the four TDM video signals is fed to an Analog-to-Digital (A/D) converter, where each of the time slots within the TDM video is converted to an 8-bit binary word. Data is then transmitted over four byte-serial buses to the ATC.

An analog signal proportional to the scanner mirror angular position is derived from the Hall-effect transducer in the scanner module and routed to the FLIR Digitizer through its own interface buffer/filter, and then to the position quantizer. The position quantizer is a tracking A/D converter which provides a digital word proportional to the scan mirror angular position, as well as a series of temporal pulses corresponding to the spatial pixel positions. In addition, the position quantizer detects the mirror scanning direction (i.e., forward or retrace) and generates a corresponding binary signal. These signals are used by the multiplexer controller and the video A/D converters to establish multiplexer channel addresses and analog-to-digital conversion times. Finally, signals are routed from the multiplexer controller to the ATC, along with the four byte-serial buses. The detailed design of the components of the FLIR digitizer is discussed in the following paragraphs.
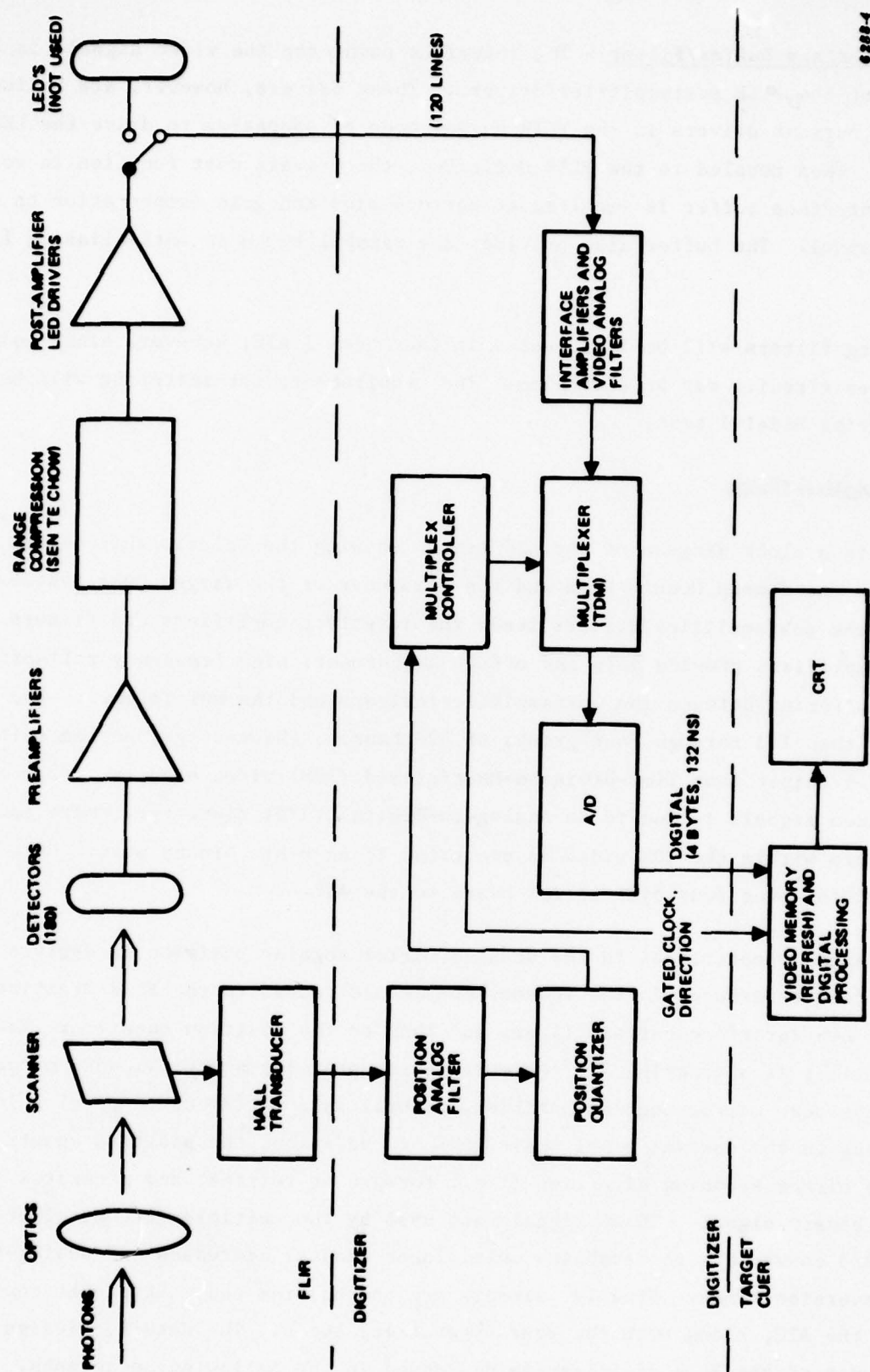
Figure 4-3. Targeting System Block Diagram

4.1.3.1 Position Quantizer - The objective of the position quantizer is to generate a series of temporal pulses corresponding to the image spacial pixel locations. Processing stability must be to within 0.02 percent of total image width with temporal pulses generated every 0.08 percent of total image width. The most obvious source of an analog signal proportional to scanner mirror angular position is the Hall-effect transducer already in existence in the scanner servo loop. Communication with the manufacturer of the transducer, Aeroflex, Inc., states that the transducer should have adequate short-term stability to satisfy both stability and linearity requirements. The transducer is a magneto resistor operated in a dc bridge circuit, nominally null when mirror deflection is zero. This positional signal may be tapped by either connecting directly to the bridge differential output or by connecting to the FLIR scan mirror servo amplifier. The latter appears to be easier, assuming that the servo does not go into saturation during parts of the scan cycle. The excitation voltage, which is controlled by the scan mirror servo loop, may be constantly changing as a function of oscillation magnitude however. In order to preclude the problems of scale factor shift, the quantizer utilizes the excitation voltage as a reference, thus sensing by taking the ratio between the bridge output and the excitation voltage. This, of course, requires that the excitation voltage as well as the position analog voltage be supplied to the position quantizer.

The 0.02 percent repeatability requirement implies that noise on the order of -74 dB relative to the analog signal must be eliminated prior to quantization. A filter will be used to minimize the amount of noise. Care must be taken, however, that the filter does not introduce error due to delays through the filter. A filter of the La Place form $(T_1 S + 1)$ $(T_2 S + 1)$ closely tracks the input signal except during an initial transient period which occurs during an unused time period (i.e., during the mechanical turn-around transient allowance time).

A block diagram of the position quantizer is shown in Figure 4-4. The quantizer is mechanized similar to a tracking A/D converter. The binary state of the up/down counter is fed to the input of a multiplying Digital-to-Analog (D/A) converter through a scale factor multiplier, to match the counter scale factor to that of the D/A converter. The position sensor bridge excitation voltage provides the reference for the D/A converter. The output of the D/A converter, then, is an analog voltage proportional to the binary state of the counter. The negative of this signal is summed with the scanner mirror position analog voltage and routed to a pair of threshold detectors. One is a positive detector, the other, a negative detector. The
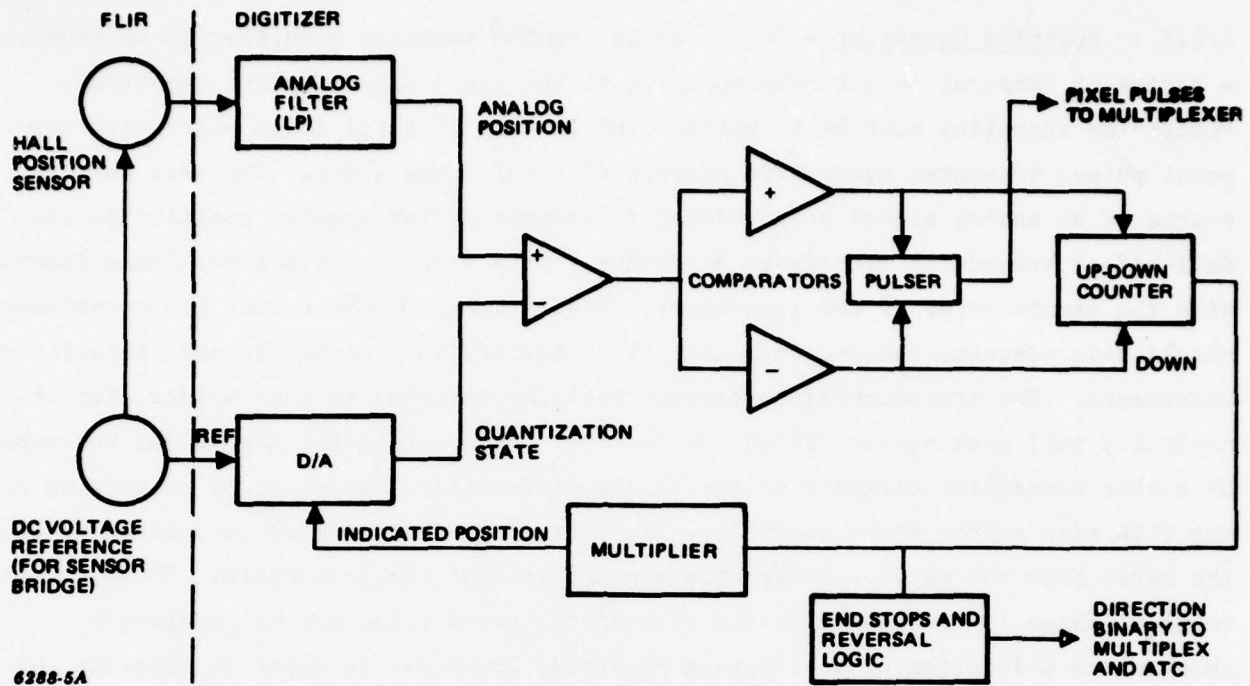
Figure 4-4. Analog Position Quantizer Block Diagram

thresholds are set equivalent to the weight of the least significant bit of the counter. If the scanner mirror position analog voltage exceeds the quantized analog reference, the positive comparator will produce an up-count pulse; conversely, if it is less than the quantized analog, the negative comparator generates a down-count pulse. In either case, an output pulse is generated, which is a temporal pulse corresponding to a spatial pixel position. The contents of the counter, then, is a binary number which continuously tracks the mirror position analog voltage. Additional logic, monitoring the contents of the counter, produces a direction binary (i.e., a signal indicating forward or retrace scan) to the remainder of the system components. In addition, the direction logic inhibits the counter from counting down on the forward scan or up on the retrace scan. Thus, even if the scanner mirror instantaneously reverses direction during some portion of an active scan, the temporal pulses still accurately correspond to spacial locations and the total number of pulses per line remains constant.

A backup procedure to using the Hall-effect transducer, is currently under investigation. Some of the reasons for this are:

a. The repeatability requirement imposes a requirement for nearly 80 dB signal-to-noise ratio (i.e., position analog voltage to random noise). This might be impossible to achieve even with filtering, depending on the proximity of noise sources and the degree of shielding and isolation that can be achieved.

b. The magnetic circuits associated with the transducer could introduce some hysterisis effects so that the analog voltage is not a faithful representation of mirror position. This would be of no particular consequence if any such offset were fixed and linear, as the delta adjustments would compensate, but would be disastrous if it were variable and nonlinear.

In the event that the Hall-effect transducer proves inadequate during system test and evaluation, a number of alternate approaches to position determination are available and have been considered. These approaches involve using the back side of the scanner mirror to reflect parallel beams from a light source to a photo-sensitive element. Several approaches, including analog, digital, and an incremental approach using precision Ronchi rulings have been considered. All are somewhat more complex, however, than the approach using the Hall-effect transducer. The alternate approaches will be evaluated and one selected in the next quarter.

4.1.3.2 Multiplexer/Digitizer Design – A simplistic approach to multiplexing and digitizing the video from the FLIR would be to simply implement the electronic equivalent of a 160-position switch, the output of which would be then routed to a single A/D converter. Such an implementation would require each switch position to be selected and settled within less than 26 nanoseconds for a 60 Hertz scan and the digitization rate would exceed 37.8 MHz. This is not a practical approach for many reasons. Therefore, the multiplexer/digitizer has been divided into several identical sections, each operating in parallel, and each accepting 32 input video lines, producing a byte-serial data stream at the output.

Again, a simplistic approach might be to simply implement a 32-pole, single level switch to scan the video inputs. Each switch position in such an implementation would be required to settle within less than a sample period, which would now be less than 132 nanoseconds. While such a scheme is within state of the art, it is unneces-

sarily costly. A switch tree arrangement, which has been selected for this system, is less demanding on circuit design and, therefore, less expensive. Only the highest level of the tree needs to switch at the highest speed, and each successive level of the tree can switch at successively lower rates. A block diagram of the multiplexer and the A/D converter is shown in Figure 4-5. The highest level of the tree is a two-channel multiplexer, while both the intermediate and lower levels are four-channel multiplexers. Buffer amplifiers are provided between the multiplexer levels to minimize loading and interactive effects. The A/D converter, at the output of the high-level multiplexer, is a flash-type converter, consisting of a bank of 256 voltage comparators followed by a logic network which converts the output of the comparators to an 8-bit binary number within a single clock pulse interval (TRW 1007J). The byte-serial output from the A/D converter is then routed to the ATC system, along with an appropriate clock signal and timing signals. Switch sequencing and timing of the multiplexer and A/D converter is controlled by the multiplexer controller.

4.1.3.3 <u>Multiplexer Controller</u> - The multiplexer controller determines the sampling sequence and timing of the multiplexer. This is performed by controlling the addressing of each level of the multiplexer and by establishing the A/D sampling time based on pixel timing which is derived by the mirror position quantizer. In addition, the multiplexer controller provides clock and timing signals to the remainder of the ATC System.

The multiplexer switching sequence is shown in Figure 4-5. The numbers in the column to the left of the block diagram represent the detector (or line) numbers assigned to each of the four blocks of the multiplexer. Numbers in parentheses correspond to the input port numbers for each of the switch devices. Initially, with all of the switch devices set to port (1), line 1 video is routed through A(1), J(1) and L(1) to the A/D converter. At the next clock pulse, L is swiched to port (2) and line 2 video is routed through B(1), K(1), and L(2) to the A/D converter. At the next clock pulse, L is switched back to port (1), but J has been switched to port (2). This results in line 3 being routed through C(1), J(2), and L(1) to the A/D converter. If the sequence is followed through the entire cycle, it will be seen that the intermediate stage switches, J and K, switch at half the rate as the high-level stage, L, while the low-level stages, A through H, switch at one forth the rate of the J and K

DETECTOR
NUMBER

SAMPLE TIME = $T_P/4$ = 1.058E-6 SEC = 1/945E3 = T_1

SAMPLE TIME = $T_1/4$ = 264 NS = 1/3.78E6 = T_2

SAMPLE TIME = $T_2/2$ = 132 NS = 1/7.56E6

8-BIT WORDS

6288-7A
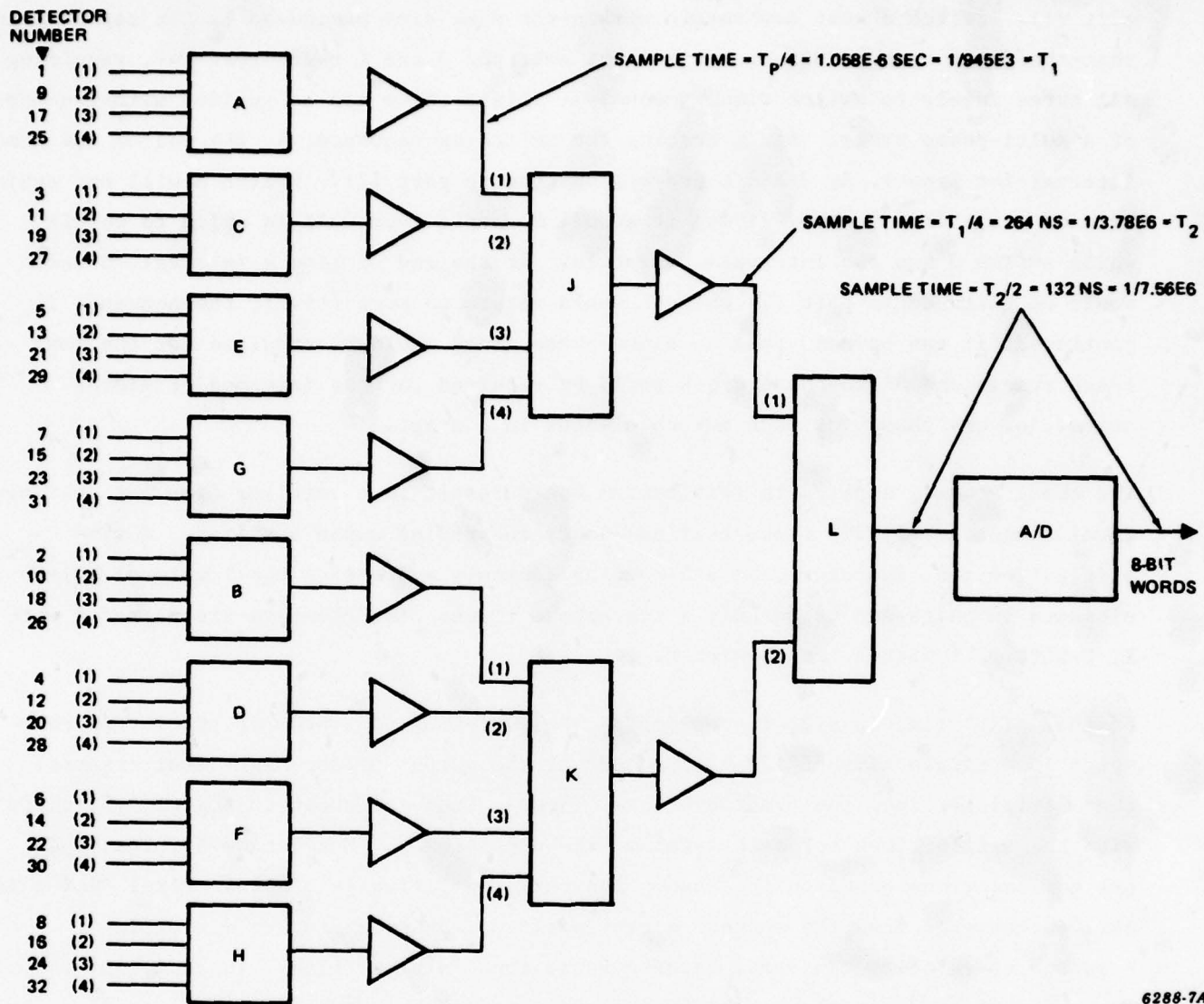
Figure 4-5. Multiplexer Block Diagram

switches, and one eighth the rate of stage L. Thus, only the high-level stage is required to switch at the maximum speed, placing less stringent speed requirements on the lower levels of switching.

Again referring to Figure 4-5 and continuing to follow the switching sequence, it can be seen that if all stages of the multiplexer are switched from a single clock, at several points in the cycle one or both of the intermediate or low-level stages will be required to switch and settle within the same time interval as the high-level stage. For example, at the end of the time interval for sampling line 2 and only a single clock, J and K must switch to port (2) at the same time that L switches to

port (1). Switch J must now settle within the same time period as L. It can be seen that the worst case occurs each time that switches J and K reach port (4), requiring all three levels to switch simultaneously. This problem can be avoided with the use of a multi-phase clock. Again tracing the switching sequence, at the end of the time interval for line 1, A, J and L are all swiched to port (2). Switch A will not again be used until line 9 time, giving it a full 8 sample intervals in which to settle, while switch J has two intervals to settle. At the end of line 2 interval, B and K would be switched to port (2) while L would return to port (1). If the sequence is continued, it can be seen that an eight-phase clock would be required for the low-level stages and a two-phase clock would be required for the intermediate-level stages, or one phase for each switch element in a stage.

The above scheme, applied to this system would result in a settling time for the low-level stages nearly 2.5 times that necessary to provide ample settling. A simplification can, therefore, be achieved by commonly addressing the low-level switch elements in pairs and using only a four-phase clock. The elements are paired A with B, C with D, E with F, and G with H.

Nominal pixel time is 4.23 microseconds. Multiplexing 32 lines per pixel time results in a sample time of 132 nanoseconds at the output of the high-level stage of the multiplexer into the a/d converter. These values are shown in Figure 4-5, along with the sample times for each level of the multiplexer. Note, however, that these are nominal times based on the assumption that pixel time is stable. Pixel timing is derived, however from the scanner mirror position, and the scanner mirror instantaneous velocity can vary, causing variations in pixel time. In addition, the operation of the multiplexer and multiplexer controller requires a total of 37 clock intervals to complete a 32-line sample period. The sampling clock in the multiplexer controller is, therefore, speeded up somewhat to assure completion of a 32-line cycle within a worst-case pixel time. This results in a sample time, at the high-level stage, of 91.5 nanoseconds, rather than the nominal 132 nanoseconds shown in Figure 4-5. Pixel pulses are generated in bursts of 1280 pulses, followed by a mirror reversal gap. For each pixel pulse, the multiplexer completes a 32-line sample, followed by a scan rate margin gap. The multiplexer timing relationships are summarized below. Times are in nanoseconds, TS_{min} is the minimum time interval available for the indicated stage to switch, and TC_{max} is the maximum estimated time required for the components of the indicated stage to switch.

Stage	TS_{min} (nsecs)	TC_{max} (nsecs)	Margin (nsecs)
A thru H	640	548	92
J and K	183	157	26
L	91.5	60	31.5

From the above, it can be seen that there is a time margin available at each level of the multiplexer.

The multiplexer controller causes each of the multiplexer sections to sequentially sample 32 video lines for each pixel position, as determined by the scanner mirror position quantizer. This successive sampling causes the spatial location of the sample for successive IR image lines to be slightly skewed. This skew is relatively minor, being bounded by two successive pixel positions. However, in order to minimize the effect on pattern recognition algorithms, the adjacent multiplexer blocks are programmed to sample their image lines in opposite order, as illustrated in Figure 4-6A. Thus, multiplexer block 1 samples its lines in 1 to 32 order while block 2 samples in 64 to 33 order, and so on for the remainder of the blocks. The resulting skew pattern is triangular in shape rather than an abrupt sawtooth pattern. Note also, in Figure 4-6B that on the retrace scan if the samples triggered by the Nth pixel are taken in the same order as on the forward scan, the skew pattern will fall between N and N-1 rather than between N and N+1 as on the forward scan, and the slope of the skew pattern will be inverted. This is illustrated by the solid dots of Figure 4-6B. This phenomenon is avoided by offsetting the pixel positions by one space and by reversing the multiplexer sequence order during the retrace scan, as illustrated by the circles in Figure 4-6B. Note that this additionally requires that the multiphase clock controlling the multiplexer switching sequence also be reversed during the retrace scan.

Figure 4-7 is a block diagram of the multiplexer controller and its relationship to the multiplexer. The multiplexer scan cycle is initiated by receipt of a pixel pulse from the scan mirror position quantizer. This pulse starts a gated clock oscillator which drives the Programmable Read Only Memories (PROM) counter. A decoder provides a feedback to turn off the gated clock after the correct number of cycles necessary to complete a 32-line cycle. Additional outputs from the decoder and a set of flip-flops provide a gated clock coincident with valid data from the A/D converter. The outputs from the PROM counter provide addresses for a set of PROM's which provide a
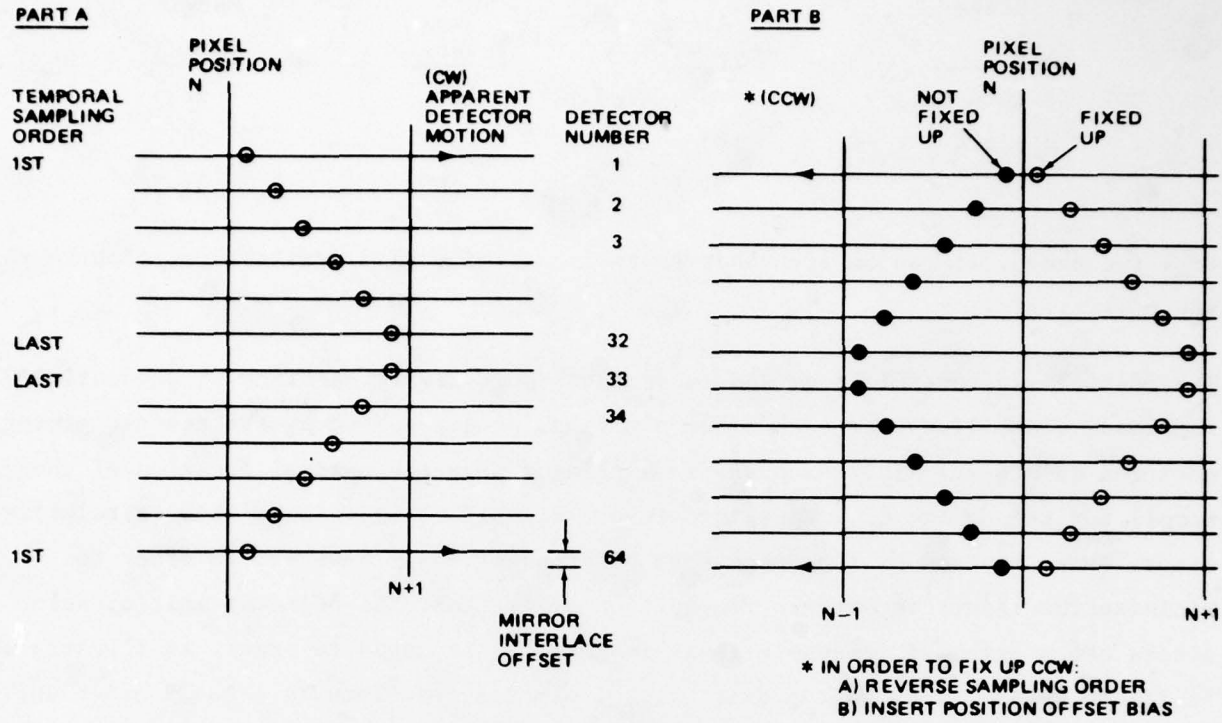
Figure 4-6. Spatial Skew

translation from the straight sequential count of the PROM counter to the multiphase addresses required by the multiplexer. In addition, the direction binary signal, derived in the scan mirror position quantizer, controls the scan reversal required during the retrace scan. The outputs from the PROM's are then latched into the address registers of each of the multiplexer blocks. Note that there is a delay between the gated clock oscillator and the PROM counter. The A/D converter is strobed from the undelayed clock, whereas the counter is incremented from the delayed clock. This delay allows setting the strobe point of the A/D converter so that the multiplexer switches have had sufficient time to settle. The A/D converter is strobed at a point just prior to changing the multiplexer addresses. This makes maximum use of the settling time available for the multiplexer switches.

4.1.3.4 Packaging and Partitioning – In the Model 1 configuration, the entire FLIR Digitizer will be packaged in a stand alone unit. There are numerous possible combinations of partitioning the FLIR digitizer for packaging into the Model 2 airborne configuration. These combinations are presently being studied to determine an optimum configuration. Some of the factors that influence this study are discussed below.

4-16

Figure 4-7. FLIR Digitzer Block Diagram

8-BIT WORDS TO ATC

GATE (1C)

1b   c

A/D

GATED 2-CHANNEL AMPLIFIER (1445)

1b 8b 8b 1b 1b   c

MUX UNIT 2

MUX UNIT 3

MUX UNIT 4

DC POWER SUPPLIES

4D (1B)

ANALOG TIME DIVISION MULTIPLEXER (TDM)

2b (1A8)

M4A   M1B   M2B   M3B   M4B

INTERFACE AMPLIFIERS
(TOTAL = 32 ANALOG INPUTS)
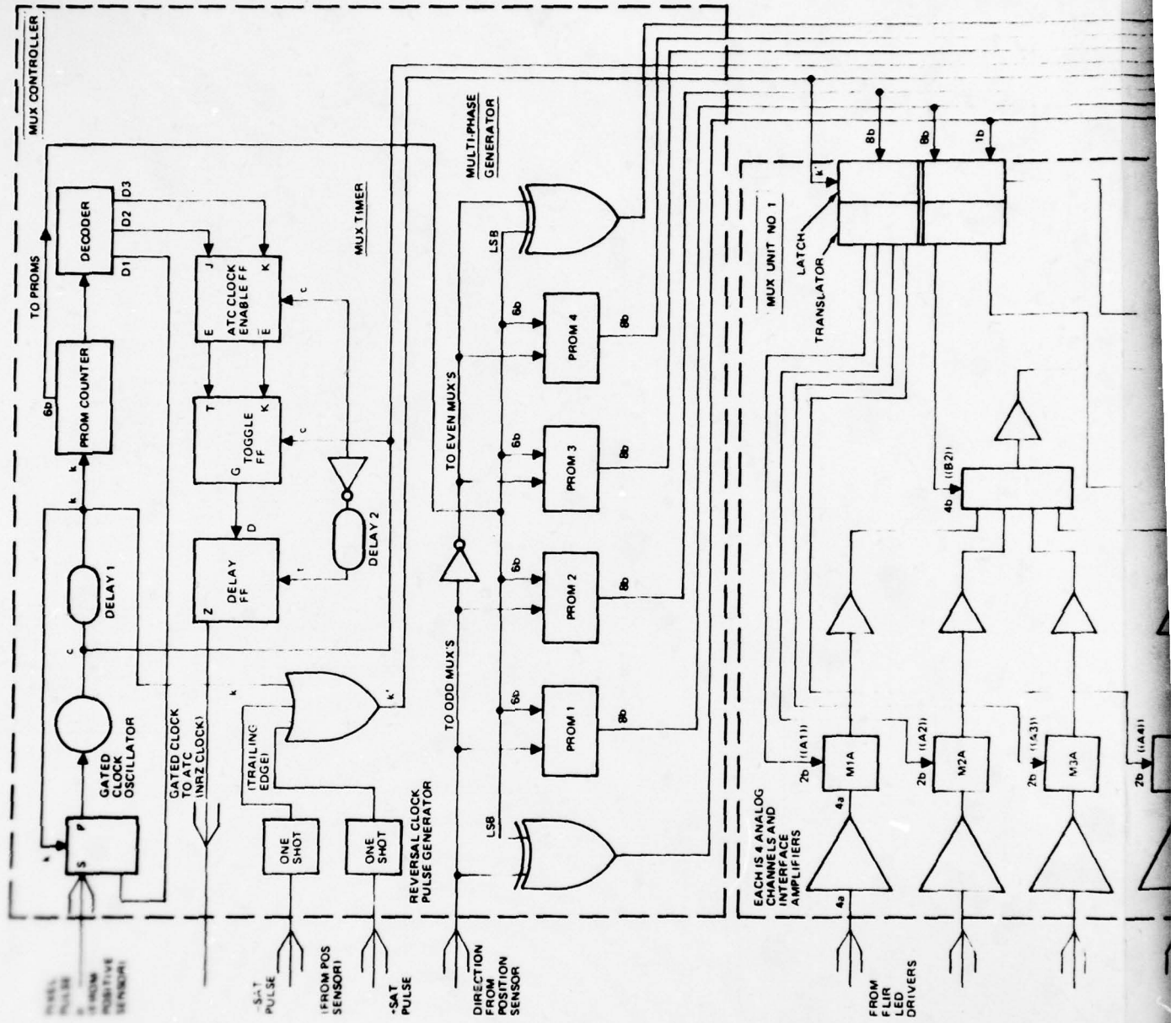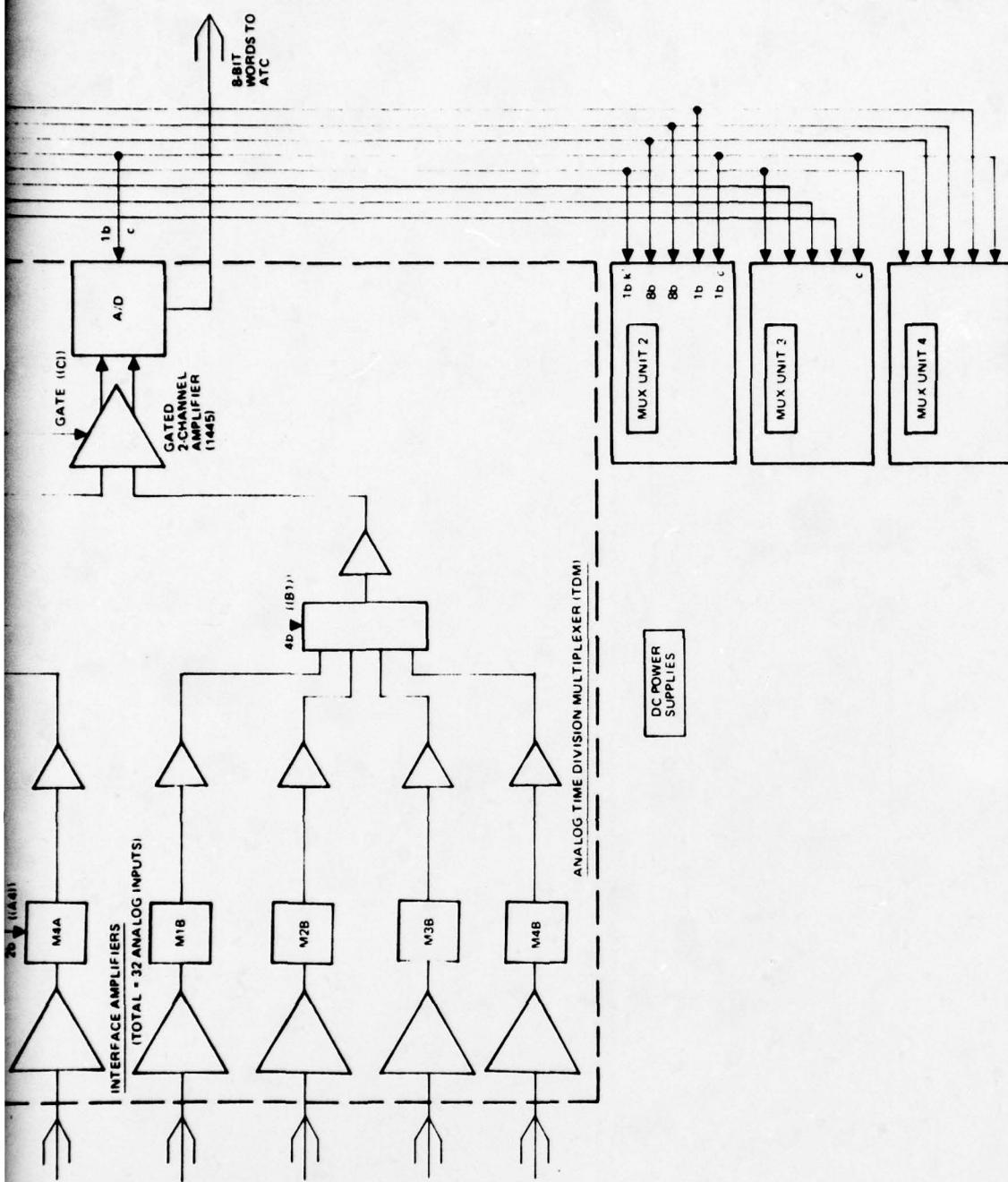
The LOHTADS FLIR is presently mounted onto a two-axis gimballed inertial platform
system. This system is mounted inside a single-axis gimballed turret, which forms a
redundant azimuth to provide a wide net angular travel for the system. In order to
minimize susceptibility to noise, and in order to minimize the number of leads
crossing the gimbal interfaces, some portion of the input circuits to the FLIR
Digitizer must be physically placed in close proximity to the FLIR postamplifier/
drivers. Considerations in accomplishing this must include:

a. Mechanical size and weight of the additional circuitry

b. Effect of added weight and mass unbalance on the gimbal servo systems

c. Heat removal techniques and effects of temperature rises

d. Quantity and placement of flex leads and effects on gimbal servo loading

e. Physical limitations on lead placement between turret and airframe

f. Electromagnetic Interference (EMI) considerations.

Obviously, the fewest weight, volume, and temperature effects would accrue if all de-
tector video lines were simply brought out from the gimbal and all of the entire FLIR
Digitizer was airframe-mounted. However, in that case the number of leads and the EMI
problems would be unmanageable. The other extreme would place the entire multiplexer
on the gimbal, resulting in only a single video Time Division Multiplex (TDM) signal
leaving the gimbal. While this would certainly simplify the lead and EMI problem,
the size, weight, and temperature rises would be prohibitive. A compromise
partitioning currently being considered would separate the circuitry either between
the low-level multiplexer and its buffer/amplifier or between the low-level buffer/
amplifier and the intermediate-level multiplexer. With this approach, all of the re-
mainder of the FLIR Digitizer, with the exception of the amplifier/filter for the
scanner mirror position signal, would be airframe-mounted.

A large proportion of the FLIR Digitizer consists of repeated circuitry, especially
in the multiplexer. Cost and other factors make it desirable to partition the cir-
cuitry so that a relatively large number of assemblies are functionally identical.
In addition, for a number of reasons, it is desirable to partition the circuitry so
that functional entities are totally contained on a single assembly. Finally,
partitioning should be accomplished so that insofar as possible area, volume, and
heat dissipation are relatively evenly distributed.

Figure 4-8 is an overall diagram of the FLIR Digitizer showing the functional partitioning. Both the interface amplifiers and the quadratic low pass filters may be omitted if system testing on Model 1 proves them unnecessary. Table 1 summarizes the parts count, area, volume, and heat dissipation requirements of each of the functional elements shown in Figure 4-8. From Table 1 it can be seen that partitioning strictly along functional lines will result in some assemblies being very sparsely populated. Therefore, in some cases more than one function will be contained on a single assembly.

From Table 1 it can also be seen that the interface amplifiers and the low pass filters occupy a considerable volume because there is one set required for each video channel. Since these might be omitted, a final decision on partitioning for Model 2 must await the outcome of Model 1 system testing.

4.1.4 Status

The proceeding design description demonstrates part of the effort that has been completed to date. An analysis of the FLIR optical system, including studies of optical resolution, has been completed. A review of the electronic design of the FLIR and its internal logic has been completed. The optical studies and review of the electronics enabled the determination of sampling rates and timing requirements. Finally, a review of the FLIR electromechanical scanner design enabled a complete definition of the FLIR Digitizer design requirements. A number of concepts for multiplexing and digitizing the video data were then devised, and a study of currently available, off-the-shelf components was concurrently initiated. This led to a final selection of a suitable scheme that was consistent with the numerical parameters of both the FLIR signal requirements and the available circuit components. Several methods were devised for determining the scanner mirror position and one that appears to be the simplest was selected for implementation. A complete design of the selected approaches, including detailed logic diagrams and extensive analyses of precise timing and propagation delays, has been completed. At present, the electronic circuit design is being constructed on an extensive wire-wrapped breadboard which will be used to verify multiplexer switching speed calculations, to test D/A and A/D converter performance, along with their associated support circuits, and to test the PROM's and their associated programming. Parts procurement has been initiated, and most of the components have already arrived.
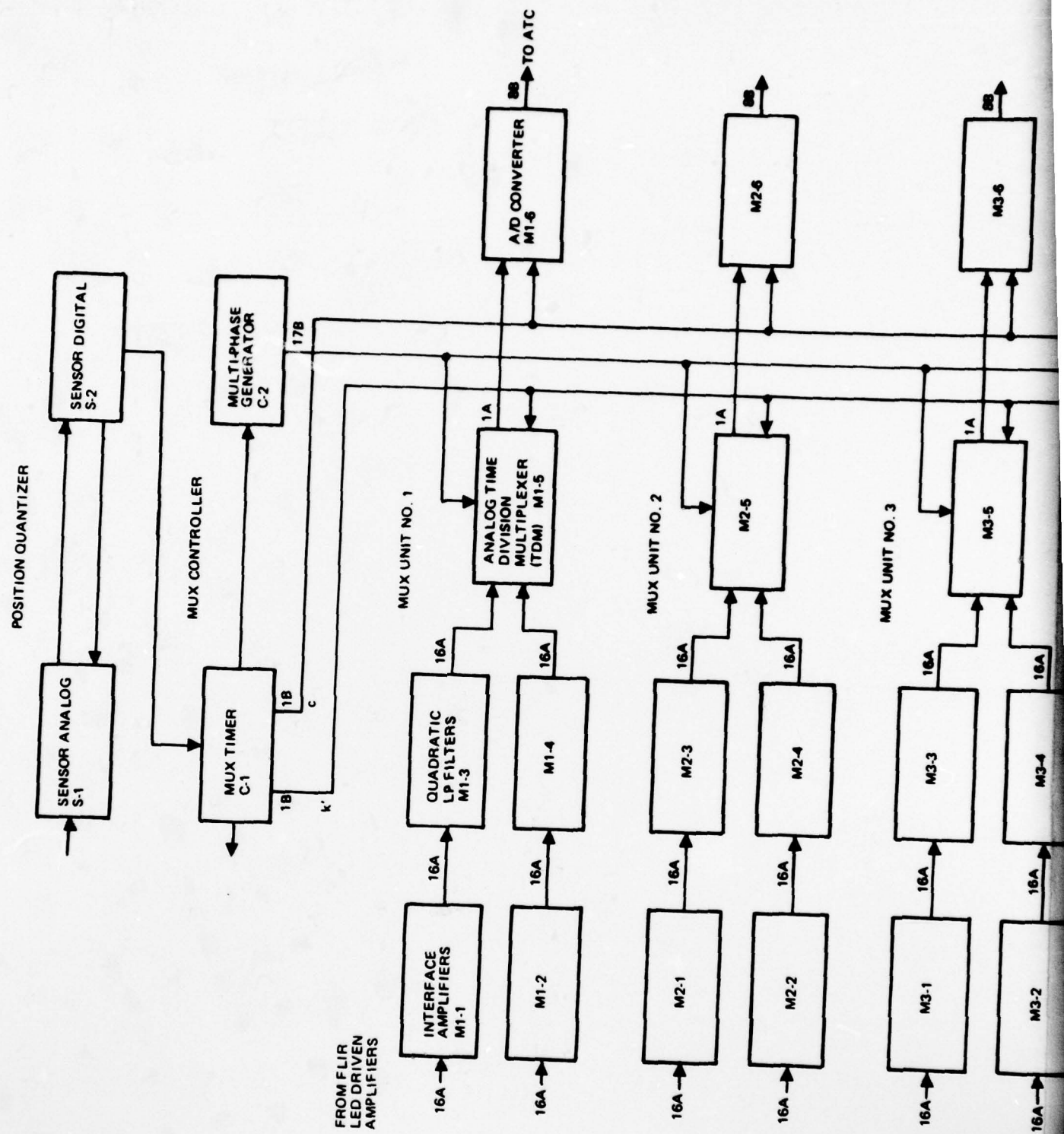
Figure 4-8. FLIR Digitizer Functional Block Diagram

MUX UNIT NO. 4

M4-6

M4-5

M4-3

M4-4

M4-1

M4-2

1A

16A

16A

16A

16A

16A

16A

6B

COMMON MODE REJECT AMPLIFIER
(1 PER SYSTEM)

(ANALOG POWER)
VDC

SECOND-STAGE
REGULATORS
P-2

(TTL POWER)
5 VDC
RTN

−15 −12 −6 RTN 12 15

8A

POWER SUPPLIES (DC)
P-1
(PROBABLY LOCATED
IN ATC) REQU'S
FLOATING GND

NOTES:
1. A = ANALOG DATA STREAM
2. B = BINARY DATA STREAM (ONE BIT)
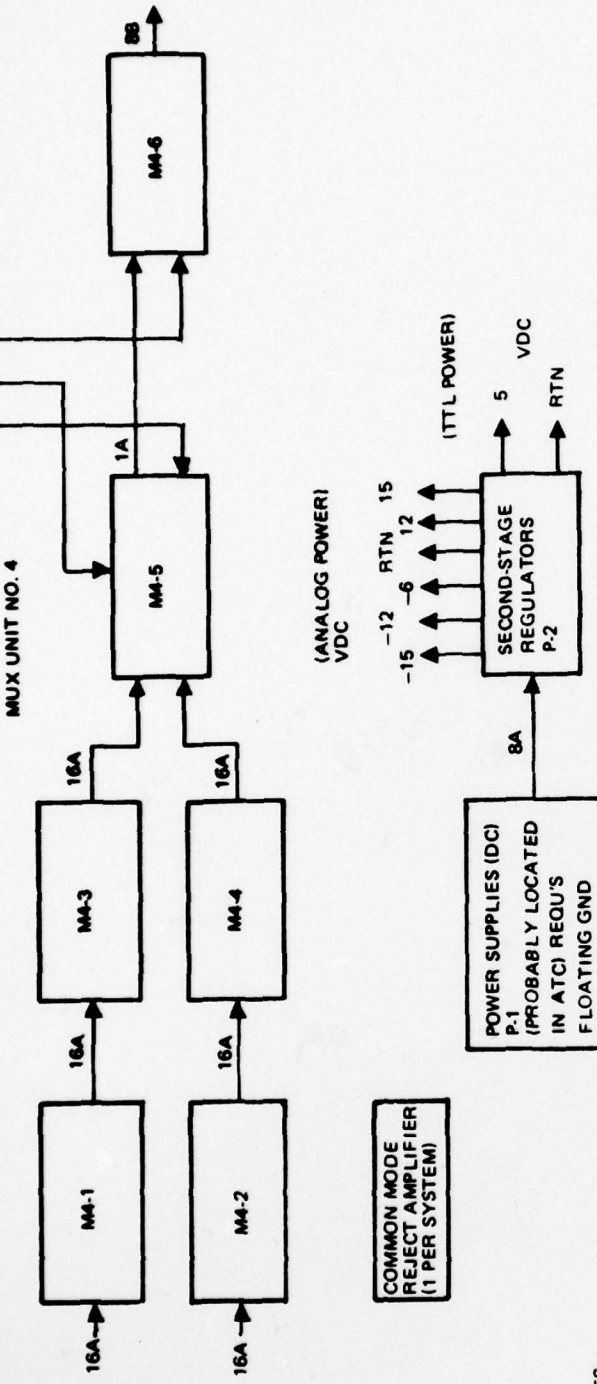
6288-10

Table 4-1. Component Count, Area Volume, and Power Requirements

Entry	Symbol	Block Name	Block Qty.	Total Power (watts)	I. C. Count 14/16 PIN	I. C. Count 20+ PIN	Trimpot	Misc. Discretes	Area (Sq. In.)	Volume (Cu. In.)
1	C-1	MUX TIMER	1	1.25	10	2		5 Caps	13.2	6.6
2	C-2	MULTI-PHASE GEN	1	1.90	7	4		5 Caps	15.2	7.6
3	S-1	SENSOR ANALOG	1	6.03	20	3	4	45 Caps 10 Res.	39.6	19.8
4	S-2	SENSOR DIGITAL	1	2.3	14	2		8 Caps 10 Res.	15.4	7.7
5	M1-5 thru M4-5	ANALOG TDM	4	22.8	84	8		116 Caps	89.7	44.9
		TOTALS	8	34.3	135	19	4	179 Caps 20 Res.	173.2	86.6
6	MN-6	A/D CONVERTER	4	37.6	20	4		44 Caps 84 Res. 16 Trans.	69.1	34.5
		TOTALS	12	71.9	155	23	4	223 Caps 104 Res. 16 Trans.	242.3	121.1
7	M1-1 thru M4-1 and M1-2 thru M4-2	INTERFACE AMPLIFIERS	8	31.2	160		256	160 Caps 128 Res.	205	102.5
		TOTALS	20	103.1	315	23	260	383 Caps 232 Res. 16 Trans.	447.3	223.6
8	M1-3 thru M4-3 and M1-4 thru M4-4	QUADRATIC LP FILTERS	8	12.5	32		256	352 Caps 512 Res.	174.6	87.3
		TOTALS	28	115.6	347	23	516	735 Caps 744 Res. 16 Trans.	621.8	310.9

Meanwhile, preliminary effort towards mechanical packaging of the brassboard unit was initiated with a visit to Ft. Belvoir to inspect the LOHTADS helicopter platform gimbal and turret system which will house the FLIR and portions of the FLIR Digitizer. Information gained there, and considerations of logical and functional grouping; quantity and length of signal leads; volume, weight and heat constraints; and EMI control have led to preliminary system partitioning. This, along with breadboard test and evaluation results will lead to a final partitioning and mechanical design and packaging of the brassboard unit. Future plans call for:

a. Completion of the breadboard multiplexer

b. Test and evaluation of the multiplexer breadboard design

c. Mechanical design and packaging of the Model 1 Multiplexer.

4.2 FRAME STORE MEMORY

4.2.1 Requirements

The frame store must accept data from the FLIR Digitizer at real time rates, store the data in memory, and recall specified bytes of data from the memory on request of the detector or the silhouetter. In addition, it must accept data from a test set in a format compatible with that from the FLIR digitizer and output it, a byte at a time, to the test set.

Figure 4-9 is a functional block diagram of the Frame Store (FS). The various blocks are functional units and are not necessarily packaged together.

4.2.2 Store Mode Control Logic (SMCL)

The SMCL controls the storage of data as it comes in. A nonreturn-to-zero clock, a FORWARD signal, and a negative going pulse called "snatch" are received from either the FLIR digitizer or the test set. The snatch pulse starts a cycle of storage which ends with one frame of data in the memory. The SMCL selects the input signals on the basis of whether it is in the normal store mode or in test. It controls the start of the storage cycle to coincide with the start of a frame sweep by the FLIR Digitizer. It gates the clock signal so that it does not reach the rest of the system until the cycle starts. The clock and the forward signals are forwarded to the clock and timing block. There, the delayed clocks that control the generation of the memory
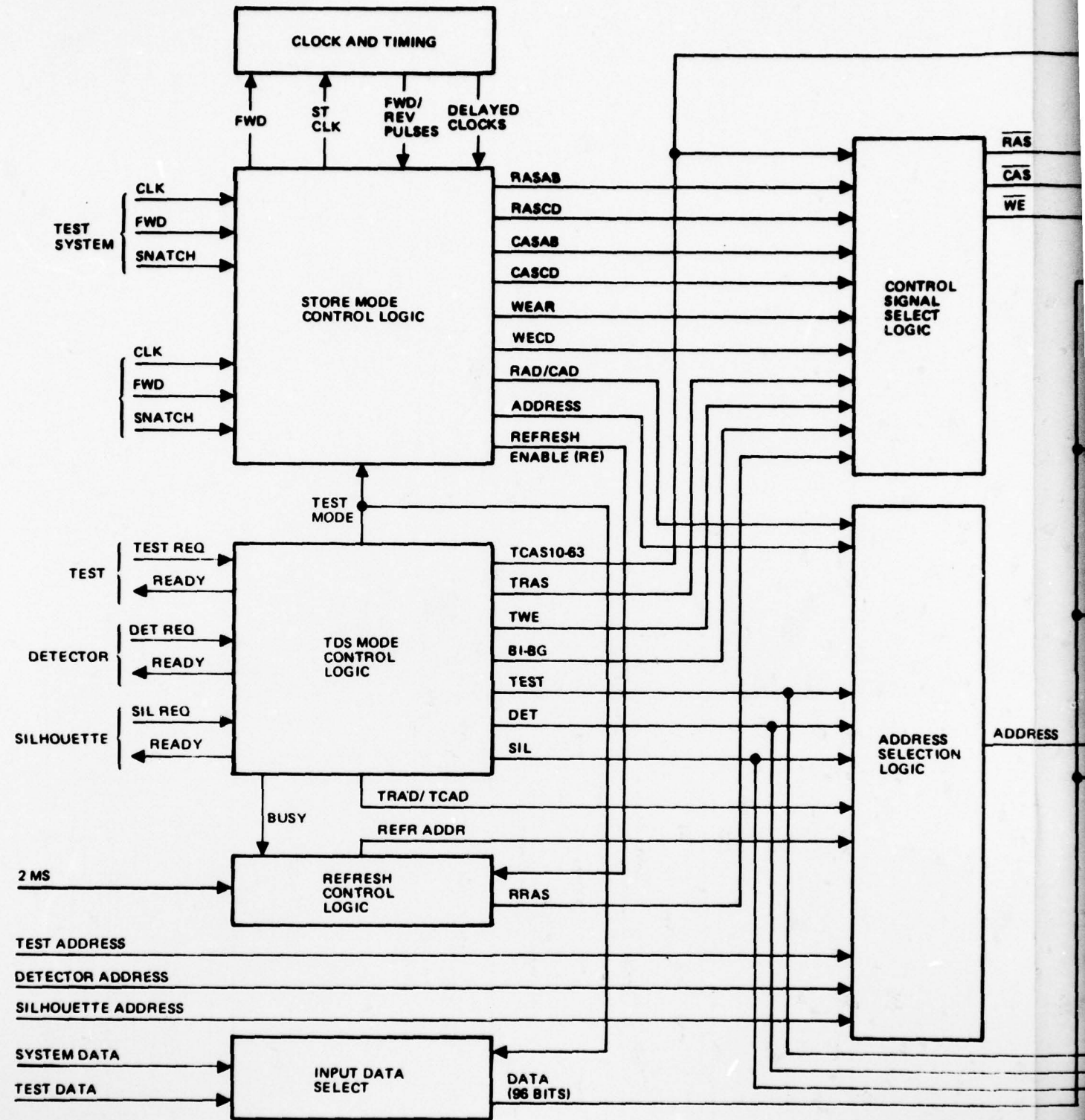
Figure 4-9. Frame Memory System Block Diagram

MEMORIES

BAND 1

BAND 2

BAND 3

BAND 4

OUTPUT
DATA
SELECT

TEST
OUTPUT
REGISTER

DATA

DETECTOR
OUTPUT
REGISTER

DATA

SILHOUETTE
OUTPUT
REGISTER

DATA

62RR 11
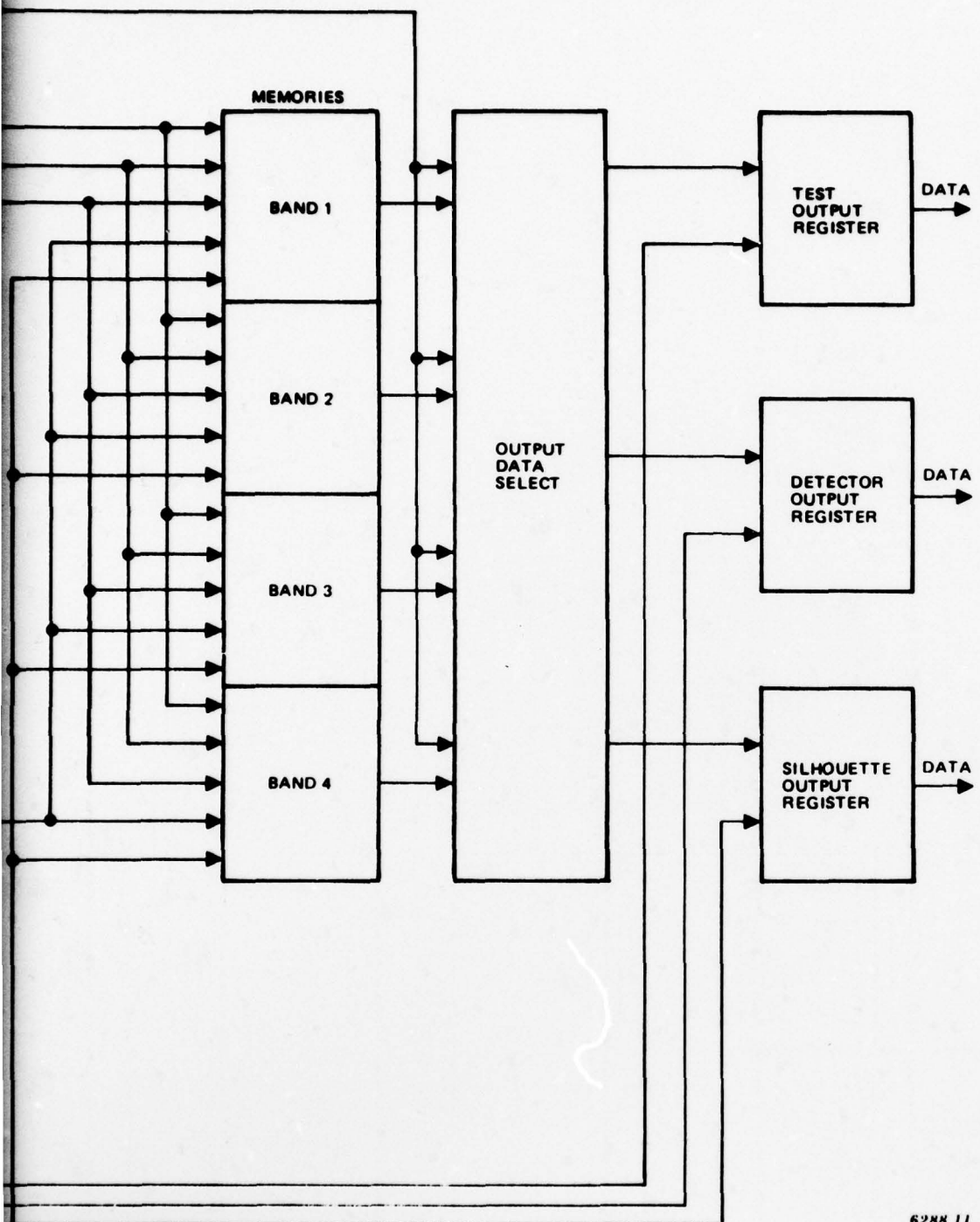
control signals, and the pulses that indicate the start of forward and return sweeps
are generated. These signals are returned to the SMCL where the various control
pulses to the memory are generated. The SMCL also contains a counter and necessary
logic to generate the addresses at which the incoming data are to be stored.

The forward sweep takes approximately five milliseconds, but the dynamic memories
which store the data must be refreshed at least every two milliseconds. Data comes
in 32 sample bursts, and intervals up to three microseconds may exist between suc-
cessive bursts. The SMCL detects when these intervals are present and forwards a
signal to the Refresh Control Logic (RCL) which initiates refresh of two rows of
memory. This permits a complete cycle of refresh within the prescribed two
milliseconds.

4.2.3 Output Mode Control Logic (TDSMCL)

The output MCL controls the operation of the system during output to the test set,
the detector and the silhouetter. It receives requests from these three devices,
processes them without mutual interference, generates the control signals required to
retrieve the requested data, and forwards them to other blocks in the diagram. Upon
receipt of the request from any device, the output MCL sets a flip-flop. The output
of this flip-flop is returned to the requesting device. Thus, a signal is high when
the frame store is able to accept requests. When the signal goes low, the requesting
devices knows that its request is being processed and can turn off the request. When
the data is retrieved and ready, the signal again goes high, indicating that the re-
questing device can read the data.

4.2.4 Refresh Control Logic

The RCL controls the timing and generation of control pulses to the memories to en-
sure that the data contained therein is refreshed frequently enough so that it will
not be lost. Refresh operates in two modes. First, when the system is accepting
data from either the FLIR Digitizer or the test set, the RCL waits for the Refresh
Enable (RE) signal from the SMCL.

At the RE signal it generates two row refresh signals and returns to the wait state.
In addition, a full cycle of refresh will completely refresh the memories during the
400 microsecond turnaround time at the end of the sweep in either direction. The

other mode is used at all times other than when the frame store is receiving data. On receipt of the two-millisecond signal, a complete cycle of refresh is started and completed. If the signal is received while the FS is servicing an output request, it will be stored for the short time until the request is satisfied and then it will be acted upon. The two-millisecond signal comes from the system computer. The RCL will contain its own address counter. In operation during the input modes, the counter will be advanced two counts each time there is a refresh operation indicating that two rows have been refreshed. At the end of each sweep, either forward or reverse, the counter will be reset and a complete cycle of refresh run. Similarly, at each two-millisecond pulse, the counter will start at zero and all rows will be refreshed. There are 256 rows in the memory, 160 of which will be active. Therefore, 160 refresh pulses will be generated in each complete cycle.

4.2.5 Input Data Select (IDS)

Incoming data may originate in either the test set or in the sensor device via the FLIR Digitizer. The IDS selects the proper input for the operating mode of the system. In normal operation it accepts the data from the FLIR Digitizer. In test mode, it accepts data from the test set.

There will be four memories for each bit of each eight-bit input from the FLIR Digitizer or the test set. These will be cycled so that each one accepts every fourth incoming word. In order to alleviate timing problems, the first word is stored in a bipolar register. Then the required timing pulses are generated so that this stored byte is strobed into the first memory and, simultaneously, the second byte is strobed directly from the input wires into the second memory. The IDS contains the logic to control this data presentation.

4.2.6 Control Signal Select Logic (CSSL)

Control signals which strobe data into and out of the memories are generated in the SMCL, the TDSMCL and the RCL. The CSSL selects the appropriate source for the instantaneous operating mode of the FS.

4.2.7 Address Selection Logic (ASL)

Addresses are generated in the SMCL and the RCL. They are also sent from the three requesting devices. The ASL selects the proper address source for the mode in which the FS is currently operating.

4.2.8 Memories

The memories consist of 192 dynamic Random Access Memories (RAM's). Each is capable of storing 32K-bits of data. Data is strobed into them, refreshed as necessary while in storage and retrieved from the RAM's by means of Row Address Select (RAS), Column Address Select (CAS) and Write Enable (WE) pulses properly timed with respect to each other. The data to be stored or retrieved will be located by the address. The generation of all of these has been discussed above. They are now applied properly to the memories and data is either written into them or retrieved from them.

4.2.9 Output Data Select (ODS)

Data is retrieved from the memories one byte at a time. If the outputs of the memories are directly paralleled, no two can be strobed at the same time. Since other aspects of the operation require such simultaneous strobing, some isolating circuitry must be placed on the outputs of the memories in order that there is no mutual interference. The ODS selects a particular memory group to output data in accordance with the address presented by the requesting device. The data so retrieved is placed on a single set of output lines.

4.2.10 Output Data Registers (ODR)

The output data registers look at the data output of the ODS. The TDSMCL generates signals according to the requesting device which strobes the data into the appropriate output device where it is held. Since the device which requested the output reads only on the rise of the ready signal, the information in the output registers is not cleared. When the next request is serviced, the new data replaces the old.

4.2.11 Packaging

The circuitry for the FS will be packaged on the standard circuit cards described elsewhere in this report. These cards will mount approximately 55 microcircuits and the necessary discrete components. Each band of memories will include 32 memory chips. There will be four such bands for LOHTADS, each band handling 32 detector channels. Along with each set of memories, there will be the microcircuits dedicated to the operation of that particular set. The microcircuits include drivers, inverters, and gates which control that group and no others. Some of these circuits may show on the diagram as parts of other functional blocks.

The control logic central to all bands will be mounted on separate cards. At present it appears that two cards will be required for the necessary number of circuits.

4.3 PROCESSING ELEMENTS

The ATC will be implemented using both special purpose hardware/firmware designs and a number of general purpose microcomputers. The microcomputers will be used, when design considerations allow, to provide maximum flexibility in the system design. However, there are some functions which, due to high data rates and/or simplicity of the algorithm designs, dictate the use of specially developed hardware.

Digital Equipment Corporation's (DEC) LSI-11/2 has been selected as the general purpose microcomputer for the ATC. This decision is based on three factors: (1) Its instruction set, (2) its availability, and (3) compatibility with the laboratory system. All these factors, contribute to a favorable impact on cost to the program. Because the LSI-11/2 instruction set is a subset of the instruction set of the PDP-11/34, the programming effort to convert the ATC Algorithm implementations which are now being developed and tested on the PDP-11/34 is substantially simplified.

It is anticipated at this time that three microcomputers will be utilized in the ATC system, one for each of the following system functions:

a. Automatic Target Detection
b. Target Silhouetter
c. Target Classifier.
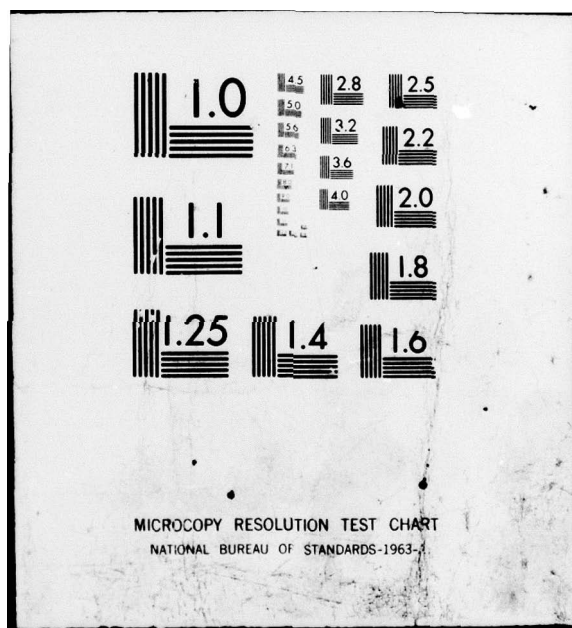
MICROCOPY RESOLUTION TEST CHART

NATIONAL BUREAU OF STANDARDS-1963-A

A typical microcomputer subsystem is illustrated in Figure 4-10 and will consist of the following processor modules: (1) One LSI-11/2 central processor unit, (2) One 8K-word RAM Module used for scratch pad memory, (3) One 24K-word Erasable Programmable Read Only Memory (EPROM) Module used for storing the algorithm implementations, and (4) two 16-bit parallel interface units to communicate with other subsystems of the ATC.

During debug, integration, and testing of a typical microcomputer subsystem the EPROM circuit board is substituted with an MXV11-AC multifunction module which has 16K-words of RAM and two RS232 serial line interface ports. This will allow the microcomputer to be interfaced directly with Northrop's instrumentation system as illustrated in Figure 4-11. The instrumentation system with its peripherals provides an efficient means to accomplish the following system checkout functions:
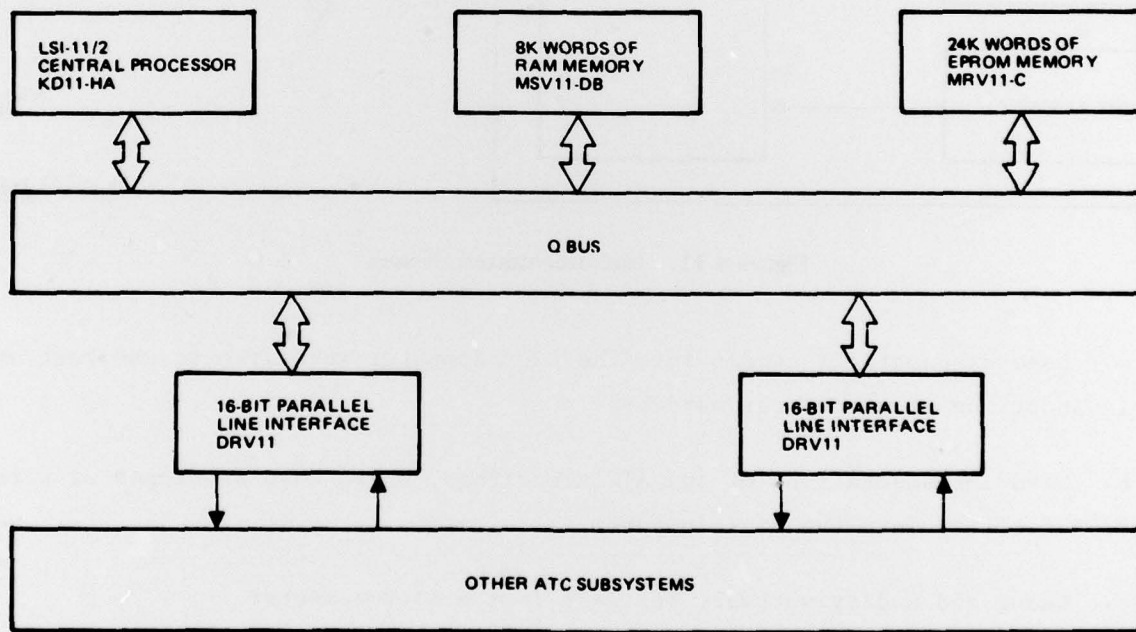
6288-12

Figure 4-10. Typical Microcomputer Subsystem

INSTRUMENTATION SYSTEM

ACOUSTIC COUPLER

MAG TAPE DRIVE

COMPUTER AUTOMATION

LSI-2 MINICOMPUTER

FLOPPY DISC DRIVE

HIGH-SPEED PRINTER

CRT TERMINAL

MULTIFUNCTION MODULE

MXV11-AC
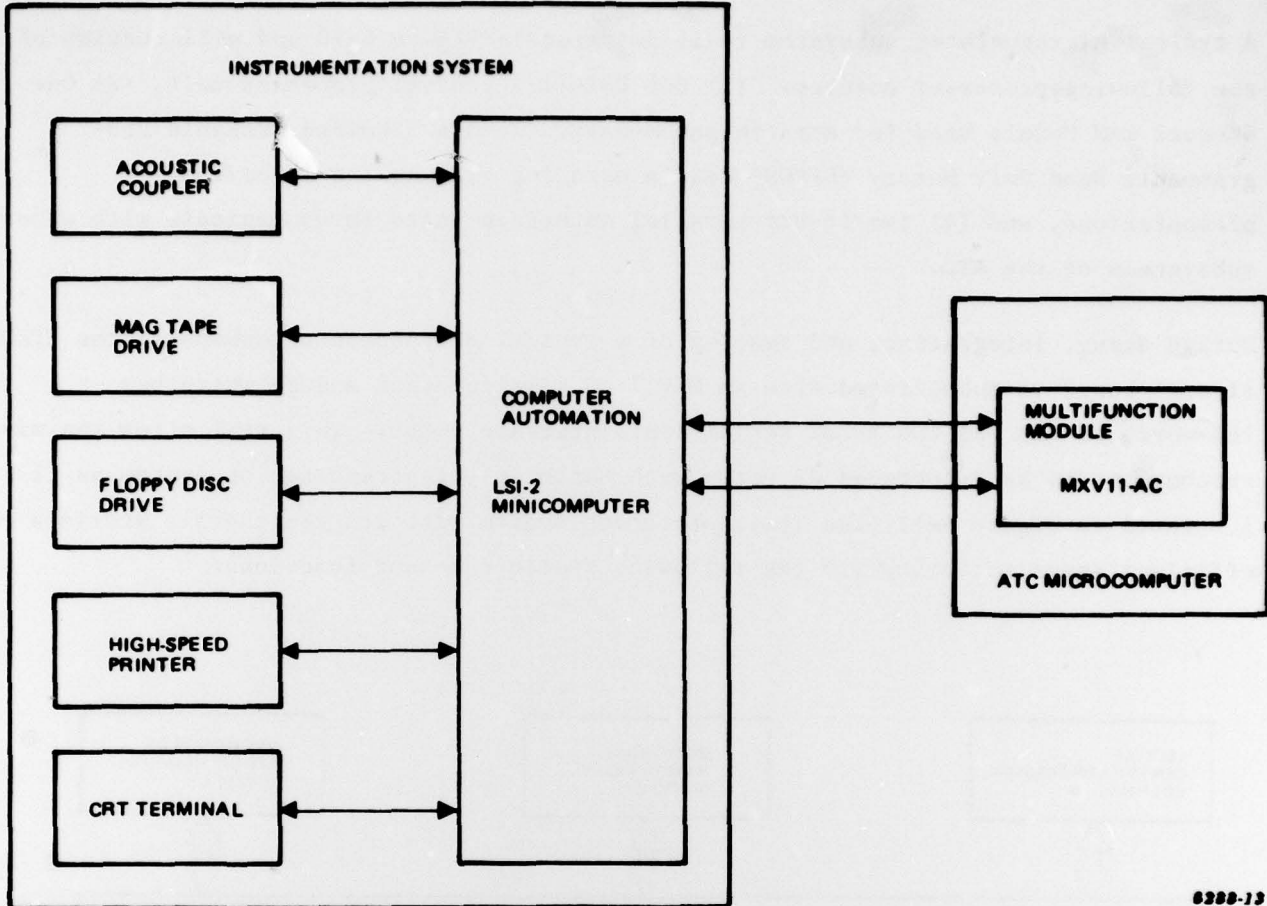
ATC MICROCOMPUTER

6388-13

Figure 4-11.   Instrumentation System

a.   Load diagnostic routines into the microcomputer subsystem to checkout and trouble-shoot the microcomputer hardware

b.   Load implementations of the ATC algorithms, which have developed at a remote PDP-11/34 facility into the microcomputer

c.   Debug and modify software resident in the microcomputer

d.   Obtain and record pertinent data to evaluate the performance of ATC algorithms.

SECTION 5
TARGET DATA BASE

The FLIR image data received from NV&EOL to be used as simulated input data consists of full frame images recorded on digital tape. In order to support the target silhouetting and classification functions, however, small image subframes that contain candidate target only, are required. Northrop is therefore constructing a FLIR target data base of 32 by 32 pel subframes from the supplied full-frame imagery.

During this quarter, the images from the Fort Polk I and II, Hunter Liggett I, and Alabama data sets have been used to build the target data base. Each subframe selected from these source tapes is included with a leader describing the tape ID and an assigned image number. Class and aspect information are included in the leader as well.

The target data base consists of three principal classes viewed at five aspects. Classes used were jeep, tank, and Armored Personnel Carrier (APC). Aspects used were front, side, rear, 3/4 front, and 3/4 rear. Targets falling outside these classes were classified as "probable targets" or "no aspect," respectively. The target data base distribution by class and aspect, for each source image data set is given in Table 5-1. A brief review of the table shows that no truck images are included. Also, the number of jeep views is somewhat limited. This condition will have to be remedied if jeeps and trucks are to be handled successfully by the ATC system. During subsequent quarters, targets from the available image data sets will be added in order to attempt to fill out the target image matrix.

Table 5-1. Target Data Base Distribution

Fort Polk 1						
	Burning	Front	Rear	Side	3/4 Front	3/4 Rear
Jeeps	0	0	0	0	0	0
APCS	0	0	0	9	1	0
Tanks	0	2	1	63	0	2
Trucks	0	0	0	0	0	0
Personnel	0	0	0	0	0	0
Choppers	0	0	0	0	0	0
No target	0	17	1	15	1	0
Prob Tar	25	3	0	5	0	0

Fort Polk 2						
	Burning	Front	Rear	Side	3/4 Front	3/4 Rear
Jeeps	0	0	0	0	0	0
APCS	0	0	0	10	0	0
Tanks	0	5	23	43	0	0
Trucks	0	0	0	0	0	0
Personnel	0	0	0	0	0	0
Choppers	0	0	0	0	0	0
No Target	0	0	0	0	0	0
Prob Tar	46	0	0	14	0	0

Alabama						
	Burning	Front	Rear	Side	3/4 Front	3/4 Rear
Jeeps	0	0	0	12	0	3
APCS	0	4	3	13	4	5
Tanks	0	5	2	15	6	12
Trucks	0	0	0	0	0	0
Personnel	0	0	0	0	0	0
Choppers	0	0	0	0	0	0
No Target	0	27	0	16	0	0
Prob Tar	0	0	0	1	0	0

Hunter Liggett						
	Burning	Front	Rear	Side	3/4 Front	3/4 Rear
Jeeps	0	0	0	0	0	0
APCS	0	0	0	0	0	0
Tanks	0	0	4	7	0	0
Trucks	0	0	0	0	0	0
Personnel	0	0	0	0	0	0
Choppers	0	0	0	0	0	0
No Target	0	0	0	25	0	0
Prob Tar	0	0	0	0	0	0

SECTION 6
PLANS FOR NEXT QUARTER

6.1 INTRODUCTION

The follow-on efforts for the second quarter are discussed in detail, for each task, in the corresponding sections of this report. For convenience, the second quarter plans for each task are outlined below.

6.2 ALGORITHM DEVELOPMENT

6.2.1 Image Enhancement

Hardware configurations for the selected enhancement-candidate algorithms will be evaluated. The enhancement method with the best cost of implementation/performance combination will then be designed, and construction begun.

6.2.2 Target Silhouetting

The target-silhouetting algorithm system will be used to silhouette the entire target data base. This will serve to identify target-data conditions where performance is suboptimal. The connected components and region coloring aspects of superslice will then be evaluated to determine its contribution to the system's performance on sub-optimal data conditions.

6.2.3 Target Detection

Target detection algorithms developed for IR&D will be integrated into the Automatic Target Cuer (ATC) system.

6.2.4 Target Classification

Testing of the Fourier and the University of Maryland's shape features will continue on a larger data base. This effort will be aided by the global data base test of target silhouetting. In addition, a new set of Fourier features as well as Dudani's moment features will be included in the performance testing.

6.3 HARDWARE DEVELOPMENT

6.3.1 Forward-Looking Infrared (FLIR) Digitizer

Critical aspects of the FLIR digitizer will be breadboarded and tested. The design will be completed and construction of circuit cards will begin.

6.3.2 System Memories

Design of the frame store memory will be finalized. Layout and breadboarding will then begin. Also, the scan-converter memory design will be completed.

6.3.3 Local Area Gain and Brightness Control (LAGBC)

Design of the selected LAGBC algorithm will be completed.

6.3.4 Processing Elements

Design of system processing elements will be phased with the definitions of the target detection, silhouetting and classification functions.

6.4 TARGET DATA BASE

Targets from the Hunter Liggett II data base, the A. P. Hill data base and the Graf II data base will be added to the composite target subframe data base.